GEORG-AUGUST-UNIVERSITÄT
GÖTTINGEN

Fakultät für
Physik

Master's Thesis

Studien über $t\bar{t}Z$ Ereignisse im dileptonischen Zerfallskanal (unterschiedliche Leptonenladung) bei $\sqrt{s} = 13$ TeV mit dem ATLAS Detektor

Studies of $t\bar{t}Z$ events in the OS dilepton channel at $\sqrt{s} = 13$ TeV with the ATLAS detector

prepared by

Tobias Christian Orthen

from Hagen

at the II. Physikalisches Institut

Thesis number: MSc-2016/06

Thesis period: 1st April 2014 until 30th September 2016

First referee: Prof. Dr. Arnulf Quadt

Second referee: Prof. Dr. Stanley Lai

Zusammenfassung

Studien über $t\bar{t}Z$ Ereignisse erlauben einen direkten Zugang zum tZ-Kopplungs-Vertex und Sensitivtät auf die Vektor−Axialvektor-Kopplung des schwachen neutralen Stroms. Daraus kann die dritte Komponente des schwachen Isospins des Top-Quarks, T_t^3, abgeleitet werden. T_t^3 bestimmt, ob das Top- und das Bottom-Quark zusammen das schwache Isospin-Doublet der dritten Quarkgeneration bilden und ist daher ein wichtiger Test des Standard Modells der Teilchenphysik.

Dazu wird in dieser Arbeit der dileptonische Zerfallskanal mit unterschiedlicher Leptonenladung (OSSF) von $t\bar{t}Z$ Ereignissen mit einem Schnitt auf das Z-Fenster untersucht. Dies ist eine Herausforderung, da die Statistik in der Signalregion begrenzt und das Signal-zu-Untergrund Verhältnis gering ist. Es werden Variablen zur Trennung von Signalereignissen von den beiden stärksten Untergrundprozessen, Z+jets und $t\bar{t}$ studiert und Neuronale Netzwerke trainiert, um eine Trennung zu ermöglichen. Die erhaltenen Diskriminanten zeigen gute Separationsergebnisse und keine Anzeichen von Overtraining.

Die Ergebnisse dieser Arbeit zeigen damit, dass weitere Studien des OSSF Zerfallskanals dazu geeignet sein können, Untersuchungen der Kanäle mit drei und vier Leptonen zu ergänzen, um den tZ-Kopplungs-Vertex zu erforschen. Die Daten stammen aus Proton-Proton Kollisionen des LHC bei einer Schwerpunktsenergie von $\sqrt{s} = 13$ TeV, wurden im Jahre 2015 mit dem ATLAS Detektor aufgezeichnet und die integrierte Luminosität beträgt 3.2 fb^{-1}.

Abstract

By studying the $t\bar{t}Z$ process one has direct access to the tZ vertex and is sensitive to the vector−axial-vector coupling of the weak neutral current. From that one can deduce the third component of the weak isospin of the top quark T_t^3. T_t^3 determines whether the top and the bottom quark are partners in the weak isospin doublet of the third generation of the quark sector and is therefore an important test of the Standard Model of Particles Physics.

Therefore, the decay channel with two opposite sign same flavour (OSSF) leptons with a cut on the Z-window is studied in this thesis. This channel is challenging because of low statistics in the signal region and a low signal-to-background ratio. Discriminating variables are studied to train artificial neural networks for the two major backgrounds Z+jets and $t\bar{t}$. The two obtained discriminants show good separation power between signal and background events and no overtraining is observed.

The obtained results show that further studies of the OSSF dilepton channel can gain additional knowledge in addition to the three and four lepton decay channels for studies of the tZ vertex. The data for these studies stem from proton-proton collisions of the LHC at a center of mass energy of $\sqrt{s} = 13$ TeV and were recorded by the ATLAS detector in 2015 with an integrated luminosity of 3.2 fb^{-1}.

Contents

1. Introduction

The fundamental constituents of the universe and the forces acting upon them are described by the Standard Model of Particle Physics. The top quark is the heaviest known particle of the Standard Model and its properties therefore play a crucial role for testing key parameters of the Standard Model and for setting boundary conditions for physics models beyond the Standard Model.

The Large Hadron Collider (LHC) is able to produce a large number of top quarks in proton-proton collisions due to its high luminosity and a center of mass energy no other particle collider has ever achieved. With the ATLAS detector, the biggest detector ever built, the technical equipment is available to reconstruct and process data from particle collisions and thereby perform high precision measurements.

As a test of the SM, the measurement of top quark pair production in association with a Z boson is important to access information on the coupling of a top quark to a Z boson. From that coupling one can infer the third component of the weak isospin of the top quark and thus test whether the top and the bottom quark form the weak isospin doublet of the third generation in the quark sector.

In the final state with two opposite sign same flavour leptons the discrimination between signal and background events is difficult. However, it is important to add the results gained from this channel to the ones obtained from other channels. This is expected to increase the sensitivity alongside with a general expected sensitivity increase for analyses with Run II data from the LHC at a center of mass energy of $\sqrt{s} = 13$ TeV.

Chapter 2 gives an overview of the Standard Model and top quark physics with a focus on $t\bar{t}Z$. Chapter 3 describes the LHC and the ATLAS detector as the experimental setup of the used data. After that, Chapter 4 provides the necessary information about the used simulated data samples, the data samples themselves and the objects used in this analysis. In Chapter 5 the methodology of the analysis is outlined including a description of multivariate analysis techniques. Finally, Chapter 6 describes the results of the performed studies before Chapter 7 draws conclusion from the achievements and gives an outlook of further steps to be taken.

In this report natural units are used $(\hbar = c = 1)$ and all masses, momenta and energies are given in electron volts (eV).

2. Theoretical Background

2.1. Introduction

In this Chapter, the general structure of the Standard Model of particle physics (SM) is introduced and the main pillars of the mathematical concept are outlined as well. After that, a more detailed explanation of top quark physics is given. The third part of this Chapter prepares the ground for the analysis presented in this report, the opposite sign dileptonic final state of a $t\bar{t}$ pair produced in association with a Z boson. Therefore, Section 2.4 is dedicated to $t\bar{t}Z$ physics. For further reading, References [1, 2] give a comprehensive overview of the Standard Model and particle physics.

2.2. The Standard Model of Particle Physics

The Standard Model of Particle Physics (SM) describes the components of matter which have no further constituents, elementary particles. Furthermore this theory is able to describe the interaction of particles via forces which themselves are mediated by elementary particles. Mathematically, the SM is described by Quantum Field Theory (QFT) and each particle is an excitation of its respective quantum field.

One major property of particles is their spin, given in units of $\hbar$. Particles with spin $1/2$ are called fermions[1], particles with integer spin bosons. Bosons are mediating the three forces within the SM via which particles can interact: the electromagnetic force via the photon, the strong force via the gluon and the weak force via the $W^{\pm}$ and the Z boson. Gravity, the fourth known force, is not included in the SM.

[1] All particles having half-integer spin are called fermions, e.g. a theoretical particle of spin $3/2$ would be a fermion as well.

Whether particles can undergo interactions via one of the forces is defined by their quantum numbers and allows to further categorise the fermions into quarks and leptons. Quarks can interact via all three forces because they carry the electromagnetic charge, the strong colour charge and the weak isospin. In fact, only quarks can couple to gluons and interact via the strong force. This distinguishes them from leptons which only interact via the weak force and charged leptons also via the electromagnetic force.

All together, the SM knows 12 fermions: six quarks and six leptons. In Figure 2.1 the quarks are coloured purple and the leptons green. Based on the weak isospin, one can assign each fermion to a partner to form a so-called doublet in which one partner has a third component of the weak isospin $+1/2$ and the associated partner $-1/2$.

In Figure 2.1 the up and the down quark form a doublet and so do the charm and the strange quark as well as the top and the bottom quark. Within the quark sector, the so-called up-type quarks u, c and t have an electric charge $Q = +2/3$ whereas the down-type quarks d, s and b have $Q = -1/3$. One often refers to the three doublets as the three generations of the quark sector. The same applies to the lepton sector where the electron neutrino and the electron form the weak isospin doublet of the first generation, the muon neutrino and the muon and finally the tau neutrino and the tau lepton are representing the second and the third generations, respectively.

In Figure 2.1 the doublet partners are arranged such that isospin $+1/2$ particles, the up-type quarks and the neutrinos are located above their $-1/2$ isospin partners, the down-type quarks, the electron, the muon and the tau lepton. The latter three have $Q = -1$.

In the SM as it is described above, all constituents, 12 fermions and 4 bosons, are assumed to be massless. However, one knows from experimental results that they are not.

Table 2.1 shows all fermions and their respective properties. For the bosons please refer to Table 2.2. Additionally one knows that the particle's masses within the two sectors increase with generation. Except for the neutrino masses which are so small that they are assumed to be massless in the SM even though they have been experimentally proven to have non-zero mass. Amongst the bosons it is the $W^{\pm}$ and Z bosons that have mass whereas the photon and the gluon are massless.

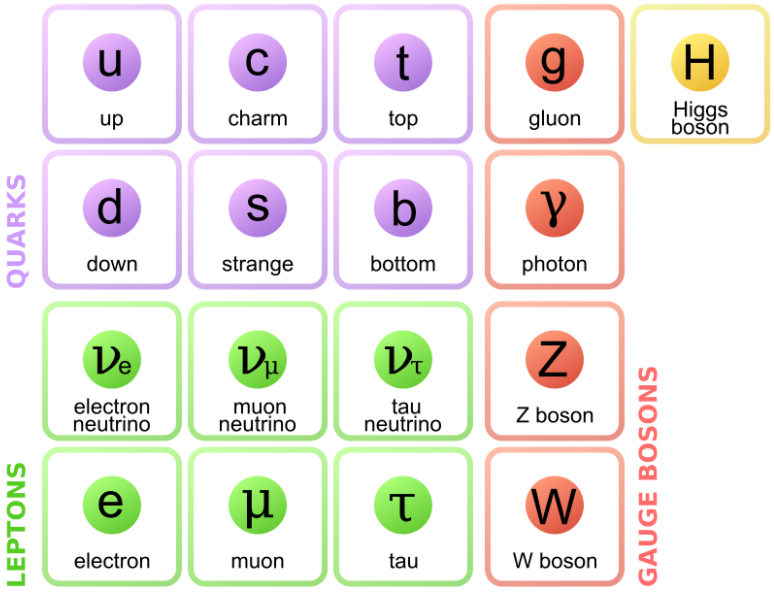

Figure 2.1.: The constituents of the Standard Model of Elementary Particle Physics.

Generation	Leptons			Quarks		
	Flavour	Q/e^2	Mass/GeV	Flavour	Q/e	Mass/GeV
1^{st}	ν_e	0	$< 10^{-9}$	u (up)	$+2/3$	$\sim 3 \cdot 10^{-3}$
	e^-	-1	$511 \cdot 10^{-6}$	d (down)	$-1/3$	$\sim 5 \cdot 10^{-3}$
2^{nd}	ν_μ	0	$< 10^{-9}$	c (charm)	$+2/3$	~ 1.3
	μ^-	-1	$106 \cdot 10^{-3}$	s (strange)	$-1/3$	~ 0.1
3^{rd}	ν_τ	0	$< 10^{-9}$	t (top)	$+2/3$	173.34
	τ^-	-1	1.78	b (bottom)	$-1/3$	4.5

Table 2.1.: Fermion properties in the Standard Model [8].

To solve this problem, one can implement the Brout-Englert-Higgs mechanism [3–5] into the theory of the SM to generate masses of the elementary particles. Here, an additional field is introduced, the Higgs field, and all massive particles acquire their mass through interaction with this field. Since elementary particles are excitations of their respective fields, one consequently suggested the existence of a scalar Higgs boson as excitation of the Higgs field which was actually discovered in 2012 [6, 7].

[2] $e := |Q_{electron}|$

Boson	Mediated Force	Q/e	Mass/GeV
γ (photon)	electromagnetic	0	0
$W^{\pm}$	weak	± 1	80.38
Z		0	91.19
g (gluons)	strong	0	0
H (Higgs)	–	0	125.09

Table 2.2.: Boson properties in the Standard Model [8].

2.2.1. Mathematical Concept of the Standard Model

In classical dynamics the Lagrange equation or Lagrangian

$$L\left(q_i, \dot{q}_i\right) = T - V \tag{2.1}$$

determines the equations of motion where T is the kinetic energy and V the potential energy of the system. It depends on the generalised coordinates q and their derivatives $\dot{q}$. From the Lagrangian, one can obtain the Euler-Lagrange equations to describe how the system behaves in time. Therefore, they are also called the equations of motion,

$$\frac{\mathrm{d}}{\mathrm{d}t}\left(\frac{\partial L}{\partial \dot{q}_i}\right) - \frac{\partial L}{\partial q_i} = 0\,. \tag{2.2}$$

The SM is mathematically described by Quantum Field Theory (QFT). One therefore substitutes the generalised coordinates by fields $\phi_i\left(t, x, y, z\right)$ and their derivatives. Hence the Lagrangian of 2.1 becomes the Lagrangian density $\mathcal{L}$

$$L\left(q_i, \dot{q}_i\right) \rightarrow \mathcal{L}\left(\phi_i, \partial_\mu \phi_i\right) \equiv \mathcal{L}\left(\phi_i, \frac{\partial \phi_i}{\partial x^\mu}\right) \tag{2.3}$$

where $x^\mu = (t, x, y, z)$ is the four vector defining one point in space-time and $\partial\phi_i/\partial x^\mu$ represents the derivative of the field ϕ_i with respect to its four space-time coordinates.

To get the Lagrange equation L out of the Lagrange density one needs to calculate the integral $L = \int \mathcal{L}\ \mathrm{d}^3\mathbf{x}$ with the spatial vector $\mathbf{x}$.

In the next step, one can show that the equivalent of Equation 2.2 for the field ϕ_i is

$$\partial_\mu\left(\frac{\partial \mathcal{L}}{\partial\left(\partial_\mu \phi_i\right)}\right) - \frac{\partial \mathcal{L}}{\partial \phi_i} = 0 \tag{2.4}$$

by using the principle of least action. Applying the principle of least action means that one minimizes the action functional S. For completion reasons, S is

defined as follows,

$$S\left[\phi_i\right] = \int_{t_1}^{t_2} L\left[\phi_i, \partial_\mu \phi_i\right] \, \mathrm{d}t \, . \tag{2.5}$$

In quantum mechanics particles are described by wavefunctions. In QFT a particle is the excitation of a quantum field which means that the characteristics of the particle must be contained in the field ϕ_i already and hence must be contained in the structure of the Lagrangian density. Consequently, the Lagrangian density is different for spin-half fermions, spin-one bosons or spin-zero particles.

The Lagrangian density $\mathcal{L}$ is further on referred to as *Lagrangian* because the actual Lagrangian $L = \int \mathcal{L} \, \mathrm{d}^3\mathbf{x}$ does not occur any more.

It is important that the Lagrangian in QFT is not derived from a certain theory or principle but is rather axiomatic. One needs to *find* the Lagrangian that holds for the case one is trying to describe. Three examples are given below to describe particles of different spin as free-particles, e.g. without considering interactions.

Relativistic spin-half fields

As described in Section 2.2, most of the SM particles are spin-half fermions. To find the corresponding Lagrangian means that the Euler-Lagrange equation describing the dynamics of this system is identified to be the free-particle Dirac equation,

$$i\gamma^\mu \left(\partial_\mu \psi\right) - m\psi = 0 \tag{2.6}$$

The field that is able to describe a spin-half fermion, e.g. the solution for the free-particle Dirac equation is a four-component complex spinor of the form $\psi\left(x\right) = \left(\psi_1, \psi_2, \psi_3, \psi_4\right)$. The components represent four orthogonal plane wave solutions. Two of them represent particle solutions while the other two represent antiparticle solutions. The general structure of the solutions is as follows

$$\psi_i = u_i\left(E, \mathbf{p}\right) \cdot e^{i(\mathbf{p}\cdot\mathbf{x} - Et)} \, . \tag{2.7}$$

In this four-component spinor, the upper two components of the particle solutions and the lower two components of antiparticle solutions describe the spin quantisation axis which is chosen to have the same direction as the particle's motion through space. The remaining two components describe the kinematics of the respective particle. All solutions only depend on the four-momentum vector p_μ.

The Lagrangian associated to the free-particle Dirac equation is

$$\mathcal{L}_D = i\overline{\psi}\gamma^\mu\partial_\mu\psi - m\overline{\psi}\psi \,. \tag{2.8}$$

Relativistic vector fields

To obtain the field equations for massive spin-one particles one starts with the so-called Proca Lagrangian

$$\mathcal{L}_{Proca} = -\frac{1}{4}F^{\mu\nu}F_{\mu\nu} + \frac{1}{2}m_\gamma^2 A^\mu A_\mu \,. \tag{2.9}$$

Here, A^μ is the electromagnetic field $A^\mu = (\phi, \boldsymbol{A})$ and $F^{\mu\nu}$ is the field-strength tensor from which Maxwell's equations of electrodynamics can be derived, describing the dynamics of this system.

From the Proca Lagrangian one can obtain the field equations of massive spin-one particles. In case of Quantum Electro-Dynamics (QED) one has to set the mass m_γ^2 to zero and $\mathcal{L}_{Proca}$ becomes $\mathcal{L}_{EM}$ with the photon as spin-one force carrier. One cannot use Equation 2.9 directly to describe the gluon which is also a massless spin-one particle because there are 3 gluon colour states. Therefore three new vector fields $\boldsymbol{A_\mu} = \left(A_1^\mu, A_2^\mu, A_3^\mu\right)$ need to be introduced. Due to the principle of gauge invariance which is explained in more detail in Section 2.2.1 the interaction between A_1^μ, A_2^μ and A_3^μ makes an additional term necessary.

Relativistic spin-zero fields

This paragraph can be considered as an introduction to the following Section 2.2.1 where a scalar boson is introduced to the SM as a consequence of the Brout-Englert-Higgs mechanism which generates the masses for the massive SM particles. Such a scalar spin-zero particle is the excitation of a scalar field ϕ fulfilling the Klein-Gordon equation

$$\partial_\mu\partial^\mu\phi + m^2\phi = 0 \,. \tag{2.10}$$

Therefore the Lagrangian has to have the form

$$\mathcal{L}_\mathcal{S} = \frac{1}{2}\left(\partial_\mu\phi\right) - \frac{1}{2}m^2\phi^2 = 0 \tag{2.11}$$

so that after calculating the partial derivatives of Equation 2.10 and substituting them into the Euler-Lagrange equation 2.2 one obtains Equation 2.11.

Principle of Local Gauge Invariance

The underlying mathematical principle of the SM is the invariance of the Lagrangian under *local gauge transformation*. Invariance in mathematics means that a system is symmetric under a certain transformation of the reference frame.

It is important to distinguish between *global* invariance and *local* invariance. In a system with a *global* symmetry, every point transforms under the exact same conditions. Hence, the wavefunction needs to satisfy the relation

$$\psi \longrightarrow \psi' = e^{i\theta}\psi \, . \tag{2.12}$$

Requiring a *local* symmetry means that one allows all individual points of the system to transform differently. Consequently the transformation needs to depend on a local phase $q\chi\left(x\right)$ so that

$$\psi\left(x\right) \longrightarrow \psi'\left(x\right) = e^{iq\chi(x)}\psi\left(x\right) \, . \tag{2.13}$$

For example one can consider a circle with a rotational symmetry around the origin. A *global* transformation could lead every point on the circle to rotate by the same angle in the same direction. The circle remains the same afterwards. In contrast, applying a *local* transformation means that every point can rotate with a different angle, e.g. the circle could be transformed into a semi- or even a quarter-circle.

Now, a new component must be introduced so that the transformation is still symmetric, the so-called *gauge field*. It 'counteracts' the local phase, hence, in the new reference frame the physical laws described by the wavefunction ψ stay the same.

One example is the free-particle Dirac Lagrangian, Equation 2.8, that after introducing the new component A_μ becomes

$$\mathcal{L} = \overline{\psi}\left(i\gamma^\mu\partial_\mu - m\right)\psi - q\overline{\psi}\gamma^\mu A_\mu\psi \, , \tag{2.14}$$

where the gauge field A_μ needs to obey the transformation

$$A_\mu \longrightarrow A'_\mu = A_\mu - \partial_\mu\chi \tag{2.15}$$

and the derivative ∂_μ must be substituted by the *covariant derivative* D_μ,

$$\partial_\mu \longrightarrow D_\mu = \partial_\mu + iqA_\mu \,, \tag{2.16}$$

when the transformation to the new reference frame is conducted.

The 'counteraction' of the gauge field is represented by the derivative $\partial_\mu \chi(x)$ acting on the local phase. Via the mechanism of *local gauge invariance* it is possible to rewrite the free-particle Lagrangians described above in Equations 2.8, 2.9 and 2.11 such, that they allow the respective particles to interact.

Thus, it is possible to generate the fields for the photon as the mediator of the electromagnetic force, the gluons for the strong force and the $W^{\pm}$ and the Z bosons for the weak interaction. All symmetries describing the SM are continuous.

Emmy Noether discovered in 1918 that for every continuous symmetry there is a conserved quantity [9]. Indirectly *Noether's theorem* is already hidden in Equation 2.14. The conserved quantity is represented by the factor q.

The Symmetries of the SM and Electroweak Symmetry Breaking

The fundamental symmetry of the SM is $\mathrm{U}(1)_Y \times \mathrm{SU}(2)_L \times \mathrm{SU}(3)_C$.

- $\mathrm{SU}(3)_C$ is the symmetry group describing the strong force or *Quantum Chromo Dynamics* (QCD). The index 'C' and the word 'Chromo' refers to the conserved quantity of QCD, the 'colour' charges red, blue and green. To construct the $\mathrm{SU}(3)_C$ symmetry group eight generators are required, the Gell-Mann matrices. Consequently, eight massless gluons mediate the strong force, each of which carrying a combination of two colour charges. Besides gluons, only quarks carry colour charge. Antiquarks carry the anticolour charges, antired, antiblue and antigreen.

- $\mathrm{SU}(2)_L$ is the symmetry group describing the chiral part of the weak interaction expressed by the index 'L'. The flavour changing charged current of the weak interaction mediated by the $W^{\pm}$ bosons only couples to left-handed particles and right-handed antiparticles. To get the left- and right-handed parts from a spinor one needs to multiply with the chiral projection operators $P_R = \frac{1}{2}\left(1+\gamma^5\right)$ and $P_L = \frac{1}{2}\left(1-\gamma^5\right)$ for right- and left-handed components, respectively. For the full description of the $\mathrm{SU}(2)_L$ group another field W^3_μ is needed which is neutral and mixes with the $\mathrm{U}(1)_Y$ group described below to form the Z boson and the photon.

- $\mathrm{U}(1)_Y$ is the symmetry group with the weak hypercharge 'Y' as the conserved quantity. The weak hypercharge is defined as $Y = 2\left(Q - T^I_3\right)$ with the electric charge Q and the third component of the weak isospin T^I_3. Glashow, Weinberg and Salam unified the theories of electromagnetism and weak force into the GSM model of electroweak interactions [10–13]. Here, the photon and the Z boson are linear combinations of the neutral weak current from $\mathrm{SU}(2)_L$ and the gauge field B_μ of the $\mathrm{U}(1)_Y$ gauge group. The photon and Z boson fields can hence be written as

$$A_\mu = +B_\mu \cos\theta_W + W^3_\mu \sin\theta_W \,, \tag{2.17}$$

$$Z_\mu = -B_\mu \sin\theta_W + W^3_\mu \cos\theta_W \,, \tag{2.18}$$

  with a Weinberg angle of $\theta_W \simeq 30^\circ$ which is often referred to as *weak mixing angle*.

As described in Section 2.2, measured masses. In the SM, particle masses can be generated via the interaction with the Higgs field via the Brout-Englert-Higgs mechanism. This process is breaking the $\mathrm{U}(1)_Y \times \mathrm{SU}(2)_L$ symmetry of the SM to generate the masses for the $W^{\pm}$ and the Z bosons as well as the mass for the scalar Higgs boson.

Therefore, four degrees of freedom are required, two of which being neutral and two being charged. They are represented in a charged and a neutral complex scalar field. To embed the mechanism into the electroweak theory a weak isospin doublet is needed,

$$\phi = \begin{pmatrix} \phi^+ \\ \phi^0 \end{pmatrix} = \frac{1}{\sqrt{2}} \begin{pmatrix} \phi_1 + i\phi_2 \\ \phi_3 + i\phi_4 \end{pmatrix} . \tag{2.19}$$

In Section 2.2.1 the Lagrangian for a scalar field was introduced already and therefore one can write

$$\mathcal{L}_{Higgs} = \left(\partial_\mu \phi\right)^\dagger \left(\partial^\mu \phi\right) - \left(\mu^2 \phi^\dagger \phi + \lambda \left(\phi^\dagger \phi\right)^2\right) , \tag{2.20}$$

for the additional terms being added to the SM Lagrangian to include the Higgs field.

2.3. Top Quark Physics

In the following, the special position of the top quark in the SM is discussed in more detail to motivate the search presented in this report.

As it was already introduced at the beginning of Section 2.2, the top quark is the weak isospin partner of the bottom quark. Together they form the weak isospin doublet of the third quark generation with $Q_t = +2/3$, $T_{3,t} = +1/2$ and $Q_b = -1/3$, $T_{3,b} = -1/2$, with the electric charge Q and the third component of the weak isospin T_3 of the top and bottom quark, respectively.

By the current state of research, the top quark is the heaviest known particle in the SM. After its discovery in 1995, the DØ and CDF experiments at the TEVATRON proton-antiproton collider near Chicago conducted its mass measurements at $\sqrt{s} = 1.8$ TeV and $\sqrt{s} = 1.96$ TeV.

After analysing much more events produced by the Large Hadron Collider (LHC) near Geneva the statistical uncertainty of the measurements could be reduced. Even more sophisticated analysis tools and better detection techniques of the ATLAS and CMS experiments could also reduce the systematic uncertainty.

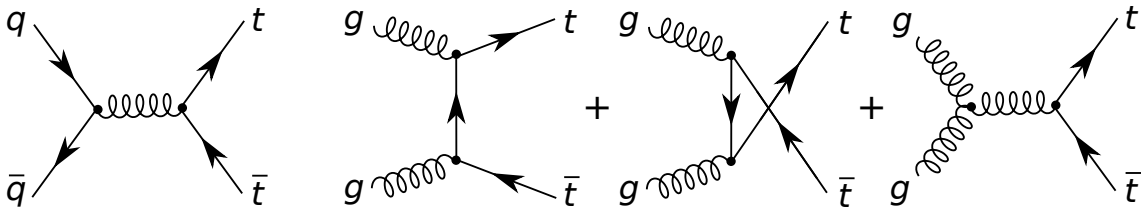

Figure 2.2.: Feynman diagrams showing top quark strong production.

This effort leads to the latest top mass value of $m_{\text{top}} = 173.34 \pm 0.27\,(\text{stat.}) \pm 0.71\,(\text{sys.})$ GeV [14] which is a combined result of the DØ, CDF, ATLAS and CMS collaborations. This combination uses TEVATRON data of up to 8.7 fb^{-1} at $\sqrt{s} =$ 1.96 TeV and up to 4.9 fb^{-1} of LHC data at $\sqrt{s} = 7$ TeV.

2.3.1. $t\bar{t}$ Production

At hadron colliders like the TEVATRON or the LHC, top quarks can be produced in strong interactions as top-antitop pairs or via the electroweak interaction as single top quarks. The leading order Feynman diagrams for the strong production are shown in Figure 2.2.

On the left side, a quark and an antiquark annihilate and form a $t\bar{t}$ pair via a gluon in the s-channel process $q\bar{q} \rightarrow t\bar{t}$. The remaining three diagrams show gluon fusion production $gg \rightarrow t\bar{t}$ described from left to right. Three leading order diagrams are possible: a t-channel and u-channel production and the case, when the initial state gluons form a triple gluon vertex (triple gauge coupling) leading to a $t\bar{t}$ pair which is again an s-channel process.

Figure 2.3 shows the theory prediction and the measurements for the $t\bar{t}$ production cross section at the TEVATRON and the LHC in pb for different centre of mass energies. One can see that for low $\sqrt{s}$, the theory prediction for $p\bar{p}$ is higher in comparison to pp. At low $\sqrt{s}$, the proton/antiproton momentum is mainly shared by the valence quarks and therefore the TEVATRON as a $p\bar{p}$ collider has a higher chance to produce a $t\bar{t}$ pair due to quark-antiquark annihilation. The measurements by the TEVATRON experiments CDF and DØ show good agreement with the theoretical prediction at $\sqrt{s} = 1.8$ TeV, $\sqrt{s} = 1.96$ TeV and at $\sqrt{s} = 13$ TeV.

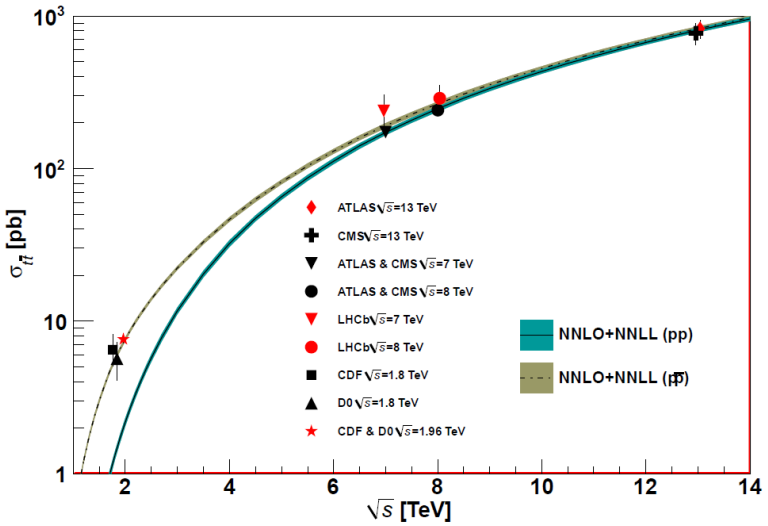

Figure 2.3.: Production cross section for $t\bar{t}$ at the TEVATRON in $p\bar{p}$ and at the LHC in pp collisions for varying energies. The theoretical prediction is taken from [15] with an assumed top quark mass of $m_t = 172.5$ GeV. It agrees within uncertainties with the measured values of the TEVATRON experiments DØ and CDF at $\sqrt{s} = 1.8$ TeV [16, 17] and $\sqrt{s} = 1.96$ TeV [18–20]. Also the measurements of the ATLAS [21–23], CMS [24, 25] and LHCb [26] experiments at the LHC show agreement with the prediction.

For higher $\sqrt{s}$, the theoretical predictions for $p\bar{p}$ and pp converge because the density of the sea quarks and gluons inside the protons/antiprotons is higher than for the valence quarks. Also the momentum fraction of the valence quarks decreases. Therefore, the production processes via $gg \rightarrow t\bar{t}$ become the dominant ones.

Also the measurements of CMS and ATLAS agree with the theory expectation for $\sqrt{s} = 7, 8$ and 13 TeV. The theory model assumed $m_{top} = 172.5$ GeV and the calculated cross section is $\sigma_{t\bar{t}} = 173.6^{+4.5+8.9}_{-5.9-8.9}$ pb for $\sqrt{s} = 13$ TeV.

2.3.2. $t\bar{t}$ Decay

The top quark decays in almost all cases into a W boson and a b quark because the CKM-matrix element $|V_{tb}|$ is almost 1. Subsequently, the W boson decay products define the final signature of the top quark decay in the detector. For $t\bar{t}$ this leads to three decay modes:

- with both W bosons decaying hadronically via $t\bar{t} \to W^+bW^-\bar{b} \to q\bar{q}'bq''\bar{q}'''\bar{b}$, referred to as *all-jets channel* .
- with the W bosons decaying hadronically and leptonically respectively via $t\bar{t} \to W^+bW^-\bar{b} \to q\bar{q}'bl^-\bar{\nu}_l\bar{b} + l^+\nu_l bq''\bar{q}'''\bar{b}$, referred to as *lepton + jets* $(l + \text{jets})$ *channel*.
- with both W bosons decaying leptonically via $t\bar{t} \to W^+bW^-\bar{b} \to l^+\nu_l bl'^-\bar{\nu}_{l'}\bar{b}$, referred to as *dilepton* (ll) *channel* .

Each of the decay channels has different branching ratios as stated in Figure 2.4. The $\ell +$ jets and all-jets channels have the highest branching ratios but in the latter one needs to distinguish the jets and associate them to the respective top quark to make a measurement while having high background contributions. For the $\ell +$ jets channel one can get good discrimination between background and signal processes and the lepton can often be clearly identified leading to good results. In the dilepton channel the problem is the missing energy carried away by two different neutrinos even though the two leptons again can give a clear signature, also because the background is low.

2.4. The $t\bar{t}Z$ Process

2.4.1. Motivation to Study $t\bar{t}Z$

Studying the coupling of top quarks to the vector bosons of the weak interaction is an important test of the SM. As already mentioned in Section 2.3, the top quark can be studied as a bare quark because it decays before hadronisation after being produced in a collider. Hence, one can directly study the coupling of the top quark and the Z bosons.

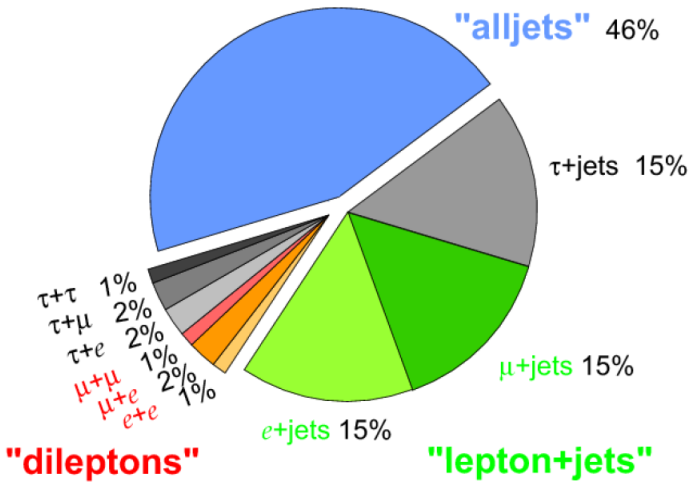

Figure 2.4.: Top quark decay pie chart.

With a dilepton final state that is focused on in this text, one is sensitive to $t\bar{t}W$ with a W boson being emitted as initial state radiation and $t\bar{t}Z$ as final state radiation. For $t\bar{t}W$ one usually focuses on the dilepton same sign channel whereas for $t\bar{t}Z$ the opposite sign dilepton channel is interesting, though, discrimination between signal and background events is difficult.

At the tZ vertex one is sensitive to the vector−axial-vector coupling of the weak neutral current and thus can infer the third component of the weak isospin of the top quark T_t^3. As explained in Section 2.3, the value of T_t^3 determines whether the top and the bottom quark are partners in the weak isospin doublet of the third generation of the quark sector.

In the SM Lagrangian the coupling to the Z boson is given by

$$\mathcal{L}_{t\bar{t}Z} = \frac{e\overline{u}\left(p_t\right)\gamma^{\mu}}{2\sin\theta_W\cos\theta_W}\left(C_V - \gamma_5 C_A\right)v\left(p_{\bar{t}}\right)Z_{\mu} \tag{2.21}$$

with the vector and axial vector couplings

$$C_A = T_t^3 \quad \text{and} \quad C_V = T_t^3 - 2Q_t\sin^2\theta_W\,. \tag{2.22}$$

In case the couplings show a significant deviation from the theoretical prediction of the SM this is an indicator for physics beyond the SM.

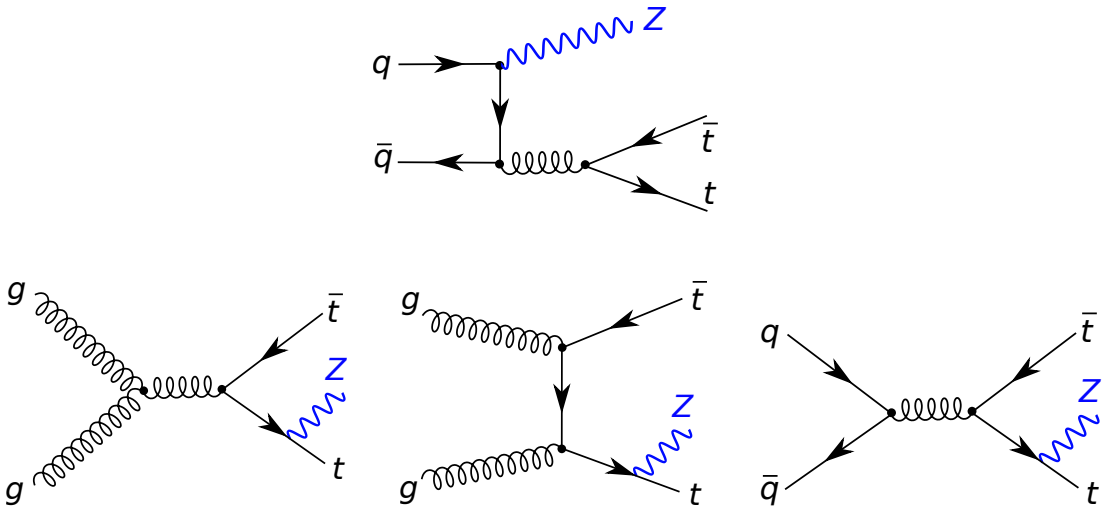

Figure 2.5.: Leading order Feynman diagrams of $t\bar{t}Z$ production at hadron colliders. The Z boson is either radiated off as initial state radiation (upper row) or final state radiation (bottom row). Only in the last case one is sensitive to the tZ coupling vertex.

2.4.2. $t\bar{t}Z$ Production Mechanisms at the LHC

Figure 2.5 shows leading order Feynman diagrams for $t\bar{t}Z$ production at hadron colliders. In the upper row the Z boson is produced as initial state radiation (ISR) from an incoming quark. This process is not sensitive to the tZ coupling.

On the other hand the Z boson is radiated off from final state top quarks in the bottom row of Figure 2.5. A process called final state radiation (FSR) in contrast to the ISR process is sensitive to the tZ interaction vertex.

The two diagrams on the left in the bottom row show $t\bar{t}Z$ production with initial state gluons. In the left diagram, they form a triple gauge coupling vertex and the top quark pair is produced in an s-channel process. The diagram in the middle shows a t-channel and the right shows again an s-channel process with the difference that the initial state particles are a quark and an antiquark. They annihilate and produce the final state particles in an s-channel process via a gluon.

Figure 2.6 shows the production cross section of $t\bar{t}Z$ as a function of $\sqrt{s}$ in comparison to $t\bar{t}H$ and $t\bar{t}W^{\pm}$. The cross section for $t\bar{t}Z$ is always higher than the other processes and reaches $\sigma_{t\bar{t}Z} = 759.8 \pm 2.6^{+9.7\%}_{-11.1\%}\,(\text{scale})^{+1.9\%}_{-2.2\%}\,(\text{PDF})$ fb at $\sqrt{s} = 13$ TeV for the NLO calculation [27].

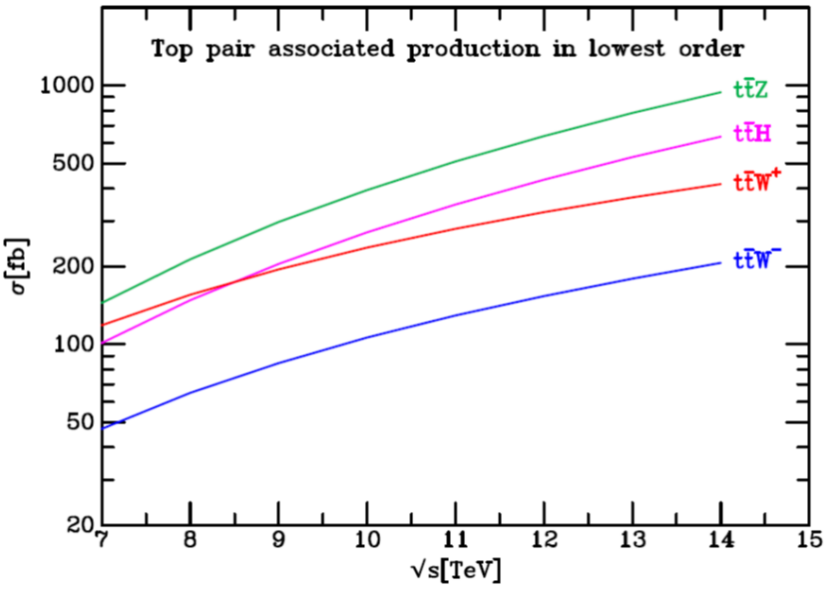

Figure 2.6.: Production cross sections of $t\bar{t}Z$, $t\bar{t}W^{\pm}$ and $t\bar{t}H$ as a function of the center of mass energy. The assumed Higgs mass is $m_H = 125$ GeV. The graph is taken from [28].

2.4.3. Previous Analyses of $t\bar{t}Z$

The first searches for the $t\bar{t}Z$ process were performed by the ATLAS and CMS experiments at $\sqrt{s} = 7$ TeV with integrated luminosities of 4.7 fb^{-1} and 5.0 fb^{-1}, respectively, which are the complete data sets available at that energy.

While ATLAS sets an upper limit on the $t\bar{t}Z$ cross section of $\sigma_{t\bar{t}Z} < 0.71$ pb at 95% [29] confidence level searching for a three-lepton final state, CMS performed a combined search of $t\bar{t}Z$ and $t\bar{t}W$. For $t\bar{t}Z$ they also looked at final states with three leptons leading to a measured cross section of $\sigma_{t\bar{t}Z} = 0.28^{+0.14}_{-0.11}\,(\text{stat.})^{+0.06}_{-0.03}\,(\text{syst.})$ pb observed with a significance of 3.3 standard deviations from the background only hypothesis[30]. At the same time this result was the first evidence for the $t\bar{t}Z$ process.

The next measurements of the $t\bar{t}Z$ coupling were performed at $\sqrt{s} = 8$ TeV by ATLAS and CMS with 20.3 fb^{-1} and 19.5 fb^{-1}, respectively. ATLAS measured $\sigma_{t\bar{t}Z} = 176^{+58}_{-52}$ fb at 7.1 σ CL [31] and CMS measured $\sigma_{t\bar{t}Z} = 242^{+65}_{-55}$ fb at 6.4 σ CL [32].

Also for the LHC Run II (preliminary), results from ATLAS and CMS are available already. The ATLAS result is $\sigma_{t\bar{t}Z} = 0.92 \pm 0.30\,(\text{stat.}) \pm 0.11\,(\text{sys.})$ pb with 3.2 fb^{-1} [33] and the CMS result is $\sigma_{t\bar{t}Z} = 1065^{+352}_{-313}\,(\text{stat.})^{+168}_{-142}\,(\text{sys.})$ fb with 2.7 fb^{-1} with an exclusion of 3.6 σ from the background-only hypothesis [34].

3. Experimental Setup

3.1. The Large Hadron Collider

The Large Hadron Collider (LHC) is part of the particle accelerator complex of the European Organization for Nuclear Research (CERN) at the Swiss-French border near Geneva. The CERN Council gave the approval for the LHC Project in December 1994 [35] and it started operation in 2008. The LHC is a ring of superconducting magnets with a circumference of 27 kilometers in the tunnel of the former Large Electron Positron Collider (LEP) 100 meters underground.

It has two beam pipes to accelerate proton bunches in opposite directions up to a maximum design energy of 7 TeV per beam. By crossing the beams, the LHC delivers proton-proton collisions at four interaction points to the experiments ATLAS, CMS, LHCb and ALICE. In Run I the collision rate was 40 MHz corresponding to bunch crossings every 25 ns. ATLAS and CMS are multi-purpose detectors whilst LHCb is specialised on b-quark physics and ALICE is especially built to record heavy-ion collisions. Therefore, the LHC is as well able to accelerate lead ions to provide data for research on heavy-ion physics.

Before protons can be injected into the LHC they are pre-accelerated by a chain of different accelerators starting with the linear accelerator LINAC2 and followed by the ring-accelerators PROTON SYNCHROTON BOOSTER (PSB), the PROTON SYNCHROTRON (PS) before the SUPER PROTON SYNCHROTRON (PSP) supplies them to the LHC.

3.2. The ATLAS Detector

ATLAS is a multi-purpose particle detector taking data from proton-proton collisions of the Large Hadron Collider (LHC) at CERN, near Geneva. It is one of four experiments based at four different interaction points along the ring of the LHC. The second multi-purpose detector is the Compact Muon Solenoid (CMS). The others are LHCb and ALICE which were specially designed for b-quark physics and heavy-ion physics, respectively.

ATLAS is a toroidal detector with a symmetric barrel structure along the beam pipe and endcaps on both sides of the barrel to take data in a 4π solid angle around the interaction point in the middle of the detector. To be able to reconstruct single collisions, the ATLAS detector consists of different components, each designed for a special purpose. The different components are discussed in more detail below. The layer structure allows each of the components to record a special fraction of the information needed to understand what happened in the collisions.

In the coordinate system that is commonly used, the beam axis is defined as the z-axis. The toroid is then described by cylindrical coordinates using the angle ϕ in the plane perpendicular to the z-axis and the radius r defines the distance to that axis. Alternatively, one can use the coordinates x and y. Both are perpendicular to the z-axis, x pointing towards the centre of the LHC ring and y pointing upwards.

To describe collision events and particle's trajectories in a detector is the pseudorapidity

$$\eta \equiv -\ln\left[\tan\left(\frac{\theta}{2}\right)\right] \tag{3.1}$$

is used very often, with θ being the angle perpendicular to the r-ϕ plane. η is useful to describe particles boosted along the z-axis since intervals of η are Lorentz invariant under boosts along the z-axis. The other coordinates are not and even η itself is not invariant under Lorentz transformation. The pseudorapidity is an approximation for high jet energies compared to the jet mass. It is originally derived from the rapidity

$$y = \frac{1}{2}\ln\left(\frac{E + p_z}{E - p_z}\right) . \tag{3.2}$$

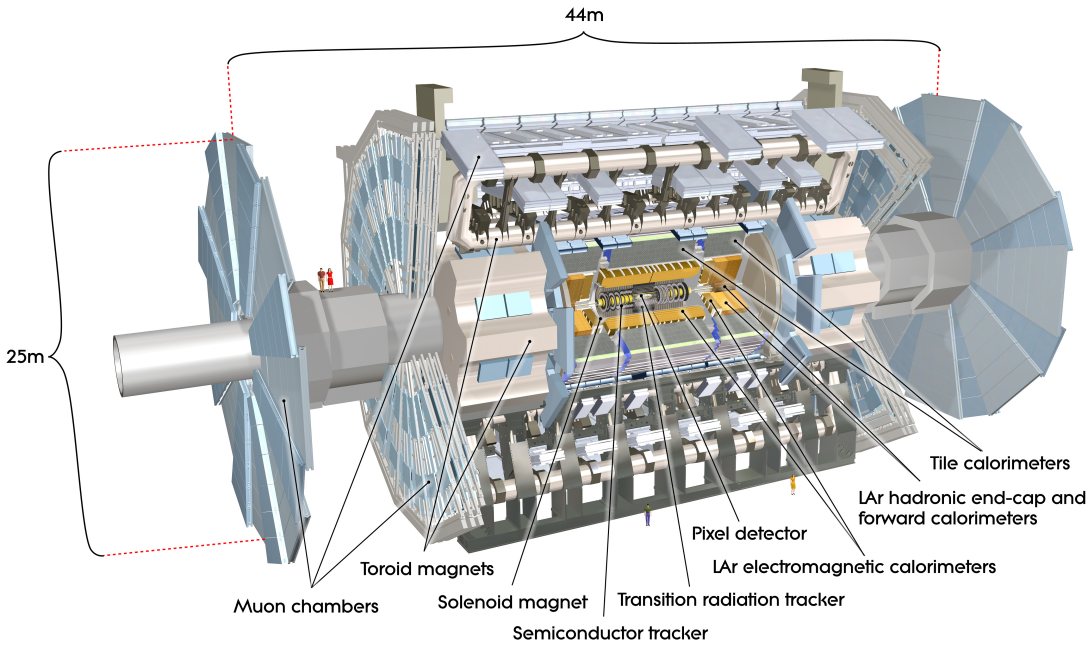

Figure 3.1.: Computer generated image of the ATLAS detector.

3.2.1. Magnet System

The ATLAS magnet system consists of two different super-conducting subsystems. A central solenoid (CS) surrounds the Inner Detector (ID) providing a central field strength of $2T$. The second system is of toroidal structure and placed between the outermost part of ATLAS, the muon system and the calorimeters.

The CS is 5.3 m long and has an inner diameter of 2.4 m. The peak field strength at the solenoid itself is 2.6 T. Because it is placed in front of the calorimeters the solenoid was designed to be as thin and as less of a resistance as possible to allow a high level performance of the calorimeters while still being reliable and safe. Therefore the CS shares a vacuum vessel with the Liquid Argon Calorimeter to save material. The CS provides a magnetic field for the Inner Detector to bend charged particles which is crucial for a high resolution momentum measurement. The bending is taking place in the r-ϕ-plane.

The outer system consists of three air-core toroids. The barrel toroid's length parallel to the beam pipe is 25.3 m having an outer and inner diameter of 20.1 m and 9.4 m, respectively. The other two toroidal components are placed at the end-caps and integrated into the barrel toroid. The combined magnetic field bends the muons passing through the calorimeters allowing muon momentum measurements combining the information of the muon system with the Inner Detector.

Each of the three toroidal systems consists of eight toroidal coils arranged symmetrically in ϕ-direction around the beam pipe. The end-cap toroids are shifted by 22.5° in ϕ-direction towards the barrel toroid. The purpose is to better integrate the systems geometrically and increase the bending power in the overlap regions. The peak field strength of the barrel and end-cap toroids is 4.1 T and 3.9 T, respectively.

In contrast to the CS the bending by the toroids takes place in the r-z-plane. The ATLAS Magnet System is indirectly cooled by liquid helium at 4.5 K.

3.2.2. Inner Detector

The Inner Detector (ID) is the component closest to the interaction point and consists of three subcomponents: Pixel Detector, Semiconductor Tracker (SCT) and Transition Radiation Tracker (TRT). All three are arranged in concentric layers around the beam axis, have a barrel and end-cap structure and are described in more detail below. The ID is operating in a 2 T magnetic field by the Central Solenoid described in Section 3.2.1. The overall dimensions of the ID are an outer radius of 115 cm and a length of 7 m.

The purpose of the ID is to provide high-resolution tracking information of the particles created in a proton-proton collision at high luminosity. Therefore the components need to cope with the higher radiation and track density the closer they are located to the interaction point. In this harsh environment high granularity and fast readout is required to allow vertexing of the primary interaction and high momentum resolution for charged particles via tracking.

Additionally, tracks created by penetrating muons are crucial to reconstruct the momentum of the muon which is only possible by combining this information with that of the muon system.

Pixel Detector

The Pixel Detector is the innermost part of the ATLAS detector and therefore requires the highest measurement precision despite operating in a harsh radiation environment.

The original Pixel Detector (Pixel) of ATLAS in Run I consisted of three layers of pixel modules made from silicon sensors. Due to higher luminosity in Run II causing higher radiation damage and a denser track environment the size of the beam pipe was decreased at the interaction point to implement a fourth pixel layer. The so-called Insertable B-Layer (IBL) is now operating as the innermost part of ATLAS with a radial extension of $31 < r < 40$ mm with respect to the z-axis.

IBL also compensates the loss in performance of the other pixel layers due to radiation damage and restores the full b-tagging capability.

Furthermore there are five pixel disks perpendicular to the z-axis at each end-cap. They are of the same kind as the barrel modules and have radii between 11-20 cm.

Semiconductor Tracker

The Semiconductor Tracker consists of eight layers of silicon micro-strip detectors in the barrel and nine disks for each of the end-caps each having three rings of strip sensors attached. Therefore it adds the equivalent number of hits to the track reconstruction.

One module consists of two detectors glued together and shifted by 40 mrad to form a grid structure. This geometry allows to identify ghost hits due to high occupancy. Strips in the barrel are 12.8 cm long while in the end-caps the length varies by radius from 12 cm at the outer layers to 6-7 cm at the inside.

The resolution of 16 μm in $R\phi$ and 580 μm in z direction is lower than for the Pixel Detector.

Transition Radiation Tracker

The Transition Radiation Tracker consists of straw tube detectors with a diameter of 4 mm filled with a gas mixture of Xe, CO_2 and CF_4. High response rates are guaranteed by each straw containing only one wire and the small diameter.

A radiator is added between the straws to detect transition radiation from penetrating electrons. Therefore the straw tube detectors have two thresholds. A lower value for tracking hits and a higher value for transition radiation hits. Additionally, every channel measures the drift time of the charge for a spatial information of the hit.

While the barrel straws are aligned axially, the end-cap straws are arranged radially. To better cope with the high occupancy, the barrel straws are divided into two parts in the middle with two read out channel at the ends. The end-cap straws are not divided and have a single read out at the outside.

3.2.3. Electromagnetic Calorimeter

The purpose of the Electromagnetic Calorimeter (ECal) is to stop photons and electrons and measure their energy. The ATLAS ECal is a sampling calorimeter with alternating layers of lead and liquid argon (LAr) having an accordion geometry. Lead serves as an absorber forcing the penetrating particles to shower electromagnetically. The electromagnetic showers ionise LAr and the generated charge moves towards electrodes attached to the LAr layer to process the signal.

The ECal is located behind the 2 T solenoid, though sharing the same vacuum vessel. To keep the argon liquid at -138° C, a barrel cryostat surrounds the ECal which is placed before the solenoid. Like the other detector components the ECal has a barrel part and an end-cap part. The barrel component is split into two individual barrels at $z = 0$ and the lead layer thickness changes with η to optimise the energy resolution. The thickness of the LAr layer stays constant in the barrel. The thickness of the barrel is measured in radiation lengths X_0 which is > 24.

In the end-caps, the wave amplitude of the accordion structure increases with radius. Therefore the absorber layer thickness stays constant but the LAr gaps become thicker. The end-caps are slightly thicker with $> 26X_0$. Furthermore, both end-cap ECals are divided into two coaxial wheels covering different η-regions. The end-caps share a cryostat with the hadronic endcap calorimeters and the forward calorimeters.

3.2.4. Hadronic Calorimeter

After the ECal stopped photons and electrons, the ATLAS Hadronic Calorimeter (HCal) stops mainly hadronically interacting particles that are able to penetrate the ECal. These particles are hadronic compounds that are forced to shower hadronically in the HCal.

The HCal can be separated in the hadronic tile calorimeter for the barrel and two parts for each of the end-caps, the hadronic end-cap calorimeter (HEC) and the high density forward calorimeter (FCAL).

The HCal has a thickness of 11 interaction lengths λ which is important to prevent punch-throughs of particles into the muon system. Because of the high coverage of $|\eta| < 4.9$ and the necessary 10 λ for good jet energy resolution the HCal is well suited for high precision E_T^{miss} measurements.

The tile calorimeter is a sampling calorimeter with layers of iron absorbers and scintillating samples. The scintillating light is transported to photomultipliers (PMTs) via wavelength shifting fibres and transformed into an electronic signal by the read out electronics. The whole barrel part is segmented into a central barrel and two extended barrels further outside.

The HEC detectors use copper plates as absorber material and the sampling layers are using the same LAr technique as the ECal. Each HEC is divided into 2 parts that differ in the thickness of the copper plates. The plates are 25 mm and 50 mm thick for the inner and the outer component, respectively. The LAr gap is 8.5 mm long and divided into four drift areas by implementing 3 electrodes with the middle one for the readout.

The FCAL is the closest to the beam pipe and is highly irradiated by a running LHC because of many infrared, small-angle hadronic interactions while crossing beams. This is why also here the radiation hard LAr technique is employed. It is divided into three sections. The one closest to the interaction point is made of copper as absorber material and the other two are using tungsten. Compared to the HEC, the LAr gaps of only 250 μm in the first component and 375 μm in the remaining two are much thinner.

3.2.5. Muon System

The ATLAS Muon System (MS) is the outermost part of the detector to perform precise track measurements of muons and to also provide trigger information. Therefore the MS consists of two categories of detectors. Monitored Drift Tubes (MDTs) and Cathode Strip Sensors (CSS) located in barrel and end-caps respectively are used for tracking. Resistive Plate Chambers (RPC) and Thin Gap Chambers (TGC) provide trigger information again used in the barrel and end-caps respectively.

As mentioned in Section 3.2.1 the toroidal magnet system creates the magnetic field for bending the muons to the necessary extend. The barrel toroid is responsible for bending within a region of $|\eta| \leq 1.0$ whereas for high regions of $1.4 \leq |\eta| \leq 2.7$ the end-cap toroids are delivering the magnetic field for bending. In the transition region $1.0 \leq |\eta| \leq 1.4$ the overlapping fields of barrel and end-cap toroids are responsible for bending the muon trajectories.

The barrel consists of three concentric layers measuring muon tracks whereas there are four such layers in the end-caps. While the barrel measures the φ- and z-coordinate the end-caps measure φ and the radius r. The trigger system has a higher time resolution than the LHC bunch crossing interval of 25 ns. It allows to trigger events on the p_T of the respective muon which is important for classifying events into relevant or irrelevant depending on the analysis.

4. Data Sets and Analysis Objects

4.1. Data Samples

The data used for these studies was produced by the LHC between 15$^{\text{th}}$ August and 15$^{\text{th}}$ November 2015 at a center of mass energy of $\sqrt{s}$= 13 TeV and was recorded by the ATLAS detector corresponding to an integrated luminosity of $\int \mathcal{L}\, \mathrm{d}t = 3.2\ \mathrm{fb}^{-1}$.

4.2. Monte Carlo Simulation

The signal and background are modelled with Monte Carlo (MC) simulations. This is done in several steps: Events are generated on parton-level and subsequently dressed with a parton shower before the hadronisation process is simulated. These events are then passed through a detector simulation.

This section provides the details of the MC production and includes the $t\bar{t}Z$ signal as well as the two main backgrounds Z+jets and $t\bar{t}$ (for more information on the topology see Section 5.3). Furthermore there are contributions from $t\bar{t}$, $t\bar{t}H$, single-top quark and diboson (WW, WZ, ZZ) production.

While for the detector response GEANT [36, 37] is used the underlying event simulation and the showering and hadronisation can be performed by different tools. SHERPA [38–40] for example can also complete the whole simulation chain without an additional step.

When talking about Monte Carlo samples it is always important to mention to which order of perturbation theory the calculation of the matrix element was done to avoid complications especially when combining two tools for separate steps.

The reason is that higher order perturbation theory calculations have a lower factorisation scale uncertainty and are therefore expected to be more precise.

For the $t\bar{t}$ and the single-top quark production POWHEG-BOX [41–44] is used for the Wt and s-channel event generation with the parton density function (PDF) sets CT10 at NLO. Afterwards PYTHIA 6 [45] is used for the parton shower, fragmentation and the underlying event simulation is done with the CTEQ6L1 PDF set and the Perugia 2012 (P2012) [46] tune. Here, the value for the mass of the top quark is $m_{\text{top}} = 172.5$ GeV.

MG5_aMC@NLO [47] is used for the generation of the $t\bar{t}W$ and the $t\bar{t}Z$ samples at leading order with a subsequent simulation of the shower and hadronisation with PYTHIA 8 [48]. The A14 tune with the PDF set NNPDF2.3LO [49] is used in PYTHIA 8.

For $t\bar{t}H$, events at NLO are produced with MG5_aMC@NLO, using the PDF sets CT10. The PDF for the showering was CTEQ6L1 produced with HERWIG++ [50].

Furthermore, for all samples described above the EVTGEN [51] program is used for the simulation of the hadronic decays of the charm and the bottom quark.

Events containing W or Z bosons with associated jets are simulated using the SHERPA 2.1.1 [52] generator. Matrix elements are calculated for up to 2 partons at NLO and 4 partons at LO using the COMIX [53] and OPENLOOPS [54] matrix element generators and merged with the Sherpa parton shower [55] using the ME+PS@NLO prescription [56]. The CT10 PDF set is used in conjunction with dedicated parton shower tuning developed by the Sherpa authors. The W/Z+jets events are normalized to the NNLO cross sections.

Diboson processes with 4 charged leptons, 3 charged leptons + 1 neutrino or 2 charged leptons and 2 neutrinos are simulated using the SHERPA 2.1.1 generator. Matrix elements contain all diagrams with four electroweak vertices. They are calculated for up to 1 $(4l, 2l + 2\nu)$ or 0 partons $(3l + 1\nu)$ at NLO and up to 3 partons at LO using the COMIX and OPENLOOPS matrix element generators and merged with the SHERPA parton shower using the ME+PS@NLO prescription. The CT10 PDF set is used in conjunction with dedicated parton shower tuning developed by the SHERPA authors. The generator cross sections are used in this case (already at NLO).

Sample	Generator	Shower	PDF	Normal.
$t\bar{t}$	POWHEG-BOX	PYTHIA 6	CT10+CTEQ6L1	NLO
Single top	POWHEG-BOX	PYTHIA 6	CT10+CTEQ6L1	NLO
$t\bar{t}W$	MG5_aMC@NLO	PYTHIA 8	NNPDF2.3LO	LO
$t\bar{t}Z$	MG5_aMC@NLO	PYTHIA 8	NNPDF2.3LO	LO
$t\bar{t}H$	MG5_aMC@NLO	HERWIG++	CT10+CTEQ6L1	NLO
Z+jets	SHERPA	SHERPA	CT10	NLO
W+jets	SHERPA	SHERPA	CT10	NLO
Diboson	SHERPA	SHERPA	CT10	NLO

Table 4.1.: Monte Carlo samples and generators that are used for the event production, showering and hadronisation in the detector including the used PDF and Normalisation.

Diboson processes with one of the bosons decaying hadronically and the other leptonically are simulated using the SHERPA 2.1.1 generator. They are calculated for up to 1 (ZZ) or 0 (WW, WZ) additional partons at NLO and up to 3 additional partons at LO using the COMIX and OPENLOOPS matrix element generators and merged with the SHERPA parton shower using the ME+PS@NLO prescription. The CT10 PDF set is used in conjunction with dedicated parton shower tuning developed by the SHERPA authors. The generator cross sections are used in this case (already at NLO).[1]

All samples and generators with the used PDF and normalisation are listed in Table 4.1.

4.3. Object Definitions

This analysis is focusing on $t\bar{t}$ events with a dilepton final state. Hence, the physics objects that are used are electrons, muons and jets from the all-hadronic top and antitop decays. Leptonic tau lepton decays are also included because it is not possible to say if an electron or muon originates from a tau decay or from the Z boson directly. However, tau leptons as such are not reconstructed. In the following, it is described how muons, electrons and jets are identified in the ATLAS detector. When speaking of electrons and muons in the following includes their antiparticles, positrons and anti-muons. The only difference in terms of their reconstruction is the inverted charge.

[1]The previous three paragraphs are the official ATLAS description for MC 15 references for 13 TeV analyses CONF notes and papers for Sherpa W, Z samples, Sherpa fully leptonic diboson and semi-leptonic diboson samples.

4.3.1. Electrons

Electrons are electromagnetically charged particles that are bent by the solenoid and leave tracks in the Inner Detector (cf Section 3.2.3). They are stopped in the ECal (cf. Section 3.2.3) depositing the largest fraction of their energy. They form clusters of regions in the ECal where energy is deposited. These clusters are then matched to a track in the ID.

Additionally to the energy deposit in the ECal, electrons deposit a very small fraction of their energy in the HCal (cf. Section 3.2.4) and fractions of the electron energy may be lost while passing the inner tracker. These contributions are determined by material and calibration studies of the detector components. After matching these different components the electron four-vector is derived from the spatial coordinates and the total energy.

To prevent photon conversions or showers from hadrons to be misidentified as electrons, detailed information like the shower shape and cluster geometries are stored.

Electrons are required to be reconstructed in the central region of the detector with $|\eta| \leq 2.47$ with exception of the transition region between the barrel and the endcap of $1.37 < |\eta| < 1.52$. Electrons in the transition region are rejected because they suffer from poor reconstruction efficiency.

A likelihood (LH) approach based on shower variables is used to identify electrons. The variables contain information about bins of clusters η and bins of cluster E_T in the ECal. For these studies electrons are required to fulfil the `TightLH` identification criteria [57]. They need to be isolated according to the `gradient` working point, meaning that the track and the calorimeter isolation efficiencies $\epsilon = (0.1143 \cdot p_{\mathrm{T}}\ [\mathrm{GeV}] + 92.14)\,\%$ are functions of the electron p_{T} .

The electron longitudinal impact parameter $d_0 = z_0 \sin(\theta)$ is required to be ≤ 0.5 mm and the cut on the transverse impact parameter is set to $|d_0| / \sigma(d_0) < 5$. The matching between the track and the ECal cluster is required to satisfy $\Delta\phi < 0.02$ and $\Delta\eta = \left|\eta_{Calo}^{1stlayer} - \eta_{Track}\right| \leq 0.005$.

Additionally, the leading electron is required to have $p_{\mathrm{T}} > 25$ GeV and the second leading electron has to satisfy $p_{\mathrm{T}} > 15$ GeV.

4.3.2. Muons

The second type of leptons considered in this analysis are muons. Compared to electrons they are not stopped in the ECal and the trace they leave in the ID is not sufficient to identify them as muons and to reconstruct their momentum.

Therefore, the ATLAS detector uses the Muon System (cf. Section 3.2.5) for muon identification. Trigger information as well as tracking information from the MS are combined with tracks from the ID. In ATLAS, a muon whose tracks are reconstructed independently in the ID and the MS and then combined with a fit is referred to as `Combined Muon` (CB).

Muons are bent to a certain extent by the central solenoid but the main bending power lies in the toroidal magnets located behind the HCal and in front of the MS. Particle identification algorithms can also use information from other detector components for muon identification, like the ECal.

Muons can also be reconstructed only using the information from the MS track along with information from the interaction point. Including information about the estimated energy loss of the muon while passing the detector, the trajectory is extrapolated and the muon is labelled ME.

Muons for these studies are required to fulfil the `medium` track quality requirement [58] which uses only CB and ME tracks.

Like the electrons in these studies they need to satisfy the `gradient` isolation working point with the track and the calorimeter isolation efficiencies $\epsilon = (0.1143 \cdot p_{\mathrm{T}}\ [\mathrm{GeV}] + 92.14)\,\%$ varying with the muon p_{T}. They need to be reconstructed in the central part of the detector with $|\eta| < 2.5$ and the highest p_{T} muon needs to fulfil $p_{\mathrm{T}} \geq 20$ GeV whereas the second muon needs to pass $p_{\mathrm{T}} \geq 10$ GeV .

4.3.3. Jets

Most objects in the selected events are expected to be jets coming from hadronic interactions. Except for the top quark, quarks hadronise after emerging from a decay or particle collision. After the formation of bound states and fragmentation they form a shower of mostly soft, charged components leaving traces in the ID, the ECal and the HCal. In the HCal they deposit most of their energy and come to rest forming clusters of energy depositions.

These different contributions can be reconstructed as a jet by jet reconstruction algorithms. Jets in these studies are reconstructed using the anti-k_t algorithm [59] with a distance parameter $R = 0.4$ in the η-ϕ plane based on topological calorimeter clusters [60]. To suppress pile-up jets the Jet Vertex Tagger [61] was used which is a multivariate combination of track-based variables constructed for that purpose.

A jet candidate needs to be reconstructed in the central area of the detector with $|\eta| < 2.5$ and $p_{\mathrm{T}} > 25$ GeV .

4.3.4. Tagging of *b*-jets

Jets originating from b quarks have special characteristics making it possible to distinguish them from jets of different flavour. Especially *b*-jets from top quark decays are highly energetic because of the high rest mass of the decaying top quark. When the top quark decays it transfers that energy onto the b quark and the W boson.

After its emergence, a *b*-quark hadronises to form a *b*-hadron. The hadron moves up to a few millimetres in the detector and then decays creating a secondary vertex that can be reconstructed. Combined with the information about the impact parameter *b*-tagging algorithms can identify *b*-jets.

b-jet candidates for these studies are tagged using the MV2c20 algorithm [62] with a cut on its output > -0.4434 corresponding to an average efficiency of 77% measured in $t\bar{t}$ MC events. This is an average value because the efficiency is a function of the jet p_{T} . The MV2c20 algorithm uses a boosted decision tree to determine the jet tagging probablity.

4.3.5. Overlap Removal

During reconstruction it is possible that one and the same physics object is reconstructed twice, e.g. as an electron and a jet candidate. To define which object is used and to avoid double counting an overlap removal is applied.

Electron candidates are dropped when they share a track with a muon candidate as well as when the distance[2] in ΔR between the electron candidate and a jet candidate satisfies $0.2 < \Delta\mathrm{R} < 0.4$.

[2] $\Delta R = \sqrt{\Delta\phi^2 + \Delta\eta^2}$

In cases of one jet with $\Delta R < 0.2$ the jet candidate is removed. If more than one jet per event is below that value the one closest to the electron candidate is discarded.

As a last step it is checked whether ΔR between a muon candidate and a jet candidate is < 0.4. The muon candidate is removed as soon as the jet candidate has more than two associated tracks. Otherwise the jet is dropped.

4.4. Event Preselection

The following criteria apply to every event used for these studies.

Data Quality

Recorded data is checked for quality requirements before it can be used in analyses: ATLAS provides a so-called `good runs list` that contains the luminosity blocks that fulfil these requirements. During data taking in 2015 there were occasionally problems with the LAr and Tile calorimeters. Events affected by that are removed. Events are furthermore rejected if they are affected by missing information due to restarts of the *Timing, Trigger and Control Systems for the LHC* (TTC) or if they were affected by the recovery procedure for single event upsets in the SCT.

Vertex Selection

All events need to have a primary vertex from a hard scattering process. This vertex is selected by default from the highest $\sum p_T^2$ where a minimum of two tracks with $p_T^{track} > 400$ MeV is required [63].

Bad-Jet Cleaning

It is possible that events contain fake jets that do not originate from hard scattering processes but for example from cosmic events or noise bursts or coherent noise in the calorimeters. Events that contain at least one such jet are removed. It is applied after the overlap removal and operated with the `LooseBad` [64] selection.

Trigger

Several triggers are applied and events for these studies need to be triggered by at least one of them. ATLAS has a three-level trigger system consisting of the hardware based first level trigger (L1), the software based second level trigger (L2) and the event filter (EF). The combination of L2 and EF is called the high-level trigger (HLT). Trigger naming conventions can be found in [65] and [66] and provide information about the abbreviations that are not explained below because they go beyond the scope of this thesis.

Events for these studies need to be triggered by at least one of the following electron triggers:

- `HLT_e120_lhloose` with one electron with $p_{\mathrm{T}} > 120$ GeV passing likelihood-based *loose* identification criteria,
- `HLT_e24_lhmedium_L1EM18VH` with one electron with $p_{\mathrm{T}} > 24$ GeV passing likelihood-based *medium* identification criteria
- `HLT_e60_lhmedium` with one electron with $p_{\mathrm{T}} > 60$ GeV passing likelihood-based *medium* identification criteria,

or by one of the following single muon triggers:

- `HLT_mu20_iloose_L1MU15` with one muon with $p_{\mathrm{T}} > 20$ GeV passing the *loose* identification criteria
- `HLT_mu50` with one muon with $p_{\mathrm{T}} > 50$ GeV .

Trigger Matching

One of the triggered leptons needs to match at least one reconstructed lepton with $p_{\mathrm{T}} > 25$ GeV.

4.5. Tag Rate Function Method

Object selection and event selection and classification which is specified in Section 5.4 for this analysis impose strong requirements on events to be selected and reduce the statistics of the Monte Carlo samples significantly. By acting on one of the strongest requirements, the number of jets that are tagged as b-jets (cf. Section 4.3.4), the tag rate function method counteracts the loss of statistics.

With an assumed cross section of $\sigma_{t\bar{t}} \approx 170$ pb and $\sigma_{t\bar{t}Z} \approx 760$ fb (cf. Sections 2.3.1 and 2.4.2) the production of the signal process is suppressed and the background events are scaled with high cross section values. In combination with less events due to previous cuts, especially the b-tagging requirement, this leads to high fluctuations in the selected phase space.

Instead of rejecting events because they do not fulfil the b-jet requirement, the tag rate function method uses the tagging efficiency

$$\epsilon_i = (f_i, |\eta_i|, p_{\mathrm{T},i}) \tag{4.1}$$

to assign a probability to each event to contain a certain number of b-jets. The tagging efficiency depends on the flavour f_i of the N jets per event with $i = 1, \ldots, N$. It depends further on the absolute value of the pseudorapidity $|\eta_i|$ and the transverse momentum of the respective jet $p_{\mathrm{T},i}$.

The probability $P_{=1}$ of an event to contain one b-tagged jet can be calculated by summing over its N jets as follows:

$$P_{=1} = \sum_{i=1}^{N} \left(\epsilon_i \prod_{i \neq j} (1 - \epsilon_j) \right) \tag{4.2}$$

The probability of an event to contain at least one b-tag $P_{\geq 1}$ is given as

$$P_{\geq 1} = 1 - P_{=0}\,, \tag{4.3}$$

$$\text{with} \quad P_{=0} = \prod_{i=1}^{N} (1 - \epsilon_i)\ . \tag{4.4}$$

After having a probability of how many b-jets an event contains one needs to know which of the jets are tagged. Therefore, all permutations are taken into consideration and ideally the weight of the picked permutation is proportional to its TRF weight. Let S_i be the ith permutation, the sum of all permutation weights is calculated, so that $S_{total} = S_i + \ldots + S_N$. A random number R from a uniform distribution between 0 and S_{total} is thrown to determine which permutation is picked. One adds up weights one after the other until the value R is reached or surpassed. The permutation that was added last to the partial sum is picked to determine which of the jets are considered as tagged. Using this information is it possible to build meaningful event variables.

The value for the tagging efficiency ϵ was determined by the ATLAS flavour group and the tag rate function method was e.g. validated for [67].

5. Analysis Strategy

5.1. Introduction

This analysis is based on the 'Measurement of the associated production of a vector boson (W, Z) and top quark pair in the opposite sign dilepton channel with pp collisions at $\sqrt{s}$= 8 TeV with the ATLAS detector' [67]. For the studies described in this text the analysis strategy of [67] is applied to data recorded in the year 2015 during LHC Run II at $\sqrt{s}$= 13 TeV. Hereby, the decay of $t\bar{t}Z$ with two leptons having opposite sign and same flavour is studied.

5.2. Final State Topology

There are several possible final states in the decay of a $t\bar{t}$ pair produced in association with a Z boson that are described in this chapter. The $t\bar{t}$ pair can decay via the all-jets, lepton+jets or the dilepton channel as it is described in Section 2.3.2. Additionally, the Z boson has multiple leptonic and hadronic decay channels. They have in common that the leptons have the same flavour and the charges of the decay products add up to $Q = 0$.

Considering the whole $t\bar{t}Z$ decay, the expected number of leptons can vary from one to four leptons in the decay of $t\bar{t}Z$. Not considering tau leptons because of their ability to decay further, the expected combinations for the dileptonic $t\bar{t}Z$ case are therefore ee, $e\mu$, μe and $\mu\mu$. Assuming the all-hadronic decay of the $t\bar{t}$ pair and focusing on the leptonic decay of the Z boson, the remaining lepton final states reduce to e^-e^+ and $\mu^-\mu^+$.

Three jets are expected from the top and antitop quark decay, respectively. One of each is expected to be a b-jet. Making use of b-tagging to identify those jets gives an additional handle on the final state by requiring 2 jets being b-tagged.

A final state of a signal event is shown in Figure 5.1. The Z boson is radiated off a top quark and decays in two opposite-sign same flavour (OSSF) leptons that are highlighted in green. The $t\bar{t}$ pair decays hadronically.

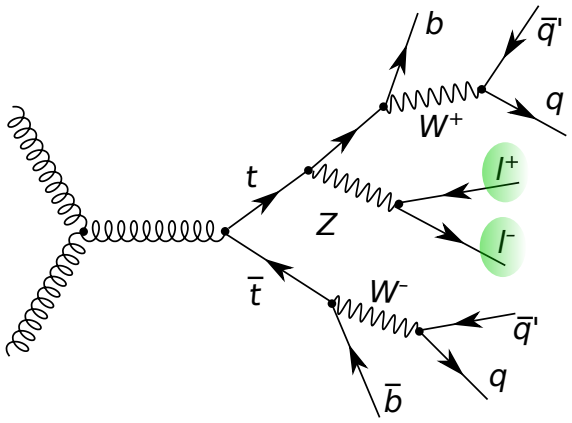

Figure 5.1.: Leading order Feynman diagrams of $t\bar{t}Z$ signal process with two OSSF leptons and six jets in the final state.

In the field of studying $t\bar{t}Z$ events, the channels with three or four leptons in the final state are usually in the focus because of a better signal to background ratio. The uncertainty on the lepton energy and the reconstruction efficiency is lower than for jets. Choosing final states with more leptons and less jets is therefore preferred.

The conclusion is that studies of the $t\bar{t}Z$ OSSF lepton channel are very challenging.

5.3. Main Backgrounds

The highest contribution of events mimicking the signature of signal events are coming from Z+jets and $t\bar{t}$ production. The left Feynman diagram in Figure 5.2 shows a Z+jets event with a leptonically decaying Z boson which was produced by quark-antiquark annihilation. In this example, initial state gluon radiation from the anti-quark showers and creates more gluons and possibly quarks, that are measured as jets in the detector and can fake a signal event.

The right Feynman diagram in Figure 5.2 shows a $t\bar{t}$ event after gluon-gluon fusion which decays via the dilepton channel. These leptons have opposite sign and can, but not necessarily need to have same flavour. From the decays of the W bosons the final state has two b-jets. Additional jets can occur from initial and/or final state radiation so that $t\bar{t}$ production is the second highest background contribution to the signal.

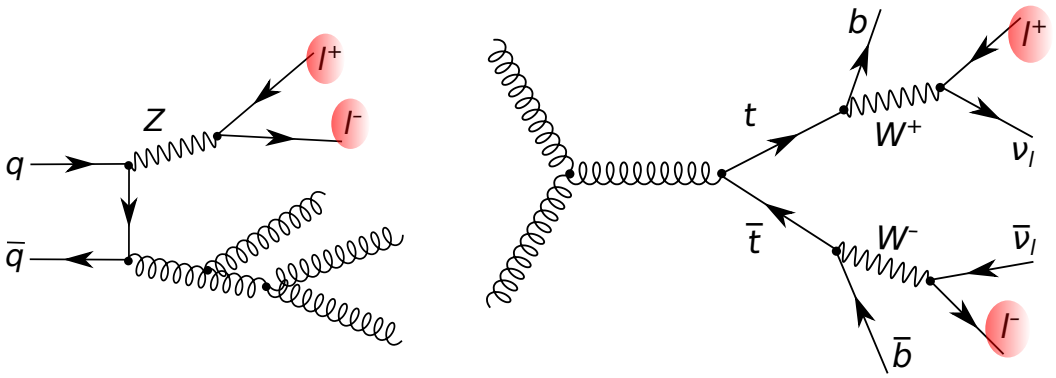

Figure 5.2.: The two main background processes are Z+jets production with a leptonic decay of the Z boson (left side) and $t\bar{t}$ production with a dileptonic decay of the $t\bar{t}$ pair. In the former case, QCD processes initiated by gluons and subsequent quarks can lead to different jet multiplicities so that the signal process can be mimicked. QCD initial and/or final state radiation can also lead to additional jets in the case of $t\bar{t}$.

5.4. Event Selection and Classification

After the preselection described in Section 4.4 further selection criteria are applied. At first, events with either two electrons or two muons of opposite sign are selected to only allow lepton combinations of e^-e^+ and $\mu^-\mu^+$. The leptons are sorted according to their p_T value. The first lepton needs to pass a $p_\mathrm{T}^\mathrm{lep} > 25\,\mathrm{GeV}$ cut and the second lepton needs to fulfil $p_\mathrm{T}^\mathrm{lep} > 15\,\mathrm{GeV}$.

The invariant mass of the two selected leptons needs to be $m_{ll} > 15\,\mathrm{GeV}$ and within the so-called Z-window $|m_{ll} - m_Z| < 10\,\mathrm{GeV}$.

As for the jets, events need to contain at least 4 jets with $p_\mathrm{T}^\mathrm{jet} > 25$ GeV and two of the jets need to be tagged as b-jets. Due to mis-modelling of the heavy-flavour (HF) content in the Z+jets MC sample, events are re-weighted to match the HF jet composition in data. Jets from charm or bottom quarks are considered as heavy-flavour jets. The number of such jets per event is counted and events with exactly one HF jet (Z+jets 1HF) are multiplied by 1.1 whereas events with at least 2 HF (Z+jets ge2HF) jets are scaled up with 1.43. This re-weighting is applied with regard to events without HF jets (Z+jets noHF).

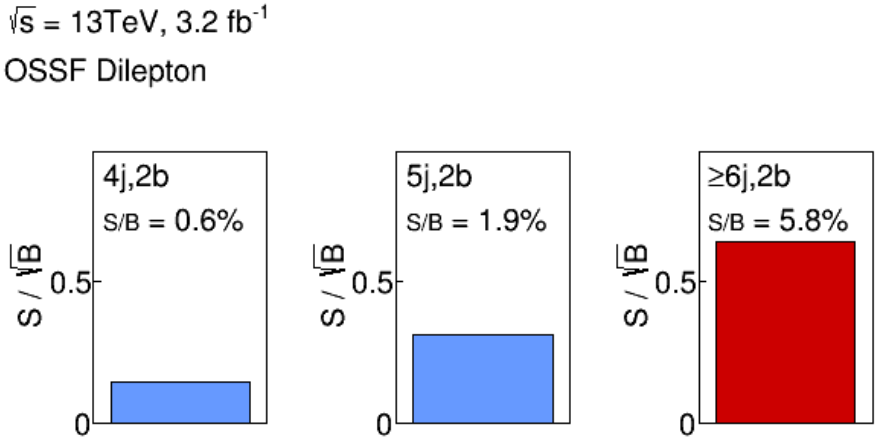

Figure 5.3.: Different categories to divide events according to their jet multiplicity and the number of jets being tagged as b-jets. The right category, with ≥ 6 jets is defined to be the signal region. The others are control regions.

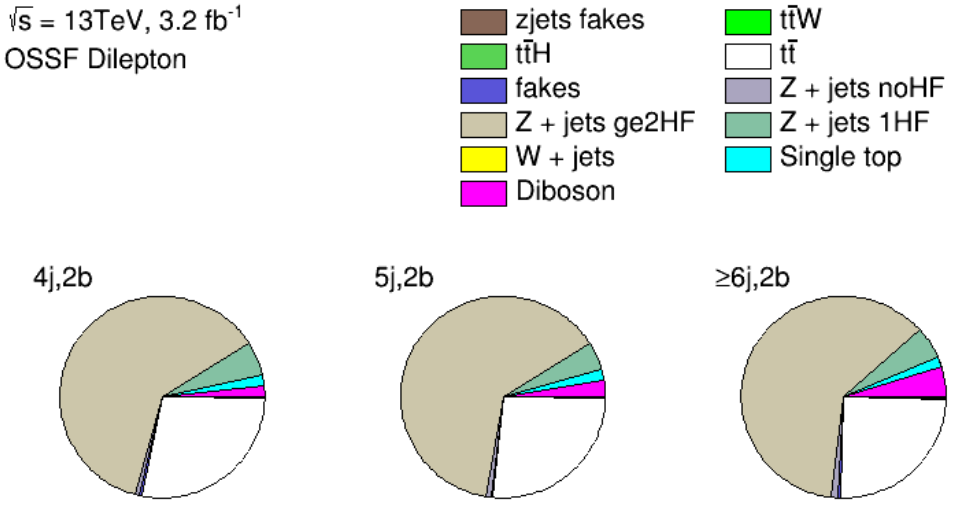

Figure 5.4.: Different categories to divide events according to jet multiplicity and number of jets tagged as b-jets. The right category, with ≥ 6 jets is defined to be the signal regions. The others are control regions.

After the object selection, the event preselection and the event selection, events are classified in control regions (CR) and signal regions (SR). Two CR regions and one SR are defined by varying the number of jets (n_{jets}) per event. Starting from 4 jets and 2 b-jets (4j, 2b) and 5 jets, 2 b-jets (5j, 2b) as CR regions, events for the signal region are required to have the highest jet multiplicity: at least 6 jets and 2 b-jets ($\geq$ 6j, 2b).

Figure 5.3 shows the signal over background S/B and the $S/\sqrt{B}$ plots for the regions defined above. One can see that this ratio increases along with the jet multiplicity.

The $S/\sqrt{B}$ ratio describes the 'discovery potential', how much signal is expected to be seen. Also the ratio S/B is important to be maximised. The higher this ratio the higher the achievable precision of the measurement. Hence it is important to optimise these values before proceeding to the next step of the analysis which is described in the following section.

Figure 5.4 gives an overview of the different background contributions for each of the three regions. One can see that Z+jets events with $\geq$ 2 HF jets are dominating by representing approximately $2/3$ of all events. The second highest contribution comes from $t\bar{t}$ events with roughly $1/4$ of all background events.

5.5. Multivariate Analysis

5.5.1. The Concept of Multivariate Analyses

From previous analyses of the opposite sign dilepton channel it is known that the discrimination between signal and background events is difficult. Therefore this analysis will exploit the potential of multivariate analysis (MVA) techniques.

In contrast to 'cut and count' analyses, an MVA combines the input of multiple variables to form a discriminant to separate signal and background events.

The misclassification rate in a cut and count analysis is higher because the phase space is linearly separated in different regions like it is shown in Figure 5.5. In the schematics (a) and (b), the phase space of the variables x_1 and x_2 is split up by defining a cut on both variables to distinguish between the data sample H_0 and H_1. The separation becomes better by choosing a non-linear approach in schematic (c).

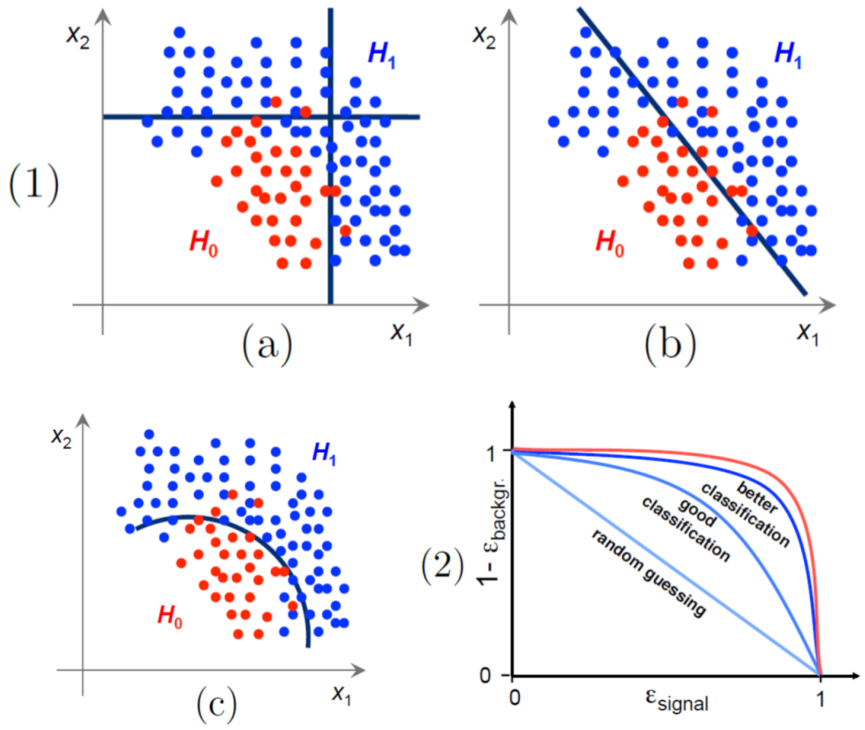

Figure 5.5.: Schematic showing different approaches (1a), (1b) and (1c) to classify signal (H_1) and background (H_0) events in a two-dimensional parameter space. Schematic (2) illustrates the ROC curve (Receiver Operating Characteristic) describing the discrimination power of the used MVA.

An MVA tries to find the best discrimination in a multidimensional phase space by creating a function $f(x_1, x_2, \ldots, x_n)$ with event variables $x_1, x_2, \ldots, x_n$ that cover the phase space such that the discrimination power is high.

The Receiver Operating Characteristic (ROC) curve indicates the goodness of the classification as shown on the outer right side of Figure 5.5.
On the y-axis, $1 - \epsilon_{\text{backgr.}}$ is shown, with the background efficiency $\epsilon_{\text{backgr.}}$, plotted against the signal efficiency ϵ_{signal}. Both values should be close to one for a good classification meaning that the best discrimination is achieved by the dark blue and red curves.

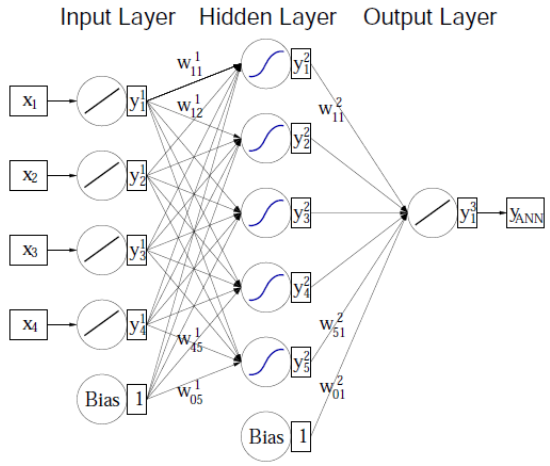

Figure 5.6: Schematic of an artificial neural network. It consists of nodes that are arranged in layers. Event variables are the input. During the training, events are passed through this structure and the network 'learns' to classify the input by finding the best weights for the connections between the nodes.

5.5.2. Artificial Neural Networks

One example for an MVA is the artificial neural network (ANN). The ANN consists of so called nodes which read the values of the event variables. In Figure 5.6, neurons are represented by circles that are connected with each other leading to the analogy of neurons in a brain.

Neurons have an associated activation function 'turning' them 'on' for certain combinations of input variable's values. The symbol in the neuron circle indicates what kind of activation function is used. Possible are linear and non-linear functions like the sigmoid function, the hyperbolic tangent or a radial function. The input-variables set the network in a defined state which then can be measured from the response of the output neurons.

A neuron response function maps the neuron input to the neuron output. Each connection between neurons has an associated weight which is multiplied with the neuron output. After that it becomes the input for the next neuron.

The analysis will use a so-called feed-forward network implemented in the NEUROBAYES package [68]. NEUROBAYES uses a three-layer feed-forward network and each event is passed through the network layer by layer.

ANNs are able to 'learn from experience'. This process is called training and the used training method is called 'back propagation'. Therefore the network needs to know the desired output for every training event. After passing the event through the network the output value is compared to the desired value and classifies the event. Ideally this value is 1 for signal and 0 for background events. The classifier (or discriminant) therefore combines the neuron response functions, the weights associated to the neuron connections and the input-variables.

After the ANN is set up, the discrimination of signal and background events needs to be optimised by choosing the best combination of input-variables with a high discrimination power.

5.6. Neural Network Implementation

5.6.1. The NEUROBAYES Package

NEUROBAYES [68] is a commercial software package to train a three-layer feed-forward neural network. For these studies, this software package is used to train a neural network (NN) to learn the characteristics of a $t\bar{t}Z$ signal event and distinguish it from a background event. The output is a classifier that can be used in data analysis. This section gives a general overview of the functionalities of NEUROBAYES whereas the chosen setup for these studies is described in Section 6.6.

NEUROBAYES consists of a kernel that provides all functions that are necessary for the training and the analysis and an interface part enabling the user to feed information into the network. The training part is performed by the so-called NEUROBAYES-Teacher and the analysis part for unknown events is called the NEUROBAYES-Expert. For these studies only the NEUROBAYES-Teacher is used.

The input to the (NN) are Monte Carlo samples for $t\bar{t}Z$ and the main background Z+jets that are described in Section 4.2. Furthermore, the variables the NN should use for the training need to be specified.

Preprocessing of Input-Variables

Before the training process of the NN the input-variables need to be modified such that the NN can handle them. Usually their distributions differ, the normalisation is different and some of the variables may be correlated. Hence, the user needs to specify the way NEUROBAYES is preprocessing the input before the training.

A global preprocessing is applied to all the variables and there is the option to apply individual preprocessing for each of the variables before the global preprocessing. This is useful e.g. when discrete variables like 'the number of jets per event n_{jet}' and continuous variables like 'the transverse momentum of a lepton pair p_{T}^{ll}' are used in an NN at the same time.

Ranking of Input-Variables

NEUROBAYES ranks the variables according to their significance. Therefore the correlation of the variables to the target is calculated, meaning the correlation to the input-variables of the signal sample. NEUROBAYES calculates the correlation matrix of the input-variables. In a second step it removes one variable and calculates the matrix again. The loss of correlation between the first and the second matrix is stored. This procedure is performed for every input variable and the variable that causes the least loss of correlation is discarded. This is done until the variables with the highest significance, meaning the highest information loss after its removing remains. Based on that information NEUROBAYES ranks the input-variables. The least correlated variable to the target adds the least significance and is ranked last. This ranking indicated the importance of variables for the training and can be used to optimise the number of variables to use as an input.

The Training Process

In neural networks the output of node j in layer n can be described by

$$h_j^n = g\left(\sum_k^{\text{variables}} w_{jk}^n \cdot x_k^{n-1} + \mu_j^n\right) \tag{5.1}$$

with $g(x) = 1/\left(1+e^{-x}\right)$ being a sigmoid function in this case. For other applications a different function can be better suitable. It is the weighted sum of all nodes in layer $n-1$ with the weights w_{jk}^n between the nodes of the layers for the variables k and the threshold μ_j^n that allows to adjust the working point of the node.

By using the term *training* one means to minimise a loss function, e.g. the cross-entropy

$$L\left(\mathbf{w}\right) = \sum_i^{\text{events}} \left[y^{(i)} \ln\left(y\left(\mathbf{x}^{(i)}, \mathbf{w}\right)\right) + \left(1-y^{(i)}\right) \ln\left(1-y\left(\mathbf{x}^{(i)}, \mathbf{w}\right)\right)\right] \quad , \tag{5.2}$$

where $y^{(i)} \in \{1,0\}$ is the event classification, $y^{(i)} = 1$: signal; $y^{(i)} = 0$: background. $y\left(\mathbf{x}^{(i)}, \mathbf{w}\right)$ is the output of the neural network for event i with the vectors for the variables $\mathbf{x}^{(i)}$ and weights $\mathbf{w}$. The index j of Equation 5.1 has been absorbed in the vector notation in Equation 5.2.

By adjusting the weights the difference between the output discriminant of the NN and the desired output which you train the network against, is minimised.

5.6.2. The FricoNN Framework

The NEUROBAYES package needs to be steered by an interface. For these studies the FricoNN framework is used to interface with the different subroutines and initialise NEUROBAYES.

As a first step, the network task, here 'classification', and the initial network topology needs to be defined. Therefore, the input-variables are read in and the parameters for the preprocessing process are defined (cf. Section 5.6.1). The architecture may be adjusted during the training of the network (for details see Sections 5.6.1 and 6.6).

Secondly, the training samples are read in and the signal sample, the target, is defined, weights are adjusted and the training is performed.

Later on, FricoNN can also be used for cross checks regarding the quality of the output network, e.g. whether it is overtrained and reproduces the input samples or if it learned the general characteristics of the training sample and can be used for classifying unknown data.

FricoNN is also able to perform the analysis of such unknown data using the final discriminant of the network that was formerly trained.

6. Analysis/Studies and Results

6.1. Kinematic Control Distributions

To prove whether the MC generated samples model the data samples well, control plots are necessary. As it is described in Section 5.4, the difference between the analysis regions is defined by the jet multiplicity. The b-tag multiplicity is two for all of them. For better comparison with other analyses in this field, it is still carried in the labels throughout the following chapters.

Figure 6.1 shows the angular distributions in ϕ for electrons and the p_{T} distributions of muons. For most of the bins the simulation models the data well within the statistical uncertainties. For getting a better understanding of the Z+jets background, the sample was split according to the heavy-flavour jet content like it was described in Section 5.4. To avoid even higher statistical fluctuations, the Z+jets sample is using the tag rate function method described in Section 4.5.

Despite of that, the MC statistics is still low in the signal region. The background is dominated by Z+jets events due to the Z-window cut. Additionally, the contribution from $t\bar{t}$ events is visible. The other background processes play a minor role for modelling the data distributions.

Table 6.1 shows the yields for the different MC samples and compares them with data. The (4j, 2b) CR shows good agreement within the statistical uncertainty. For the other regions the deviation of MC yields from what is expected from data is significant. This is also visible in the high-content MC bins for these regions in Figures 6.1 and 6.2.

6.2. Discriminating Variables

The discrimination of signal and background events is achieved on the basis of variables whose distributions differ for the two categories. Generally one distinguishes four types of variables:

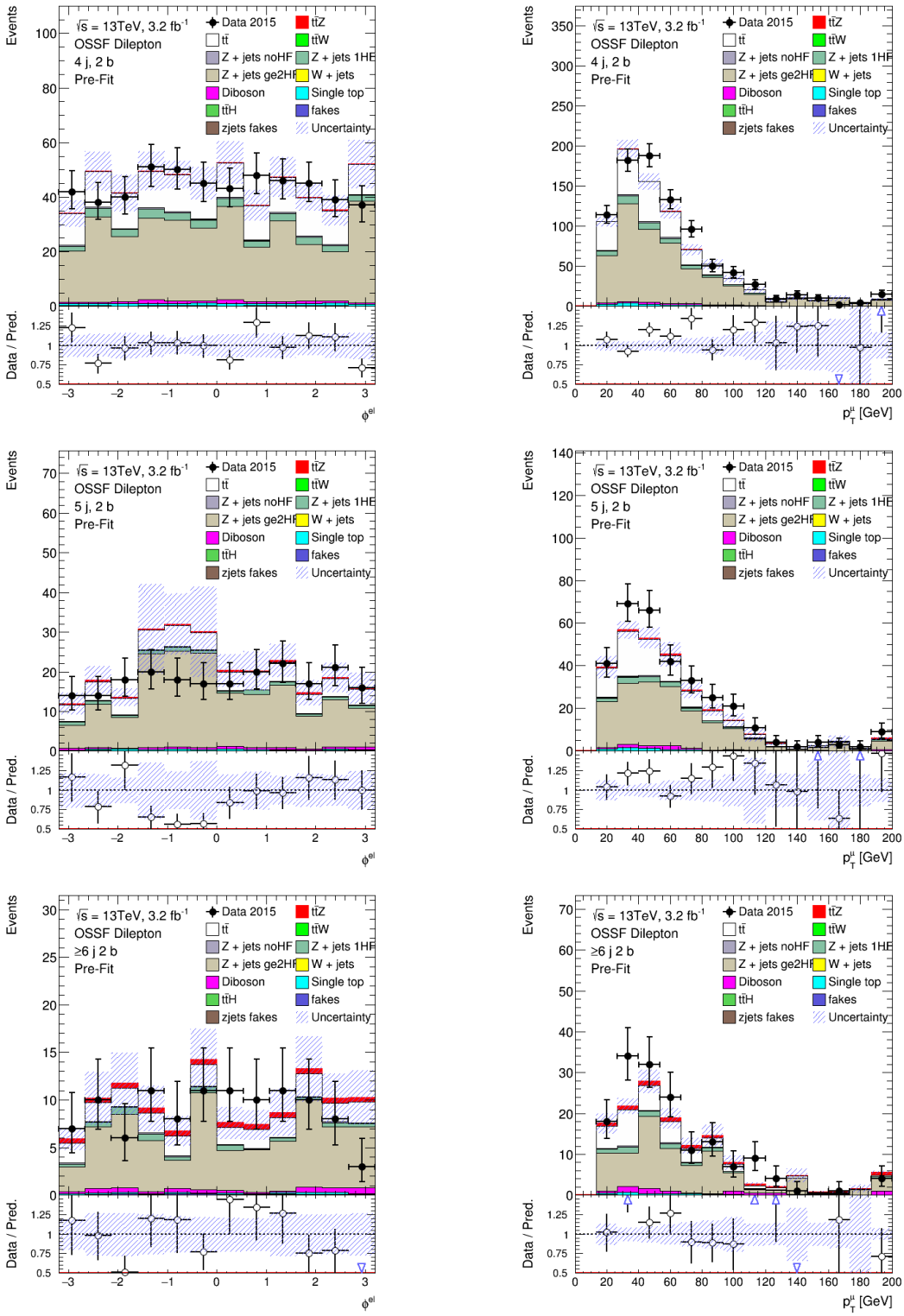

Figure 6.1.: Angular distribution of the electron ϕ^{el} (left) and the transverse momentum of the muon p_{T}^{μ} (right) for the control regions (4j, 2b), (5j, 2b) and the signal region ($\geq$6j, 2b) from top to bottom. Together with the distributions in Figure 6.2, the variables are representative for the whole set of control distributions. The whole set of control plots is found in Appendix A.

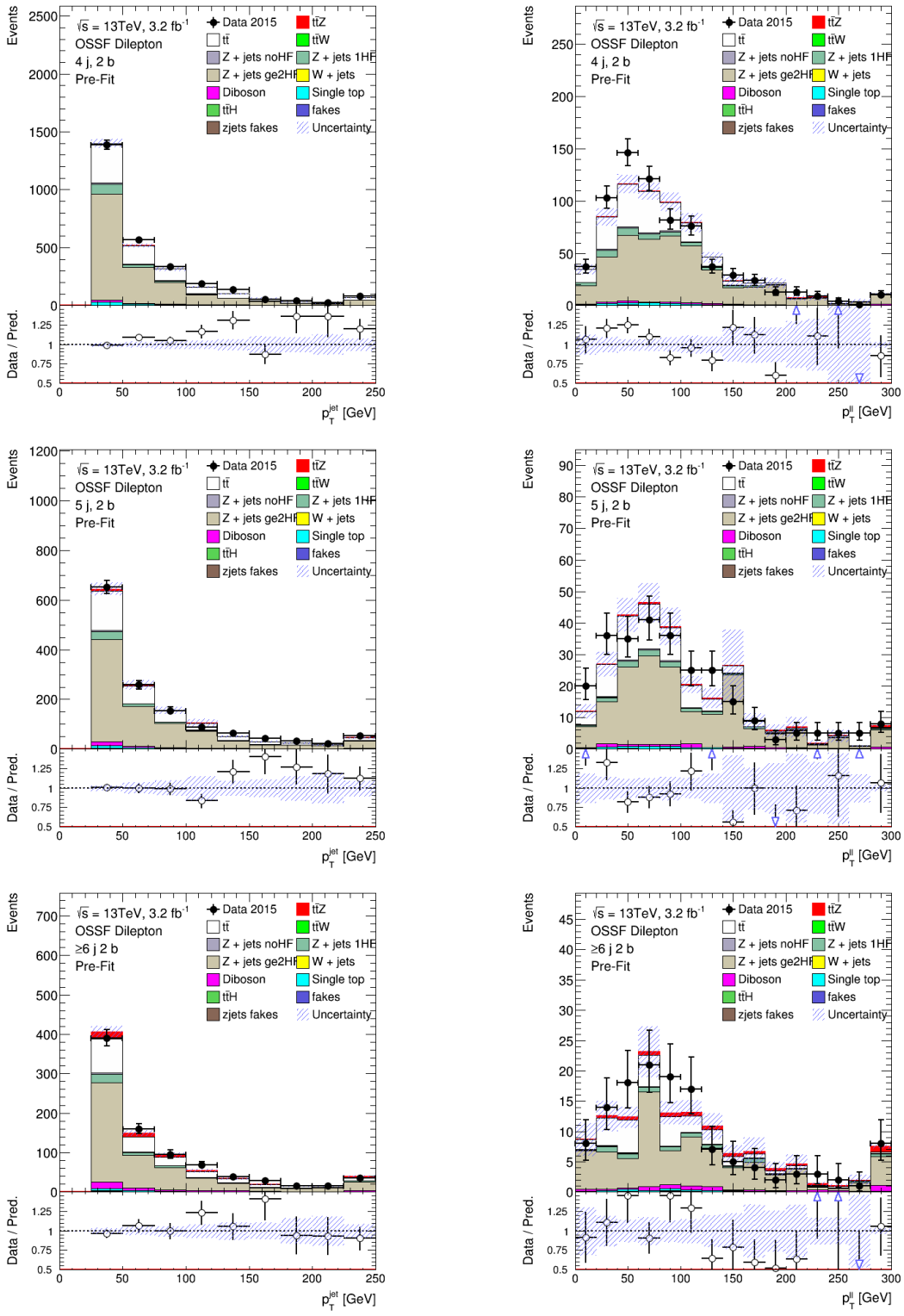

Figure 6.2.: Transvers momentum of all jets $p_{\mathrm{T}}^{\mathrm{jet}}$ (left) and the transverse momentum of the lepton pair $p_{\mathrm{T}}^{\mathrm{ll}}$ for the control regions (4j, 2b), (5j, 2b) and the signal region ($\geq$6j, 2b) from top to bottom. Together with the distributions in Figure 6.1, the variables are representative for the whole set of control distributions. The whole set of control plots is found in Appendix A.

	4 j, 2 b (CR)	**5 j, 2 b (SR)**	**≥6 j, 2 b (SR)**
$t\bar{t}Z$ (signal)	3.80 ± 0.03	5.11 ± 0.04	7.04 ± 0.04
$t\bar{t}$	187.82 ± 1.85	69.22 ± 1.12	30.16 ± 0.74
$t\bar{t}W$	0.44 ± 0.01	0.28 ± 0.01	0.18 ± 0.01
Z+jets noHF	5.79 ± 0.14	2.18 ± 0.10	1.21 ± 0.08
Z+jets 1HF	36.84 ± 1.44	11.80 ± 0.75	6.26 ± 0.62
Z+jets ge2HF	411.81 ± 22.50	166.71 ± 17.11	74.30 ± 7.63
W+jets	0 ± 0	0 ± 0	0 ± 0
Diboson	11.31 ± 1.15	6.86 ± 0.88	5.88 ± 0.67
Single top	12.47 ± 0.47	4.91 ± 0.28	2.01 ± 0.16
$t\bar{t}H$	0.30 ± 0.04	0.27 ± 0.06	0.28 ± 0.07
Fakes total	2.12 ± 0.33	0.77 ± 0.17	0.62 ± 0.18
Z+jets fakes	$4.79 \times 10^{-5} \pm 4.49 \times 10^{-5}$	$5 \times 10^{-6} \pm 0.22$	0.10 ± 0.02
Bkg. total	672.71 ± 22.66	268.11 ± 17.19	128.03 ± 7.72
Data	705	273	132

Table 6.1.: Yields of the contributing background processes for the control and signal regions in comparison to data.

Object Kinematics

Kinematics includes information of motion in space. Particles are characterised by their four-vector and the information for the vector components can be calculated from measurable variables, like for example the pseudorapidity η, the angle ϕ and the transverse momentum p_{T} as well as the energy.

Object Pair Properties

Often it is useful to group information of different particles. Motivations are a characteristic distribution in space or that they evolved from the decay of the same mother particle. Examples are the transverse momentum of two leptons p_T^{ll}, the difference[1] ΔR of two b-jets with the maximum mass $\Delta R_{bb}^{\mathrm{max}\ m}$ or the mass of two jets with the maximal transverse energy $m_{jj}^{\mathrm{max}\ p_{\mathrm{T}}}$. Figure 6.3 illustrates ΔR between two leptons.

[1] $R = \sqrt{\phi^2 + \eta^2}$

Global Event Variables

Variables that give information about the event as a whole are important because they are sensitive to the collision energy which is a key parameter of particle colliders. One example is the sum of transverse momentum of all objects of the event H_{T}. Another variable is the number of jets above a certain threshold of transverse momentum N_{jet}^{40}, e.g. with a cut on $p_{\mathrm{T}} > 40$ GeV. Making use of momentum conservation in the transverse plane, allows to gain knowledge of neutrinos in an event by calculating the missing transverse momentum to deduce the missing transverse energy $E_{\mathrm{T}}^{\mathrm{miss}}$, even though neutrinos cannot be tracked and do not deposit energy in the calorimeters.

Event Shape Variables

Event shape variables take the information of all objects in an event into account to profit from the combined information of space and motion. One example is *Centrality* which is the sum of transverse momentum of all particles of an event divided by the total energy.

Figure 6.3 shows a schematic of *Centrality*. The blue arrows represent particles from a central event where the trajectories are perpendicular to the beam axis. This would lead to *Centrality* $= 1$. The black arrows labelled *Boosted* represent objects of an event with a small opening angle with respect to the beam axis. The p_{T} of these particles is illustrated by the red arrows. By dividing their sum by the total energy, *Centrality* becomes much smaller than for the more central event and a discrimination between the two is possible.

6.3. Separation between $t\bar{t}Z$ and Z+jets Events

The final state topology of $t\bar{t}Z$ signal events and Z+jets background events differ and the respective characteristics are mirrored in the variables that are introduced in this section. The Feynman diagrams of the two processes are shown in Figures 5.1 and 5.2.

A general difference between the two processes is the collision energy that is necessary to produce such an event. For $t\bar{t}Z$, the energy threshold is much higher because of the high mass of the $t\bar{t}$ pair. Variables containing information about transverse momentum or mass exploit that property.

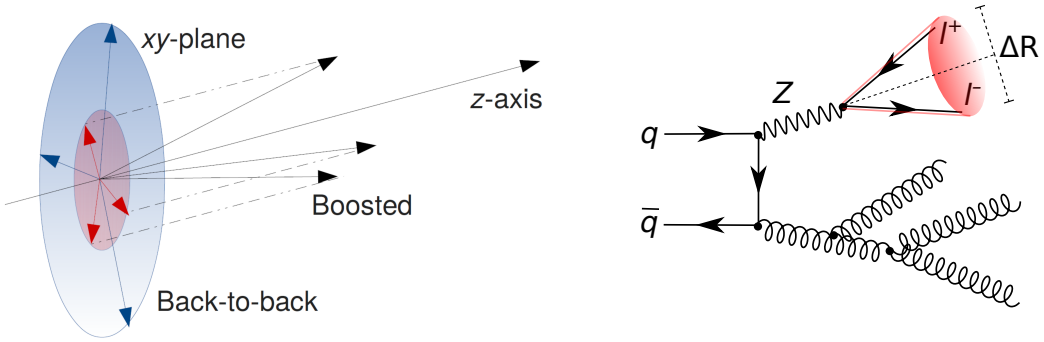

Figure 6.3.: Schematic of *Centrality* (left) as an example of an event shape variable and ΔR between two leptons as an object pair property. *Centrality* is the sum of p_{T} of all objects in an event divided by the total energy. ΔR (right) is the distance between two objects in the η-ϕ plane.

A second generic difference is that jets in Z+jets events are mainly produced by gluon radiation from the initial (ISR) state radiation. Since QCD is infrared divergent in the low energy regime the opening angle between the jets is expected to mainly be small so that the final state objects rather hit the detector in high $|\eta|$ regions than being central. Hence, variables including spatial information like $\Delta\eta$ are also used to discriminate $t\bar{t}Z$ from Z+jets events.

Figure 6.4 shows the distributions for the variables discussed in this section from top to bottom and from left to right:

1. $m_{jj}^{\text{max } p_{\mathrm{T}}}$ is the mass of the two jets with the maximum transverse momentum in an event. The jets can be of any flavour and no tagging information is considered. Despite the higher production threshold of $t\bar{t}Z$, the jet pair has higher p_{T} values for Z+jets events. This is because the hadronically decaying W bosons in $t\bar{t}Z$ events are mostly responsible for the jet pair with the highest p_{T}. Consequently the first two bins in the red signal distribution are where more than 50% of the events accumulate and the distribution then drops.

2. $m_{bb}^{p_{\mathrm{T}}\ \text{ord}}$ is the mass of the pair of b-jets that is calculated after all b-jets in the event are sorted according to their transverse momentum and the two highest jets are picked. The signal distribution is shifted to the right because b-jets in $t\bar{t}Z$ events originate preferably from the decay of the top and the antitop quark and are expected to be higher energetic than b-jets from Z+jets events. This is a consequence of the higher production threshold for signal events and results in a higher invariant mass of the b-jet pair.

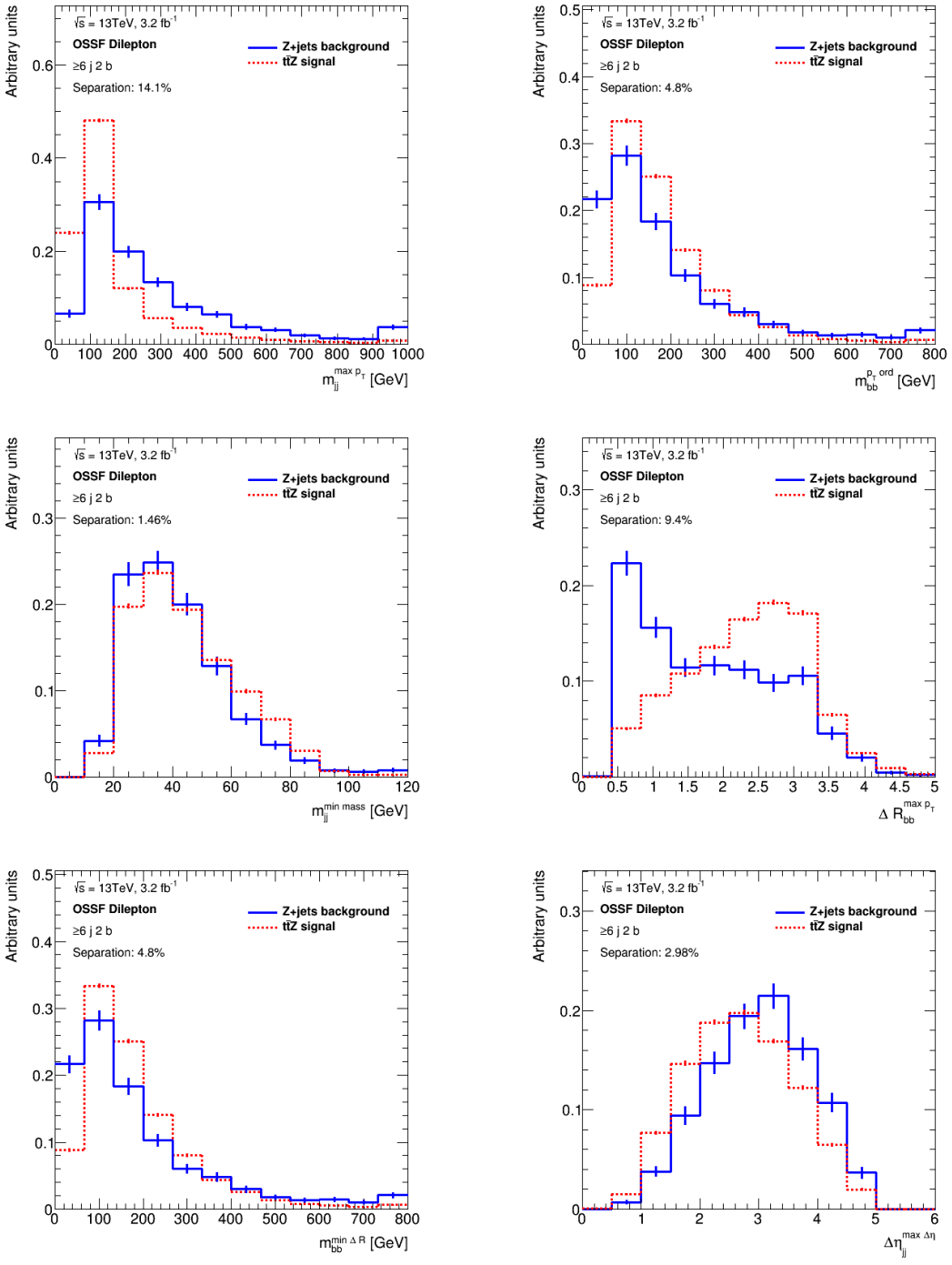

Figure 6.4.: Separation of variables for the discrimination of $t\bar{t}Z$ signal events from Z+jets background events for the signal region (≥6j, 2b).

3. $m_{jj}^{\text{min mass}}$ is the mass of the pair of jets having the minimum mass in an event. This variable shows less separation power than the others but still the background distribution is shifted to the lower mass regime because of background events having a lower production energy.

4. $\Delta R_{bb}^{\text{max } p_T}$ is the difference in ΔR between the two b-jets with the highest transverse momentum. The background distribution peaks for very low values because those b-jet pairs are expected to arise from $g \to bb$ which is a process with a small opening angle. On the contrary, the two b-jets in $t\bar{t}Z$ events are expected to stem from different mother particles, the top and the antitop quark, and this process is rather oriented back-to-back leading to higher values of ΔR peaking at 2.5.

5. $m_{bb}^{\text{min } \Delta R}$ is the mass of the b-jet pair with minimum ΔR. The b-jet pair in background events is expected to originate mostly from $g \to b\bar{b}$ and background events have a lower production energy threshold. Hence the distribution shows many entries in low-energy bins. For signal events the hadronic decay of the $t \to Wb \to q\bar{b}b$ is visible in the peak around 100 GeV.

6. $\Delta\eta_{jj}^{\text{max } \Delta\eta}$ is the difference in η between the pair of jets with the largest $\Delta\eta$ in an event. This variable exploits that Z+jets events are oriented closer to the beam axis. Hence the background distribution is shifted to higher values of $\Delta\eta$ because it is likely to have a jet pair with jets being very forward and backwards oriented, respectively.

6.4. Separation between $t\bar{t}Z$ and $t\bar{t}$ Events

The two main backgrounds for $t\bar{t}Z$ signal events are Z+jets and $t\bar{t}$ events. The final state topology of these two backgrounds show different characteristics with respect to the signal process but also with respect to each other. Therefore the discriminating variables to separate the signal from $t\bar{t}$ background events are required to be identified in this section. It is not possible to achieve a reasonable separation using the variables introduced for discriminating the Z+jets background from the $t\bar{t}Z$ signal process.

As for Z+jets, the production threshold for $t\bar{t}$ events is lower then for $t\bar{t}Z$ events, though it is higher than for Z+jets. Another difference lays in the properties of the lepton pair since the leptons from $t\bar{t}$ events do not arise from the same mother particle as it is the case for $t\bar{t}Z$.

Figures 6.5 and 6.6 show the variables that exploit these differences to separate $t\bar{t}Z$ signal events from $t\bar{t}$ background events. They are introduced from top to bottom and left to right:

1. $\boldsymbol{p_{\mathrm{T}}^{ll}}$ is the transverse momentum of the lepton pair in an event. The background distribution is shifted to the lower energy regime showing that the lepton pair mostly does not stem from a Z boson. The lepton pair is expected to originate from the dileptonic $t\bar{t}$ decay

2. $\boldsymbol{m_{ll}}$ is the transverse mass of the lepton pair in an event. Because of the Z-window cut on this variable bins with $|m_Z - m_{ll}| > 10$ GeV are not populated. The background distribution is flat within the Z-window because the energy of the lepton pair in background events is expected to be uniformly distributed because they originate from different mother particles. The bin around 100 GeV of the blue histogram is a bit less populated than the others because the Z-window has its upper boundary at 101 GeV within the bin. On the contrary, a clear peak at the Z boson mass is visible for $t\bar{t}Z$ events.

3. $\boldsymbol{\Delta R_{ll}}$ is the difference in ΔR of the lepton pair. The leptons from $t\bar{t}Z$ events are expected to be much closer together than leptons from $t\bar{t}$ event. This is visible by the signal distribution being shifted to the low ΔR values.

4. $\mathbf{max}\ \boldsymbol{m_{lb}^{\mathrm{min}\ \Delta R}}$ calculates the invariant mass of each of the two leptons with its closest jet, respectively. The higher value of the two is considered. This variable distinguishes the leptonically decaying top and antitop quarks in $t\bar{t}$ events from the hadronically decaying $t\bar{t}$ pairs in $t\bar{t}Z$ events. For $t\bar{t}$ events, by pairing leptons and b-jets with the minimum ΔR they are associated to the top or antitop quark they originate from. Compared to lb pairs from $t\bar{t}Z$ events the pair with higher invariant mass is expected to be smaller for $t\bar{t}$, what is seen in the distributions.

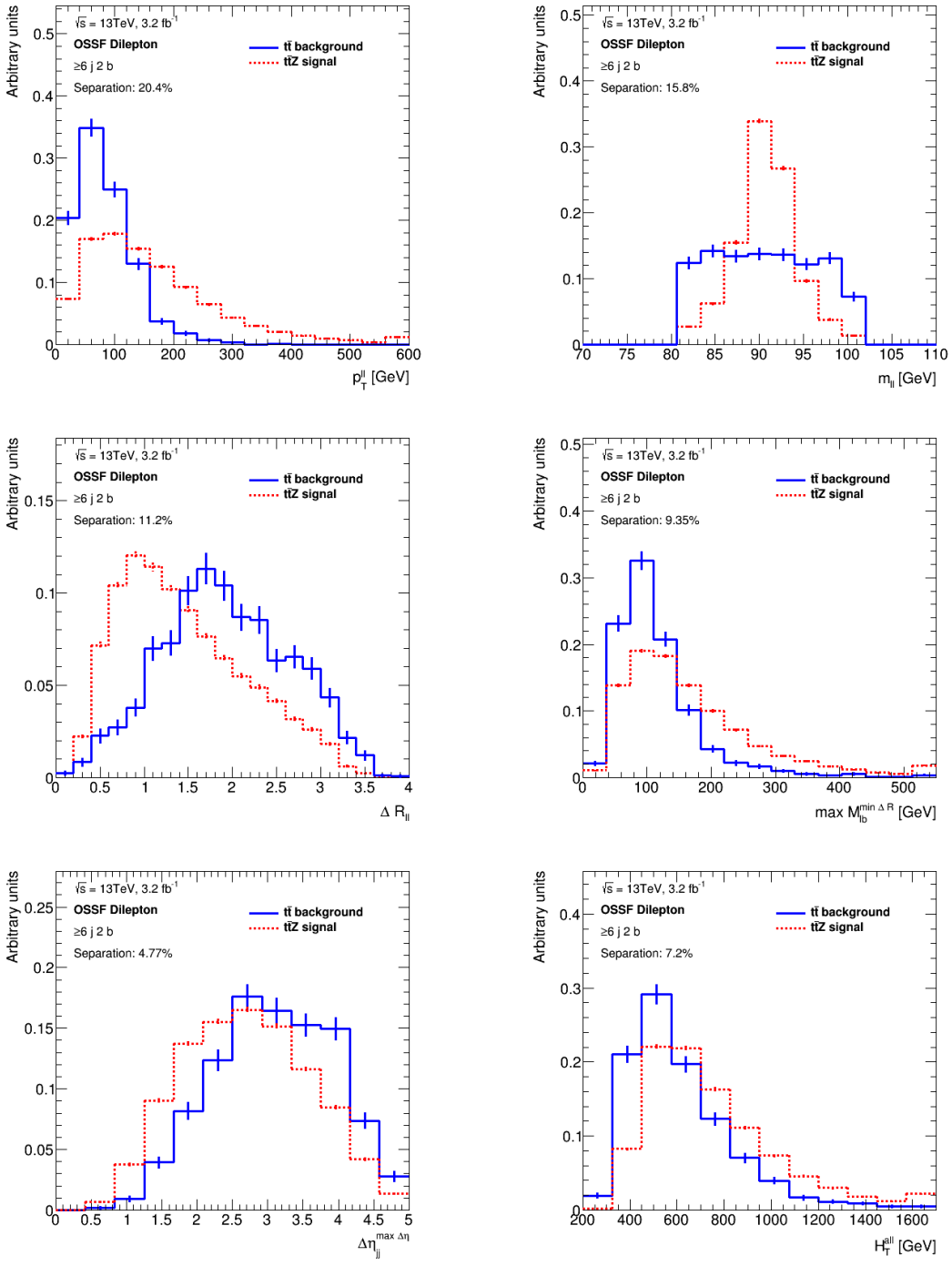

Figure 6.5.: Separation of variables for the discrimination of $t\bar{t}Z$ signal events from $t\bar{t}$ background events for the signal region ($\geq$6j, 2b).

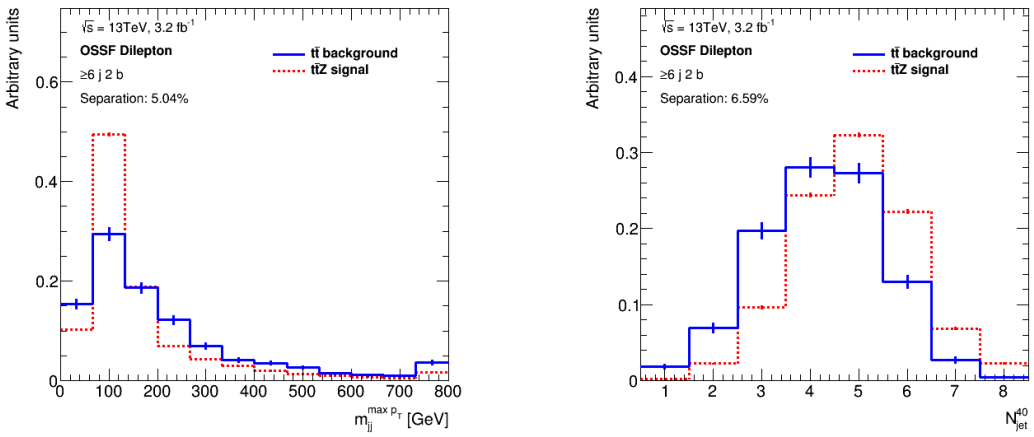

Figure 6.6.: Separation of variables for the discrimination of $t\bar{t}Z$ signal events from $t\bar{t}$ background events for the signal region ($\geq$6j, 2b).

5. $\boldsymbol{\Delta\eta_{jj}^{\max\,\Delta\eta}}$ is the difference in η between the jet pair with maximum $\Delta\eta$. Also this variable distinguishes hadronically from leptonically decaying top/antitop quarks. In $t\bar{t}Z$ events three jets respectively originate from one and the same top/antitop quark. Therefore these three each are expected to be closer together because of the boost in the same direction. Having two groups of three jets with opposite orientation, the maximum possible $\Delta\eta$ between two jets out of all six jets is larger than in $t\bar{t}$ events. In dileptonic $t\bar{t}$ decays only the b-jets arise from top/antitop quarks. The other jets originate from QCD radiation and therefore the jets are expected to be further apart as for signal events. The distributions confirm this expectation.

6. $\boldsymbol{H_{\mathrm{T}}^{\mathrm{all}}}$ is the sum of transverse momenta of all physics objects in an event. Because of the higher production threshold for $t\bar{t}Z$ events the signal distribution is shifted to higher $H_{\mathrm{T}}^{\mathrm{all}}$ values with respect to background events.

7. $m_{jj}^{\text{max } p_T}$ is the invariant mass of the lepton pair with the maximum transverse momentum in an event. This variable isolates the characteristics of a hadronically decaying W bosons in $t\bar{t}Z$ events. The signal distribution shows a clear peak in the bin of the W boson mass of $\approx$ 80 GeV. In cases when only one jet from the W decay carries the main energy fraction this jet can also pair with the b-jet of the respective top/antitop quark. Also the background distribution peaks in the same bin around 100 GeV but the distribution then falls rather moderately compared to the sharp decline of the signal distribution. The jet pairs from $t\bar{t}$ events are preferably the two b-jets from the top/antitop decay which are completely independent in the sense that they originate from different mother particles. This explains the shape difference.

8. N_{jet}^{40} is the number of jets per event with a transverse momentum larger than 40 GeV. This variable again exploits the higher production threshold of $t\bar{t}Z$ events so that the objects in general are of higher transverse momentum. The signal distribution is shifted to the higher jet numbers.

6.5. Statistics Limitations in Z+jets MC Sample

In preparation for training a neural network with the variables defined in Sections 6.3 and 6.4 as an input, studies of the properties of the Z+jets MC sample are conducted. Two properties of the sample are identified that affect the separation ability of the neural network in a negative way. These properties have their origin in how the MC sample was produced. Other than the MC samples for the other processes, the Z+jets sample is produced in p_T-slices. Each of the slices is assigned a data set ID (DSID). Appendix B gives an overview of the different Z+jets sample slices.

This section discusses the issues and describes the measures that are taken to make a separation of signal and background events possible using a neural network.

6.5.1. Mis-Modelling of Discriminating Variables

As described in Section 6.1 the tag rate function method was used in the Z+jets MC sample to enhance statistics. Instead of cutting on the number of b-jets a probability is calculated for each event to contain a certain number of b-jets (cf. Section 4.5).

In Sections 6.3 and 6.4 it is described how important b-tagging is to define variables with high separation power. However, mis-modelling was observed when comparing distributions of variables using b-tagging information for the Z+jets sample with and without using the TRF method.

Figure 6.7 shows the variable $m_{bb}^{\min \Delta R}$ with (left) and without (right) using the TRF method. As expected, the statistical uncertainty is smaller when using the TRF method. This effect is visible comparing the ratio plots. On the other hand, the data is not well modelled. In about half of the bins the uncertainty on the data does not overlap with the MC uncertainty. In the sample without applying the TRF method the MC simulation models the data well within uncertainty. The underflow bin in the left plot is an artefact originating in the different ways of how the b-tagging information is dealt with: Applying the TRF method means that the individual event looses the explicit number of jets that are b-tagged and is set to -1. However, for all variables that do not explicitly use that information such artefacts do not occur. This is visible in the control plots in Section 6.1.

As a consequence, the Z+jets sample that is used for the training of a neural network in the next section the TRF method is not applied. Even though exclusively variables from MC samples are used as an input for the neural network, the shape of the distributions can be different with or without using the TRF method. Additionally, the discrimination between signal and background events in the $t\bar{t}Z$ OSSF dilepton channel is expected to be challenging. Therefore, the variables including b-tagging information are not excluded in favour of using the TRF method. As a consequence, the statistical uncertainty is expected to be higher.

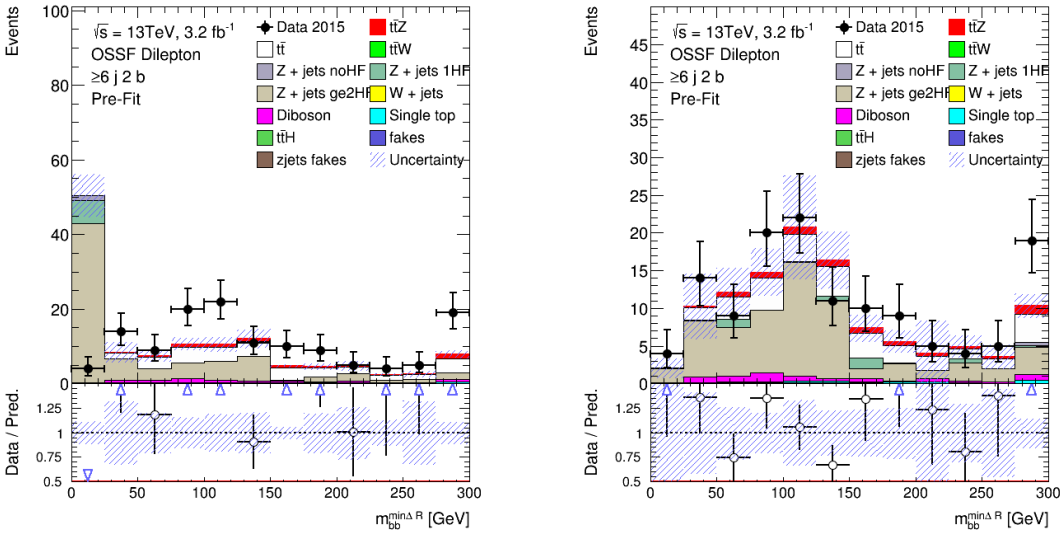

Figure 6.7.: Control Plots for the variable $m_{bb}^{\text{min }\Delta R}$ for the CR (4j, 2b) where the plot on the left uses the tag rate function method for the Z+jets sample. The plot on the right only contains events with exactly 2 b-tags. The b-tagging information is used for this variable but cannot be properly modelled for the TRF function sample.

6.5.2. Uncertainty Scaling

In MC samples a certain number *tot* of events is simulated for a physics process with a certain cross section. The cross section σ varies for different physics processes over a wide range. As a result, the produced events are normalised by

$$norm = \frac{\sigma \cdot k_f}{tot} \tag{6.1}$$

where the k-factor k_f is around 1 and accounts for scaling the cross section to higher order perturbative calculations. *norm* is preferably very low meaning that the number of events produced *tot* is high, the cross section is low so that the number of events is scaled. This then results in a small Poissonian statistical uncertainty $\sqrt{tot}$.

Considering a large background but a low selection efficiency

$$\epsilon = \frac{N_{sel}}{tot}\,, \tag{6.2}$$

the number of selected events N_{sel} is also low and the fluctuation is high.

As an indicator for whether one expects high statistical fluctuations after the event selection the ratio of *norm* and ϵ is calculated. The higher *norm* and the

NEUROBAYES function	Setting
Number of nodes in hidden layer	$n_{\text{var}} + 2$
Update interval for weights	50 events
Maximal learning speed	0.001
Learning speed factor	1
Regularisation	Bayesian
Type of loss function	Entropy
Number of interations	50
Training algorithm	BFGS

Table 6.2.: Parameter settings for training the NEUROBAYES three-layer feed-forward neural network.

lower ϵ, the more one expects statistical fluctuations and the ratio

$$\frac{norm}{\epsilon} = \frac{\frac{\sigma \cdot k_f}{tot}}{\frac{N_{sel}}{tot}} = \frac{\sigma \cdot k_f}{N_{sel}} \tag{6.3}$$

is high.

6.6. Training the Neural Network

The NEUROBAYES [68] algorithm is used to train the two major background samples Z+jets and $t\bar{t}$ against the signal sample $t\bar{t}Z$.

Due to the statistics limitations in the Z+jets sample, cuts on $\sigma \cdot k_f / N_{\text{sel}}$ and *norm* are applied. Z+jets samples are used for the training if they fulfil $\sigma \cdot k_f / N_{\text{sel}} > 0.25$ and $norm > 0.225 \cdot 10^{-3}$. Samples with DSIDs that fail the cuts would cause statistical fluctuations that are too high to achieve a separation between signal and background events. The cut values are obtained by iterative test-trainings and optimised to ensure separation with the least discarded number of raw events. Lists of discarded and used samples, as well as the number of selected events for the used samples are provided in Appendix B.

The backgrounds are trained separately but the settings of the neural network is the same. The only difference is the input for the respective neural network. For training Z+jets against $t\bar{t}Z$ a set of discriminating variables introduced in Section 6.3 is used. Consequently, the variables defined in Section 6.4 are used to train $t\bar{t}$ against $t\bar{t}Z$.

The variables are individually preprocessed before a global preprocessing is applied to all of them. During the individual preprocessing, the distributions are flattened and the mean is defined as the target for the training and not, for example, the width of the distribution. Another flag that is set is whether a variable is continuous like energy or momentum related variables usually are, or has discrete values. The number of jets with a transverse momentum greater than value x is an example for the latter.

Global preprocessing settings are the de-correlation and normalisation of the variables as well as the transformation into a Gaussian distribution.

The configuration for the NEUROBAYES package is summarised in Table 6.2. The number of nodes in the hidden layer depends on the number of input-variables. The details of neural networks are described in Section 5.6. The weights between the nodes are updated every 50 events. The lower that value the more sensitive is the network to fluctuations. The aim is to map trends and general characteristics, so a value of 50 events is reasonable. The reason why the learning speed factor is set to a very low value is the difference in statistics between the target and the training sample. The Z+jets and the $t\bar{t}$ samples are having between 2000 and 4000 raw events while the $t\bar{t}Z$ sample has approximately 35000, one order of magnitude higher.

A Bayesian regularisation means that the weights for the connections between the nodes are divided into three categories. One is for the bias node in the input layer itself. The second is for all connections between the input variable nodes and the hidden layer and the third category comprises the weights of the connections between the hidden layer and the output node. The loss function that is going to be minimised is the entropy. For a more detailed description see Section 5.6.1. The maximum number of training iterations when the algorithm has to find the minimum of the loss function is set to 50. The training method is the BFGS algorithm [69].

Table 6.4 lists the variables used in the training for the Z+jets and $t\bar{t}$ samples. At first, the algorithm is trained with all listed input-variables. It calculates the ranking of the variables according to the significance they add to the separation which is based on their correlation to the target (cf. Section 5.6.1). The variable labelled as *discarded* was discarded by the algorithm because it does not contribute any further learning information.

Training Sample	Raw Events	Type
$t\bar{t}Z$	37411	signal
Z+jets	4039	background
$t\bar{t}$	2303	background

Table 6.3.: Statistics in the MC samples used for the training. The $t\bar{t}Z$ signal sample is an order of magnitude larger then the Z+jets and $t\bar{t}$ background samples. Hence, higher statistical fluctuations are expected for the latter two.

	Z+jets		$t\bar{t}$	
Rank	**Variable**	**Added Sign.**	**Variable**	**Added Sign.**
1	$m_{jj}^{\text{max } p_{\text{T}}}$	27.53	p_{T}^{ll}	36.37
2	$\Delta R_{bb}^{\text{max } p_{\text{T}}}$	19.42	m_{ll}	26.26
3	$\Delta\eta_{jj}^{\text{max } \Delta\eta}$	6.61	$m_{jj}^{\text{max } p_{\text{T}}}$	13.78
4	$m_{jj}^{\text{min mass}}$	6.73	N_{jet}^{40}	10.78
5	$m_{bb}^{\text{min } \Delta R}$	3.64	$\Delta\eta_{jj}^{\text{max } \Delta\eta}$	10.08
6	$m_{bb}^{p_{\text{T}} \text{ ord}}$	discarded	$H_{\text{T}}^{\text{all}}$	3.78
7			ΔR_{ll}	3.09
8			max $m_{lb}^{\text{min } \Delta R}$	2.65

Table 6.4.: Ranking of the input-variables for training the Z+jets and the $t\bar{t}$ samples against the target sample $t\bar{t}Z$. The variables are ranked according to their significance they add to the neural network.

After that, the number of input-variables is optimised to maximise the separation. In an iterative process variables are removed starting with the one of lowest added significance while the training is performed again for each number of input-variables. The algorithm calculates the area under the ROC curve as a quality measure for the separation. Additionally, the processes are tested for overtraining and the training with the best separation and the lowest overtraining is considered as the final configuration. For both training samples the optimal number of input-variables is 5. The results are presented in the following Section 6.7.

6.7. Results and Discussion

The main goal of a training process using neural networks is to find a discriminant, the output node, which is powerful enough to separate signal from background events. Furthermore, this discriminant is expected to be applicable to any unknown data set and guarantees good separation as well.

This is not obvious because there is the possibility that the neural network does not learn the general characteristics of the samples it is trained on but learns *too much* about the samples' properties. Applied to an unknown data set the discriminant is then reproducing these details rather then performing a separation based on general properties. This effect is called *overtraining*.

To test the final discriminant for overtraining the signal and the background samples are split into two, each. Each event contained in the samples has an event number. The splitting is done into events with even and with odd event numbers. The training is then performed on the even event samples and they are tested on the odd event samples and vice versa.

In the next Section 6.7.1 the training results are described and the quality of the final discriminant is assessed. Section 6.7.2 shows the results of the overtraining tests of the final discriminant. Both sections present and discuss the results of the Z+jets and $t\bar{t}$ background trainings against the $t\bar{t}Z$ signal sample. The procedure is the same for both training processes.

6.7.1. Discriminant Building and Two-fold Validation

In this section, the two-fold validation and the discriminant building is described. Figure 6.8 shows a schematic of the two-fold validation. After the signal and background samples have been split into sub-samples *even* and *odd*, two neural networks are trained: One trains the odd background sample against the odd signal sample and the same is done for the even samples. Hence two discriminants are obtained. The discriminant from training the odd samples is then applied to the even samples and vice versa.

The plots in the left column of Figure 6.9 show the results. Dots with error bars show the result of applying the discriminant obtained by training to the odd samples on the even samples. The filled colour histograms show the separation of the odd samples after the discriminant from training on the even samples is applied.

By definition, the trainings do not produce the exact same distributions because they are performed on independent subsets of events. Splitting the original samples into half also decreases the statistics for the trainings. To avoid confusion and overloaded plots, error bars are only shown for the dots.

As expected, the red background sub-samples have higher statistical fluctuations than the blue dots, for both background samples, Z+jets and $t\bar{t}$. As summarised in Table 6.3, the number of raw events before splitting is 37411 for the $t\bar{t}Z$ signal sample and the Z+jets and $t\bar{t}$ samples comprise 4039 and 2303 raw events, respectively. Therefore, these fluctuations are expected.

To exploit the whole statistics of the samples, the two discriminants are combined. The right column of Figure 6.9 shows the ROC curves for the two trainings in red and blue. Additionally the ROC curve for the combined discriminant is shown in green.

The Frico-Gini index is a measure for the separation. It calculates the ratio of the area covered by the bending of the ROC curve. The Frico-Gini index is 0% for no separation power which is equivalent to a diagonal from $(0,1)$ to $(1,0)$ with $\left(\epsilon_{sig}, 1-\epsilon_{bkg}\right)$. It is 100% for an optimal separation in case the ROC curve covers the whole area of the triangle $(0,1)$, $(1,1)$, $(1,0)$. Calculated is the area between the diagonal and the ROC curve divided by the area of the triangle. The separation power of the discriminants is higher for the $t\bar{t}$ background, indicated by the Frico-Gini index.

Even though the fluctuations are visible because the curves are slightly different, the ROC curves indicate that a separation is achieved to distinguish signal from background events for both background processes.

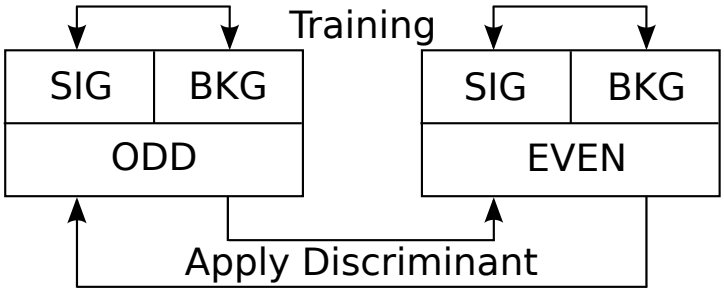

Figure 6.8.: Two-fold validation schematic.

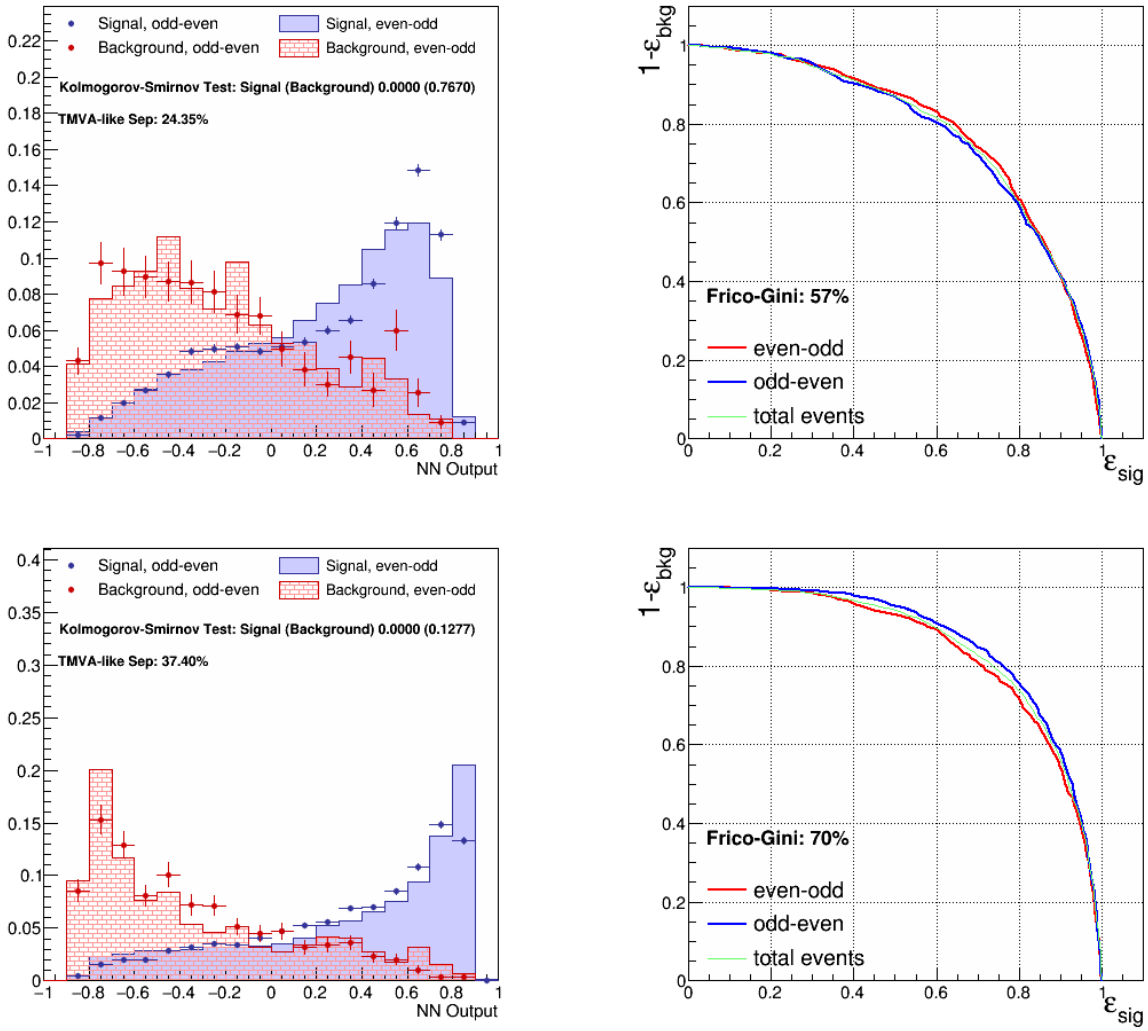

Figure 6.9.: Two-fold validation for training Z+jets (upper row) and $t\bar{t}$ (bottom row) background samples against the $t\bar{t}Z$ signal sample.

6.7.2. Overtraining Test

Figure 6.10 illustrates the procedure for the overtraining test. The training is only performed in the odd samples. To test whether the final discriminant reproduces the patterns of the samples it was trained on, it is applied to these samples itself. The separation is given by the coloured histograms. Afterwards, the discriminant is applied to the even samples. The result is given by the dotted histograms.

For the ideal discriminant the separation distributions for both applications are exactly the same. For the signal sample, the distributions agree well within the statistical uncertainties. Expecting the error bars of the coloured background sample to be of the same order as the errors on the dotted histogram, also these distributions agree within uncertainties. This indicates that there is no significant overtraining for both background samples. The respective ROC curves in the right column of Figure 6.11 mirror the statistical fluctuations in the background samples.

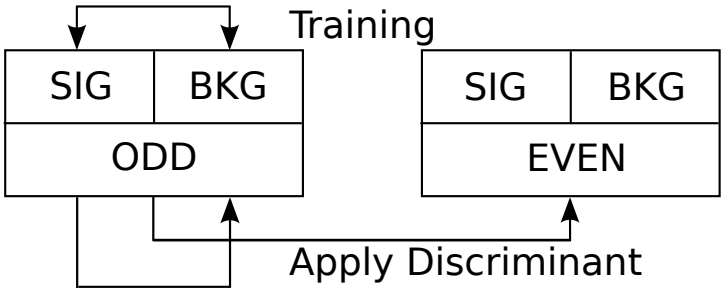

Figure 6.10.: Overtraining schematic.

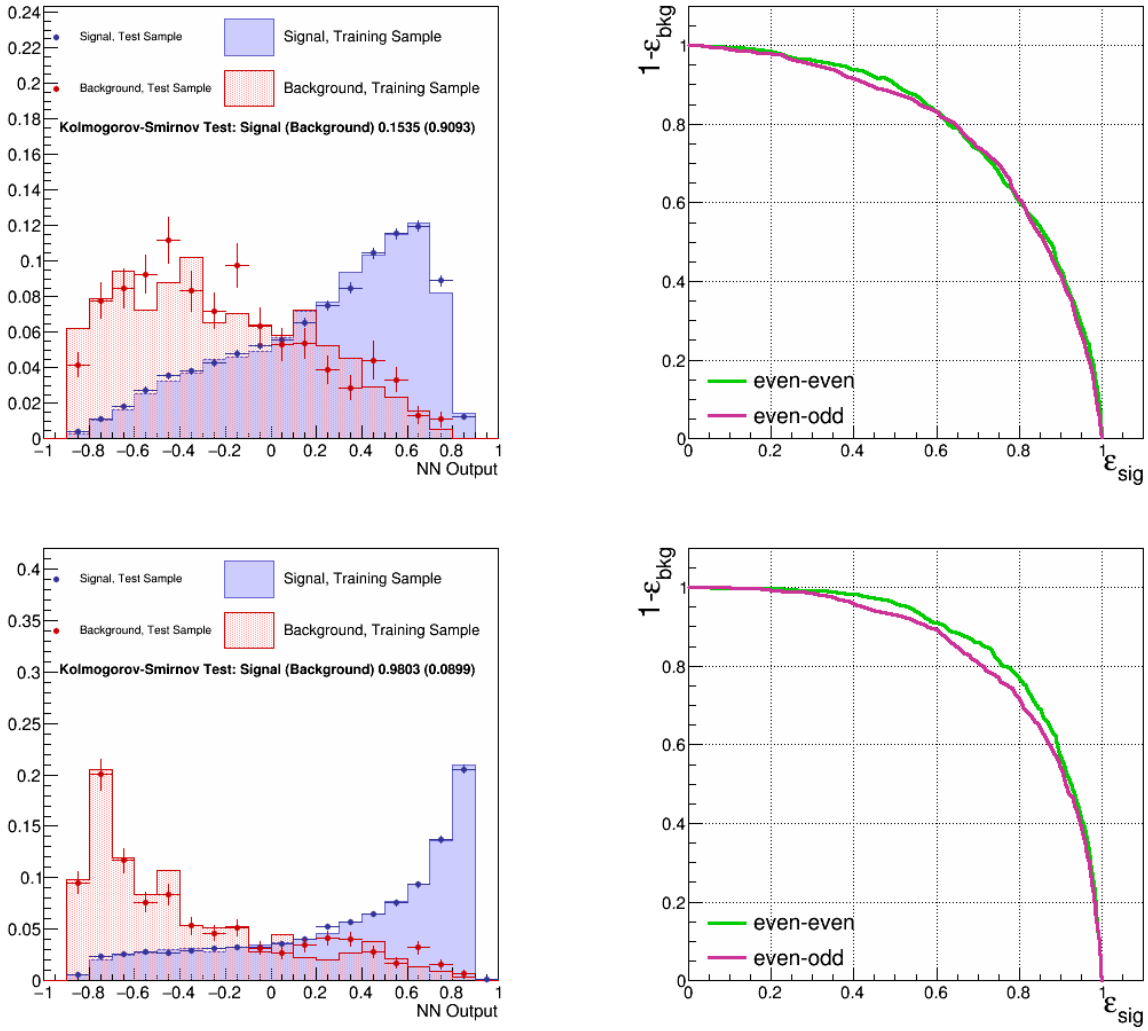

Figure 6.11.: Overtraining test for the Z+jets (upper row) and the $t\bar{t}$ background sample trained against the $t\bar{t}Z$ signal sample.

7. Conclusions and Outlook

With only two OSSF leptons in the final state of the $t\bar{t}Z$ process, studies of this channel are challenging due to low statistics and a small S/B ratio in the signal region. However, by training two neural networks a good separation between $t\bar{t}Z$ signal events and events of the two main background processes, Z+jets and $t\bar{t}$ was achieved. Furthermore, the two obtained discriminants do not show indications for overtraining and can be applied on data samples to distinguish signal from background events.

For improving the MC modelling more Z+jets MC samples are necessary to decrease statistical fluctuations. Higher statistics can also improve the result of the neural network training because the algorithms can produce better discriminants when the provided information in the form of training events is higher. As described in Sections 6.3 and 6.4, additional variables with good separation power can furthermore increase the neural network performance by adding them to the training. Higher statistics in the training samples also allows to use more input variables and achieve a good training. With higher statistics the separation distributions and the ROC curves are expected to be smoother although the achieved separation is already good, as indicated by the Frico-Gini index.

All in all, the presented studies show that, in addition to the three and four lepton channels, the OSSF lepton decay channel is suitable for studies of $t\bar{t}Z$ processes and to gain knowledge about the vector$-$axial-vector coupling of the weak neutral current by studying the tZ vertex.

A. Kinematic Control Distributions

The following figures show kinematic control distributions in addition to the ones that are discussed in Section 6.1. Distributions that are already shown in Figures 6.1 and 6.2 are listed again. Different variables for the control regions (4j, 2b) and (5j, 2b) as well as for the signal region ($\geq$6j, 2b) are listed from top to bottom for each of the figures.

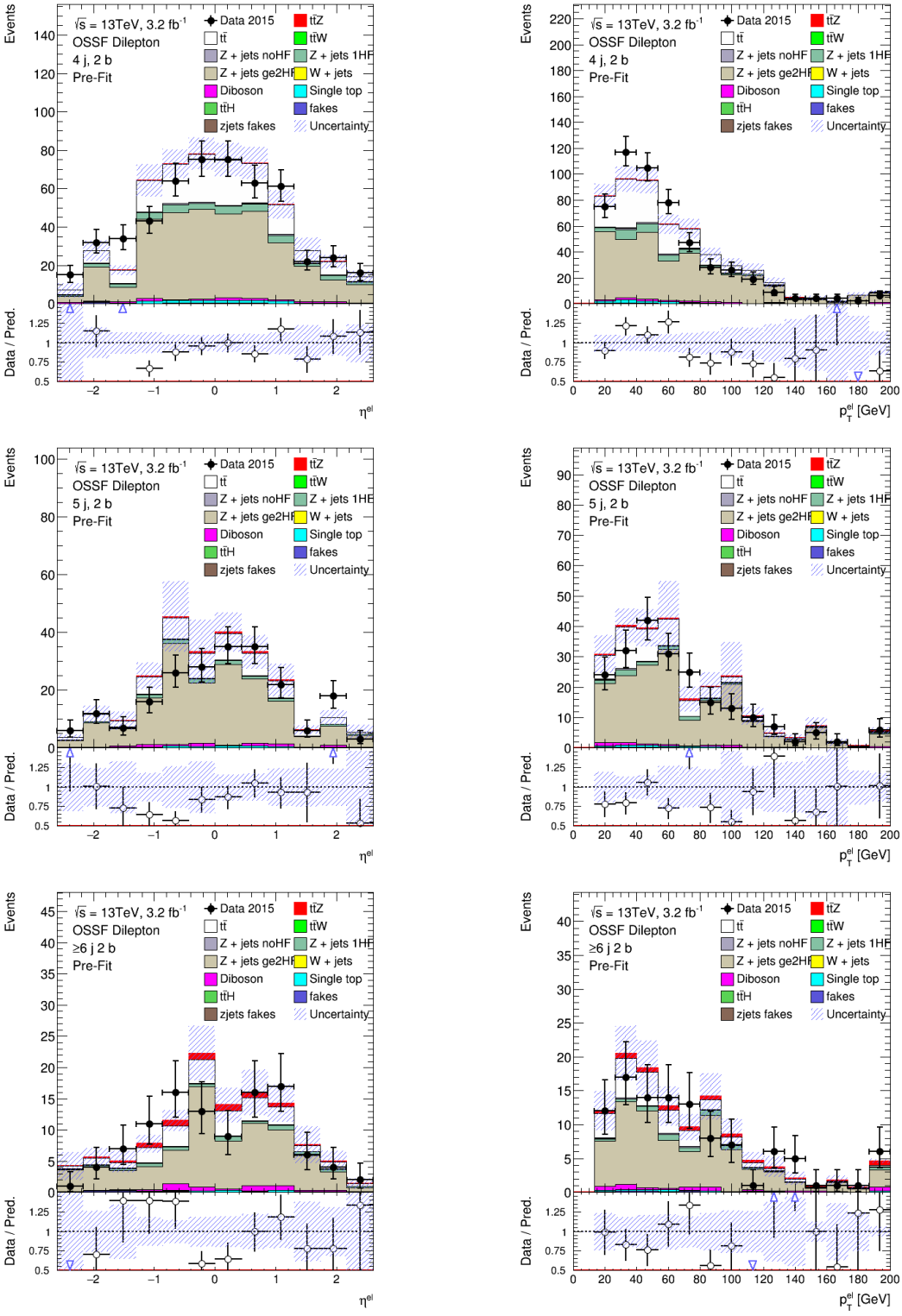

Figure A.1.: Electron pseudorapidity η^{el} (left) and transverse momentum $p_{\mathrm{T}}^{\mathrm{el}}$ (right) for the control regions (4j, 2b), (5j, 2b) and the signal region ($\geq$6j, 2b) from top to bottom.

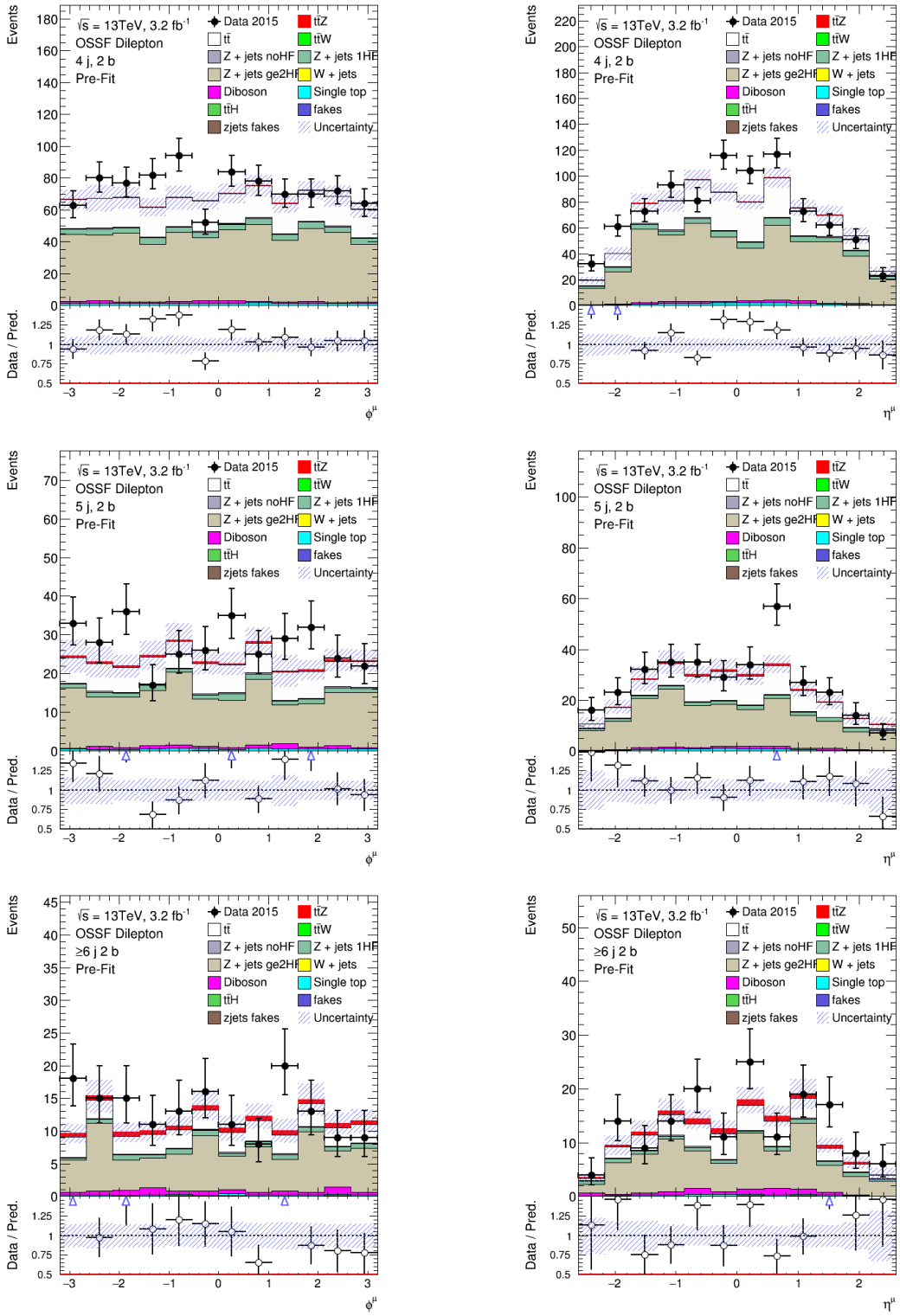

Figure A.2.: Muon angular distribution ϕ^{μ} (left) and η^{μ} (right) for the control regions (4j, 2b), (5j, 2b) and the signal region ($\geq$6j, 2b) from top to bottom.

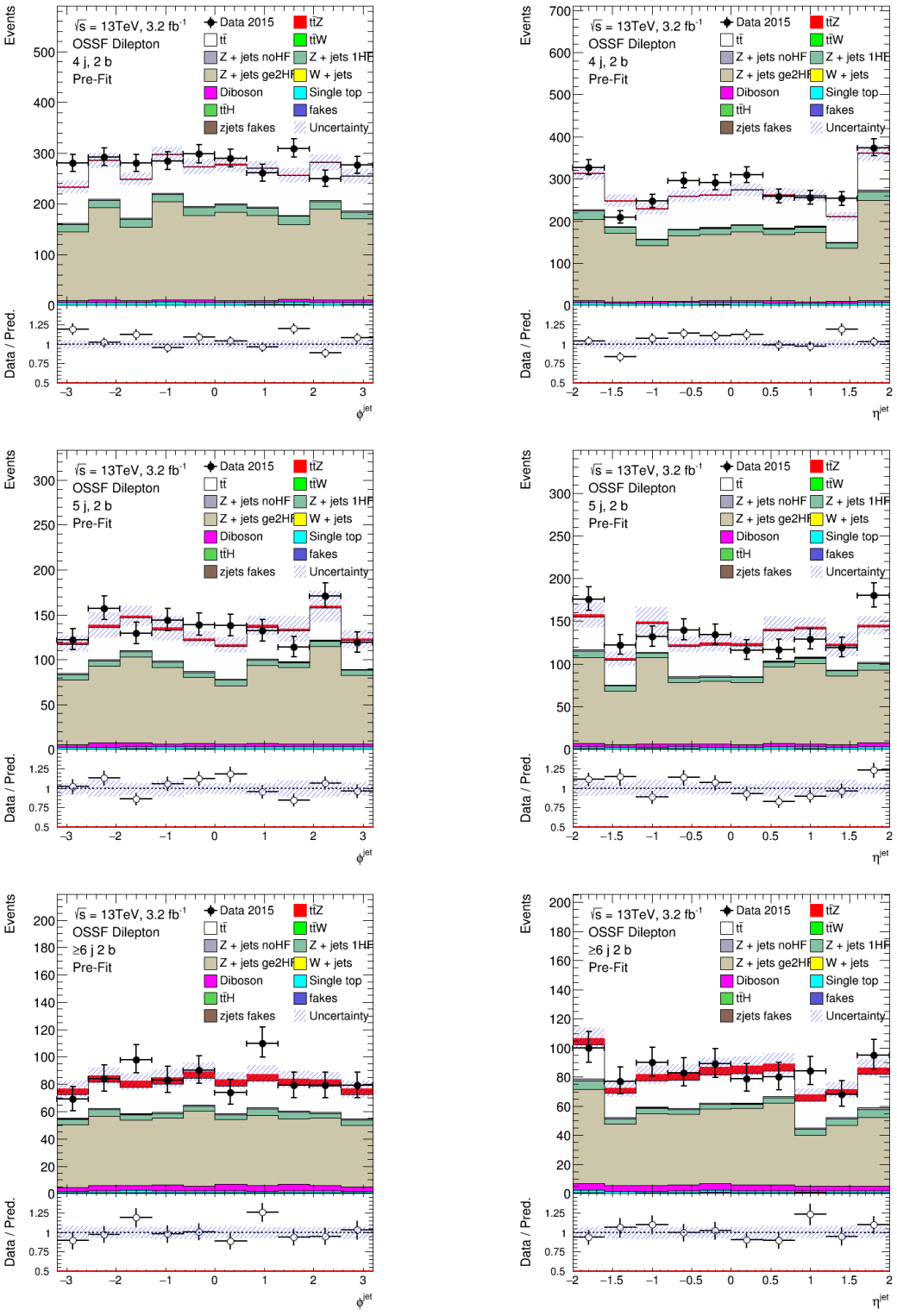

Figure A.3.: Jet angular distribution ϕ^{jet} (left) and η^{jet} (right) for the control regions (4j, 2b), (5j, 2b) and the signal region ($\geq$6j, 2b) from top to bottom.

B. Studies of Z+jets Statistics

Discarded Samples

DSID	N_{sel}	xs*kf	tot	norm	N_{sel}/tot	xs*kf/N_{sel}
361373	6	282.604	362679	0.000779212	1.65436e-05	47.1006
361374	60	157.996	275773	0.000572919	0.00021757	2.63326
361376	21	15.062	88185.1	0.0001708	0.000238135	0.717237
361377	120	8.97003	39111.2	0.000229347	0.00306818	0.0747503
361378	2	6.44051	49892.9	0.000129087	4.00859e-05	3.22025
361379	10	2.54515	15079.5	0.000168782	0.000663152	0.254515
361380	52	1.5401	5163.12	0.000298288	0.0100714	0.0296173
361396	1	1547.16	1.35106e+06	0.00114515	7.40161e-07	1547.16
361397	17	282.604	706018	0.000400278	2.40787e-05	16.6237
361398	372	157.996	1.07875e+06	0.000146462	0.000344843	0.424719
361399	2	44.4047	419437	0.000105868	4.7683e-06	22.2024
361400	51	15.062	150171	0.000100299	0.000339612	0.295333
361401	187	8.97003	38069.3	0.000235624	0.00491209	0.0479681
361402	3	6.44051	78243.5	8.23136e-05	3.83418e-05	2.14684
361403	10	2.54515	14871.2	0.000171147	0.000672443	0.254515
361404	61	1.5401	5044.5	0.000305303	0.0120924	0.0252475
361424	1	15.062	88918.9	0.00016939	1.12462e-05	15.062
361425	1	8.97003	38310.5	0.00023414	2.61025e-05	8.97003
361427	1	2.54515	14678	0.000173398	6.8129e-05	2.54515
361428	1	1.5401	4759.73	0.000323569	0.000210096	1.5401
361469	3	95.746	206047	0.00046468	1.45598e-05	31.9153
361470	23	6.27298	256674	2.44394e-05	8.96077e-05	0.272738
361477	4	95.874	204445	0.000468947	1.95651e-05	23.9685
361478	19	6.25332	257572	2.42779e-05	7.37657e-05	0.329122

Table B.1.: Z+jets samples that are discarded from the training. These DSIDs do not fulfil $\sigma \cdot k_f / N_{\text{sel}} > 0.25$ and $norm > 0.225 \cdot 10^{-3}$. It was observed that these samples cause statistical fluctuations that make a separation between signal and background not possible using an NN.

Used Samples

DSID	N_{sel}	xs*kf	tot	norm	N_{sel}/tot	xs*kf/N_{sel}
361381	8	0.402179	211433	1.90216e-06	3.7837e-05	0.0502723
361382	276	0.18138	144046	1.25918e-06	0.00191605	0.000657174
361383	3604	0.109848	154137	7.12667e-07	0.0233819	3.04795e-05
361384	14	0.0237426	127534	1.86167e-07	0.000109775	0.0016959
361385	334	0.0112289	97519.1	1.15146e-07	0.00342497	3.36195e-05
361386	3546	0.00716615	99234.9	7.2214e-08	0.0357334	2.02091e-06
361387	3	0.0040959	20952.4	1.95486e-07	0.000143182	0.0013653
361388	56	0.0021539	14703.2	1.46492e-07	0.0038087	3.84625e-05
361389	664	0.00131506	15676.3	8.38884e-08	0.042357	1.98051e-06
361390	2	0.000526354	12403.4	4.24361e-08	0.000161246	0.000263177
361391	27	0.000300076	9834	3.05142e-08	0.00274558	1.11139e-05
361392	208	0.000178131	11268.5	1.58079e-08	0.0184586	8.56401e-07
361393	2	1.85997e-06	8076.86	2.30284e-10	0.000247621	9.29985e-07
361394	2	1.1746e-06	4918.06	2.38833e-10	0.000406664	5.87298e-07
361395	34	7.81538e-07	5141.83	1.51996e-10	0.00661243	2.29864e-08
361405	16	0.402179	211242	1.90388e-06	7.57426e-05	0.0251362
361406	404	0.18138	142861	1.26963e-06	0.00282793	0.000448961
361407	4497	0.109848	155469	7.06557e-07	0.0289253	2.44269e-05
361408	15	0.0237426	125805	1.88725e-07	0.000119232	0.00158284
361409	322	0.0112289	98250.3	1.14289e-07	0.00327734	3.48724e-05
361410	3953	0.00716615	106936	6.70135e-08	0.036966	1.81284e-06
361411	4	0.0040959	20240.6	2.02361e-07	0.000197623	0.00102398
361412	44	0.0021539	14477.6	1.48774e-07	0.00303917	4.89522e-05
361413	609	0.00131506	16146.9	8.14432e-08	0.0377161	2.15937e-06
361414	4	0.000526354	13005.5	4.04715e-08	0.000307561	0.000131588
361415	41	0.000300076	9628.18	3.11664e-08	0.00425833	7.31893e-06
361416	362	0.000178131	10549.3	1.68856e-08	0.0343151	4.92075e-07
361417	3	1.85997e-06	7992.79	2.32706e-10	0.000375339	6.1999e-07
361418	19	1.1746e-06	4526.49	2.59494e-10	0.00419751	6.18209e-08
361419	176	7.81538e-07	5021.86	1.55627e-10	0.0350468	4.44056e-09
361430	3	0.18138	143564	1.26341e-06	2.08966e-05	0.06046
361431	75	0.109848	154681	7.1016e-07	0.00048487	0.00146464

Table B.2.: Z+jets samples that are used for the training. These DSIDs fulfil $\sigma \cdot k_f / N_{\text{sel}} > 0.25$ and $norm > 0.225 \cdot 10^{-3}$. That is needed to avoid statistical fluctuations that make a separation between signal and background using an NN not possible.

DSID	N_{sel}	xs*kf	tot	norm	N_{sel}/tot	xs*kf/N_{sel}
361433	3	0.0112289	97509.6	1.15157e-07	3.07662e-05	0.00374297
361434	76	0.00716615	107103	6.69091e-08	0.000709599	9.42914e-05
361437	14	0.00131506	16643.4	7.90137e-08	0.000841174	9.39327e-05
361439	1	0.000300076	9900.76	3.03084e-08	0.000101002	0.000300076
361440	9	0.000178131	11528	1.5452e-08	0.000780705	1.97924e-05
361471	65	0.697756	43741	1.5952e-05	0.00148602	0.0107347
361472	29	0.556503	137178	4.05679e-06	0.000211404	0.0191898
361473	289	0.066886	50988.1	1.3118e-06	0.00566799	0.000231439
361475	46	0.00135015	24986.9	5.40341e-08	0.00184096	2.9351e-05
361479	115	0.715182	43683.7	1.63718e-05	0.00263256	0.00621898
361480	40	0.560199	136203	4.11298e-06	0.000293679	0.014005
361481	391	0.0743931	50973.6	1.45945e-06	0.00767064	0.000190264
361482	25	0.00566189	39630	1.42869e-07	0.000630835	0.000226475
361483	384	0.00136096	24863.4	5.47376e-08	0.0154444	3.54417e-06
361489	3	0.0750899	51674.5	1.45313e-06	5.80557e-05	0.02503
361491	2	0.00129517	24624.8	5.2596e-08	8.12188e-05	0.000647584

Table B.3.: Z+jets samples that are used for the training. These DSIDs fulfil $\sigma \cdot k_f / N_{\text{sel}} > 0.25$ and $norm > 0.225 \cdot 10^{-3}$. That is needed to avoid statistical fluctuations that make a separation using a NN not possible.

Selected Events

	N_{sel}				
DSID	total	4j2b	5j2b	ge6j2b	xs*kf/N_{sel}
361381	8	3	3	2	0.0502723
361382	276	111	59	68	0.000657174
361383	3604	1349	807	698	3.04795e-05
361384	14	5	3	2	0.0016959
361385	334	103	79	91	3.36195e-05
361386	3546	1093	806	846	2.02091e-06
361387	3	3	0	0	0.0013653
361388	56	8	16	25	3.84625e-05
361389	664	159	153	200	1.98051e-06
361390	2	0	1	1	0.000263177

Table B.4.: Samples that are used for training an NN. Shown is the selection for the three control and signal regions.

DSID	N_{sel} total	4j2b	5j2b	ge6j2b	xs*kf/N_{sel}
361391	27	7	5	6	1.11139e-05
361392	208	51	37	59	8.56401e-07
361393	2	1	0	1	9.29985e-07
361394	2	1	0	1	5.87298e-07
361395	34	1	2	7	2.29864e-08
361405	16	6	4	1	0.0251362
361406	404	153	85	68	0.000448961
361407	4497	1557	927	817	2.44269e-05
361408	15	3	4	5	0.00158284
361409	322	81	71	84	3.48724e-05
361410	3953	1052	786	889	1.81284e-06
361411	4	2	1	1	0.00102398
361412	44	6	10	11	4.89522e-05
361413	609	117	106	161	2.15937e-06
361414	4	1	0	2	0.000131588
361415	41	4	7	8	7.31893e-06
361416	362	76	49	78	4.92075e-07
361417	3	0	1	0	6.1999e-07
361418	19	2	2	2	6.18209e-08
361419	176	23	17	35	4.44056e-09
361430	3	0	0	0	0.06046
361431	75	0	0	0	0.00146464
361433	3	0	0	0	0.00374297
361434	76	1	0	0	9.42914e-05
361437	14	0	0	0	9.39327e-05
361439	1	0	0	0	0.000300076
361440	9	0	0	0	1.97924e-05
361471	65	0	0	0	0.0107347
361472	29	0	0	0	0.0191898
361473	289	0	0	0	0.000231439
361475	46	0	0	0	2.9351e-05
361479	115	0	0	0	0.00621898
361480	40	0	0	0	0.014005
361481	391	0	0	0	0.000190264
361482	25	0	0	0	0.000226475
361483	384	0	0	0	3.54417e-06
361489	3	0	0	0	0.02503
361491	2	0	0	0	0.000647584

Table B.5.: Samples that are used for training an NN. Shown is the selection for the three control and signal regions.

C. Monte Carlo Samples

$t\bar{t}$

user.mdubovsk.410000.PowhegPythiaEvtGen.DAOD_TOPQ1.e3698_s2608_s2183
_r7267_r6282_p2516.02-03-450_output.root/
user.mdubovsk.410009.PowhegPythiaEvtGen.DAOD_TOPQ1.e3698_s2608_s2183
_r7267_r6282_p2516.02-03-450_output.root/

$t\bar{t}V$

user.mdubovsk.410050.MadGraphPythiaEvtGen.DAOD_TOPQ1.e4279_s2608_s2183
_r7326_r6282_p2516.02-03-45_output.root/
user.mdubovsk.410066.MadGraphPythia8EvtGen.DAOD_TOPQ1.e4111_s2608_s2183
_r7326_r6282_p2516.02-03-450_output.root/
user.mdubovsk.410067.MadGraphPythia8EvtGen.DAOD_TOPQ1.e4111_s2608_s2183
_r7326_r6282_p2516.02-03-450_output.root/
user.mdubovsk.410068.MadGraphPythia8EvtGen.DAOD_TOPQ1.e4111_s2608_s2183
_r7326_r6282_p2516.02-03-45_output.root/
user.mdubovsk.410069.MadGraphPythia8EvtGen.DAOD_TOPQ1.e4111_s2608_s2183
_r7326_r6282_p2471.02-03-45_output.root/
user.mdubovsk.410070.MadGraphPythia8EvtGen.DAOD_TOPQ1.e4111_s2608_s2183
_r7326_r6282_p2471.02-03-45_output.root/
user.mdubovsk.410073.MadGraphPythia8EvtGen.DAOD_TOPQ1.e4111_s2608_s2183
_r7326_r6282_p2516.02-03-450_output.root/
user.mdubovsk.410074.MadGraphPythia8EvtGen.DAOD_TOPQ1.e4143_s2608_s2183
_r7326_r6282_p2516.02-03-450_output.root/
user.mdubovsk.410075.MadGraphPythia8EvtGen.DAOD_TOPQ1.e4111_s2608_s2183
_r7326_r6282_p2516.02-03-450_output.root/
user.mdubovsk.410111.MadGraphPythia8EvtGen.DAOD_TOPQ1.e4632_s2726_r7326
_r6282_p2516.02-03-450_output.root/
user.mdubovsk.410112.MadGraphPythia8EvtGen.DAOD_TOPQ1.e4632_s2726_r7326
_r6282_p2516.02-03-450_output.root/
user.mdubovsk.410113.MadGraphPythia8EvtGen.DAOD_TOPQ1.e4632_s2726_r7326
_r6282_p2516.02-03-450_output.root/

user.mdubovsk.410114.MadGraphPythia8EvtGen.DAOD_TOPQ1.e4632_s2726_r7326
_r6282_p2516.02-03-450_output.root/
user.mdubovsk.410115.MadGraphPythia8EvtGen.DAOD_TOPQ1.e4632_s2726_r7326
_r6282_p2516.02-03-450_output.root/
user.mdubovsk.410115.MadGraphPythia8EvtGen.DAOD_TOPQ1.e4632_s2726_r7326
_r6282_p2516.02-03-450_output.root/
user.mdubovsk.410116.MadGraphPythia8EvtGen.DAOD_TOPQ1.e4632_s2726_r7326
_r6282_p2516.02-03-450_output.root/

$t\bar{t}H$

user.mdubovsk.341177.aMcAtNloHerwigppEvtGen.DAOD_TOPQ1.e4277_s2608_s2183
_r6869_r6282_p2516.02-03-45_ttH_output.root/
user.mdubovsk.341271.aMcAtNloHerwigppEvtGen.DAOD_TOPQ1.e4277_s2608_s2183
_r6869_r6282_p2516.02-03-45_ttH_output.root/
user.mdubovsk.341270.aMcAtNloHerwigppEvtGen.DAOD_TOPQ1.e4277_s2608_s2183
_r6869_r6282_p2516.02-03-45_ttH_output.root/

Single Top

user.mdubovsk.410011.PowhegPythiaEvtGen.DAOD_TOPQ1.e3824_s2608_s2183
_r7326_r6282_p2516.02-03-450_output.root/
user.mdubovsk.410012.PowhegPythiaEvtGen.DAOD_TOPQ1.e3824_s2608_s2183
_r7326_r6282_p2516.02-03-450_output.root/
user.mdubovsk.410013.PowhegPythiaEvtGen.DAOD_TOPQ1.e3753_s2608_s2183
_r7326_r6282_p2516.02-03-450_output.root/
user.mdubovsk.410014.PowhegPythiaEvtGen.DAOD_TOPQ1.e3753_s2608_s2183
_r7326_r6282_p2516.02-03-45_output.root/
user.mdubovsk.410015.PowhegPythiaEvtGen.DAOD_TOPQ1.e3753_s2608_s2183
_r7326_r6282_p2516.02-03-450_output.root/
user.mdubovsk.410016.PowhegPythiaEvtGen.DAOD_TOPQ1.e3753_s2608_s2183
_r7326_r6282_p2516.02-03-45_output.root/
user.mdubovsk.410025.PowhegPythiaEvtGen.DAOD_TOPQ1.e3998_s2608_s2183
_r7326_r6282_p2516.02-03-45_output.root/
user.mdubovsk.410026.PowhegPythiaEvtGen.DAOD_TOPQ1.e3998_s2608_s2183
_r7326_r6282_p2516.02-03-45_output.root/

Diboson

user.mdubovsk.361063.Sherpa_CT10_llll.DAOD_TOPQ1.e3836_s2608_s2183
_r7267_r6282_p2516.02-03-450_output.root/
user.mdubovsk.361064.Sherpa.DAOD_TOPQ1.e3836_s2608_s2183
_r7267_r6282_p2516.02-03-450_output.root/
user.mdubovsk.361065.Sherpa.DAOD_TOPQ1.e3836_s2608_s2183
_r7267_r6282_p2516.02-03-450_output.root/
user.mdubovsk.361066.Sherpa.DAOD_TOPQ1.e3836_s2608_s2183
_r7267_r6282_p2516.02-03-450_output.root/
user.mdubovsk.361067.Sherpa.DAOD_TOPQ1.e3836_s2608_s2183
_r7267_r6282_p2516.02-03-450_output.root/
user.mdubovsk.361068.Sherpa_CT10_llvv.DAOD_TOPQ1.e3836_s2608_s2183
_r7267_r6282_p2516.02-03-450_output.root/
user.mdubovsk.361069.Sherpa.DAOD_TOPQ1.e3836_s2608_s2183
_r7267_r6282_p2460.02-03-450_output.root/
user.mdubovsk.361070.Sherpa.DAOD_TOPQ1.e3836_s2608_s2183
_r7267_r6282_p2516.02-03-450_output.root/
user.mdubovsk.361071.Sherpa.DAOD_TOPQ1.e3836_s2608_s2183
_r7326_r6282_p2516.02-03-450_output.root/
user.mdubovsk.361072.Sherpa.DAOD_TOPQ1.e3836_s2608_s2183
_r7326_r6282_p2516.02-03-450_output.root/
user.mdubovsk.361077.Sherpa_CT10_ggllvv.DAOD_TOPQ1.e4641
_s2726_r7326_r6282_p2516.02-03-450_output.root/
user.mdubovsk.361078.Sherpa.DAOD_TOPQ1.e4641_s2726_r7326
_r6282_p2471.02-03-450_output.root/
user.mdubovsk.361081.Sherpa_CT10_WplvWmqq.DAOD_TOPQ1.e3836_s2608_s2183
_r7326_r6282_p2516.02-03-450_output.root/
user.mdubovsk.361082.Sherpa_CT10_WpqqWmlv.DAOD_TOPQ1.e3836_s2608_s2183
_r7326_r6282_p2516.02-03-450_output.root/
user.mdubovsk.361083.Sherpa_CT10_WlvZqq.DAOD_TOPQ1.e3836_s2608_s2183
_r7326_r6282_p2516.02-03-450_output.root/
user.mdubovsk.361084.Sherpa_CT10_WqqZll.DAOD_TOPQ1.e3836_s2608_s2183
_r7326_r6282_p2516.02-03-450_output.root/
user.mdubovsk.361086.Sherpa_CT10_ZqqZll.DAOD_TOPQ1.e3926_s2608_s2183
_r7326_r6282_p2516.02-03-450_output.root/

Z+jets

user.mdubovsk.361372.Sherpa.DAOD_TOPQ1.e3651_s2586_s2174
_r7267_r6282_p2516.02-03-450_output.root/
user.mdubovsk.361373.Sherpa.DAOD_TOPQ1.e3651_s2586_s2174
_r7267_r6282_p2516.02-03-450_output.root/
user.mdubovsk.361374.Sherpa.DAOD_TOPQ1.e3651_s2586_s2174
_r7267_r6282_p2516.02-03-450_output.root/
user.mdubovsk.361375.Sherpa.DAOD_TOPQ1.e3651_s2586_s2174
_r7267_r6282_p2516.02-03-45_output.root/
user.mdubovsk.361376.Sherpa.DAOD_TOPQ1.e3651_s2586_s2174
_r7267_r6282_p2516.02-03-450_output.root/
user.mdubovsk.361377.Sherpa.DAOD_TOPQ1.e3651_s2586_s2174
_r7267_r6282_p2516.02-03-450_output.root/
user.mdubovsk.361378.Sherpa.DAOD_TOPQ1.e3651_s2586_s2174
_r7267_r6282_p2516.02-03-45_output.root/
user.mdubovsk.361379.Sherpa.DAOD_TOPQ1.e3651_s2586_s2174
_r7267_r6282_p2516.02-03-450_output.root/
user.mdubovsk.361380.Sherpa.DAOD_TOPQ1.e3651_s2586_s2174
_r7267_r6282_p2516.02-03-45_output.root/
user.mdubovsk.361381.Sherpa.DAOD_TOPQ1.e4133_s2608_s2183
_r7326_r6282_p2516.02-03-450_output.root/
user.mdubovsk.361382.Sherpa.DAOD_TOPQ1.e4133_s2608_s2183
_r7326_r6282_p2516.02-03-450_output.root/
user.mdubovsk.361383.Sherpa.DAOD_TOPQ1.e4133_s2608_s2183
_r7326_r6282_p2516.02-03-450_output.root/
user.mdubovsk.361384.Sherpa.DAOD_TOPQ1.e4133_s2608_s2183
_r7326_r6282_p2516.02-03-450_output.root/
user.mdubovsk.361385.Sherpa.DAOD_TOPQ1.e4133_s2608_s2183
_r7326_r6282_p2516.02-03-450_output.root/
user.mdubovsk.361386.Sherpa.DAOD_TOPQ1.e4133_s2608_s2183
_r7326_r6282_p2516.02-03-45_output.root/
user.mdubovsk.361387.Sherpa.DAOD_TOPQ1.e4133_s2608_s2183
_r7326_r6282_p2516.02-03-450_output.root/
user.mdubovsk.361388.Sherpa.DAOD_TOPQ1.e4133_s2608_s2183
_r7326_r6282_p2516.02-03-450_output.root/
user.mdubovsk.361389.Sherpa.DAOD_TOPQ1.e4133_s2608_s2183
_r7326_r6282_p2516.02-03-450_output.root/
user.mdubovsk.361390.Sherpa.DAOD_TOPQ1.e4133_s2608_s2183
_r7326_r6282_p2516.02-03-450_output.root/
user.mdubovsk.361391.Sherpa.DAOD_TOPQ1.e4133_s2608_s2183
_r7326_r6282_p2516.02-03-450_output.root/
user.mdubovsk.361392.Sherpa.DAOD_TOPQ1.e4133_s2608_s2183
_r7326_r6282_p2516.02-03-450_output.root/

user.mdubovsk.361393.Sherpa.DAOD_TOPQ1.e4133_s2608_s2183
_r7326_r6282_p2516.02-03-450_output.root/
user.mdubovsk.361394.Sherpa.DAOD_TOPQ1.e4133_s2608_s2183
_r7326_r6282_p2516.02-03-450_output.root/
user.mdubovsk.361395.Sherpa.DAOD_TOPQ1.e4133_s2608_s2183
_r7326_r6282_p2516.02-03-45_output.root/
user.mdubovsk.361396.Sherpa.DAOD_TOPQ1.e3651_s2586_s2174
_r7267_r6282_p2516.02-03-45_output.root/
user.mdubovsk.361397.Sherpa.DAOD_TOPQ1.e3651_s2586_s2174
_r7326_r6282_p2516.02-03-450_output.root/
user.mdubovsk.361398.Sherpa.DAOD_TOPQ1.e3651_s2586_s2174
_r7267_r6282_p2516.02-03-450_output.root/
user.mdubovsk.361399.Sherpa.DAOD_TOPQ1.e3651_s2586_s2174
_r7267_r6282_p2516.02-03-450_output.root/
user.mdubovsk.361400.Sherpa.DAOD_TOPQ1.e3651_s2586_s2174
_r7267_r6282_p2516.02-03-450_output.root/
user.mdubovsk.361401.Sherpa.DAOD_TOPQ1.e3651_s2586_s2174
_r7267_r6282_p2516.02-03-45_output.root/
user.mdubovsk.361402.Sherpa.DAOD_TOPQ1.e3651_s2586_s2174
_r7267_r6282_p2516.02-03-45_output.root/
user.mdubovsk.361403.Sherpa.DAOD_TOPQ1.e3651_s2586_s2174
_r7267_r6282_p2516.02-03-450_output.root/
user.mdubovsk.361404.Sherpa.DAOD_TOPQ1.e3651_s2586_s2174
_r7267_r6282_p2516.02-03-450_output.root/
user.mdubovsk.361405.Sherpa.DAOD_TOPQ1.e4133_s2608_s2183
_r7326_r6282_p2516.02-03-450_output.root/
user.mdubovsk.361406.Sherpa.DAOD_TOPQ1.e4133_s2608_s2183
_r7326_r6282_p2516.02-03-450_output.root/
user.mdubovsk.361407.Sherpa.DAOD_TOPQ1.e4133_s2608_s2183
_r7326_r6282_p2516.02-03-450_output.root/
user.mdubovsk.361408.Sherpa.DAOD_TOPQ1.e4133_s2608_s2183
_r7326_r6282_p2516.02-03-450_output.root/
user.mdubovsk.361409.Sherpa.DAOD_TOPQ1.e4133_s2608_s2183
_r7326_r6282_p2516.02-03-450_output.root/
user.mdubovsk.361410.Sherpa.DAOD_TOPQ1.e4133_s2608_s2183
_r7326_r6282_p2516.02-03-450_output.root/
user.mdubovsk.361411.Sherpa.DAOD_TOPQ1.e4133_s2608_s2183
_r7326_r6282_p2516.02-03-450_output.root/
user.mdubovsk.361412.Sherpa.DAOD_TOPQ1.e4133_s2608_s2183
_r7326_r6282_p2516.02-03-450_output.root/
user.mdubovsk.361413.Sherpa.DAOD_TOPQ1.e4133_s2608_s2183
_r7326_r6282_p2516.02-03-45_output.root/
user.mdubovsk.361414.Sherpa.DAOD_TOPQ1.e4133_s2608_s2183
_r7326_r6282_p2516.02-03-450_output.root/

user.mdubovsk.361415.Sherpa.DAOD_TOPQ1.e4133_s2608_s2183
_r7326_r6282_p2516.02-03-45_output.root/
user.mdubovsk.361416.Sherpa.DAOD_TOPQ1.e4133_s2608_s2183
_r7326_r6282_p2516.02-03-45_output.root/
user.mdubovsk.361417.Sherpa.DAOD_TOPQ1.e4133_s2608_s2183
_r7326_r6282_p2516.02-03-45_output.root/
user.mdubovsk.361418.Sherpa.DAOD_TOPQ1.e4133_s2608_s2183
_r7326_r6282_p2516.02-03-450_output.root/
user.mdubovsk.361419.Sherpa.DAOD_TOPQ1.e4133_s2608_s2183
_r7326_r6282_p2516.02-03-45_output.root/
user.mdubovsk.361420.Sherpa.DAOD_TOPQ1.e3733_s2608_s2183
_r7267_r6282_p2516.02-03-450_output.root/
user.mdubovsk.361421.Sherpa.DAOD_TOPQ1.e3733_s2608_s2183
_r7267_r6282_p2516.02-03-45_output.root/
user.mdubovsk.361422.Sherpa.DAOD_TOPQ1.e3733_s2608_s2183
_r7267_r6282_p2460.02-03-450_output.root/
user.mdubovsk.361423.Sherpa.DAOD_TOPQ1.e3733_s2608_s2183
_r7267_r6282_p2516.02-03-45_output.root/
user.mdubovsk.361424.Sherpa.DAOD_TOPQ1.e3733_s2608_s2183
_r7267_r6282_p2516.02-03-450_output.root/
user.mdubovsk.361425.Sherpa.DAOD_TOPQ1.e3733_s2608_s2183
_r7267_r6282_p2516.02-03-450_output.root/
user.mdubovsk.361426.Sherpa.DAOD_TOPQ1.e3733_s2608_s2183
_r7326_r6282_p2460.02-03-450_output.root/
user.mdubovsk.361427.Sherpa.DAOD_TOPQ1.e3733_s2608_s2183
_r7267_r6282_p2516.02-03-450_output.root/
user.mdubovsk.361428.Sherpa.DAOD_TOPQ1.e3733_s2608_s2183
_r7267_r6282_p2516.02-03-450_output.root/
user.mdubovsk.361429.Sherpa.DAOD_TOPQ1.e4133_s2608_s2183
_r7326_r6282_p2516.02-03-45_output.root/
user.mdubovsk.361430.Sherpa.DAOD_TOPQ1.e4133_s2608_s2183
_r7326_r6282_p2516.02-03-450_output.root/
user.mdubovsk.361431.Sherpa.DAOD_TOPQ1.e4133_s2608_s2183
_r7326_r6282_p2516.02-03-450_output.root/
user.mdubovsk.361432.Sherpa.DAOD_TOPQ1.e4133_s2608_s2183
_r7326_r6282_p2516.02-03-450_output.root/
user.mdubovsk.361433.Sherpa.DAOD_TOPQ1.e4133_s2608_s2183
_r7326_r6282_p2516.02-03-450_output.root/
user.mdubovsk.361434.Sherpa.DAOD_TOPQ1.e4133_s2608_s2183
_r7326_r6282_p2516.02-03-450_output.root/
user.mdubovsk.361435.Sherpa.DAOD_TOPQ1.e4133_s2608_s2183
_r7326_r6282_p2516.02-03-450_output.root/
user.mdubovsk.361436.Sherpa.DAOD_TOPQ1.e4133_s2608_s2183
_r7326_r6282_p2516.02-03-450_output.root/

user.mdubovsk.361437.Sherpa.DAOD_TOPQ1.e4133_s2608_s2183
_r7326_r6282_p2516.02-03-45_output.root/
user.mdubovsk.361438.Sherpa.DAOD_TOPQ1.e4133_s2608_s2183
_r7326_r6282_p2516.02-03-450_output.root/
user.mdubovsk.361439.Sherpa.DAOD_TOPQ1.e4133_s2608_s2183
_r7326_r6282_p2516.02-03-450_output.root/
user.mdubovsk.361440.Sherpa.DAOD_TOPQ1.e4133_s2608_s2183
_r7326_r6282_p2516.02-03-450_output.root/
user.mdubovsk.361441.Sherpa.DAOD_TOPQ1.e4133_s2608_s2183
_r7326_r6282_p2516.02-03-450_output.root/
user.mdubovsk.361442.Sherpa.DAOD_TOPQ1.e4133_s2608_s2183
_r7326_r6282_p2516.02-03-450_output.root/
user.mdubovsk.361443.Sherpa.DAOD_TOPQ1.e4133_s2608_s2183
_r7326_r6282_p2516.02-03-45_output.root/

W+jets

user.mdubovsk.361300.Sherpa.DAOD_TOPQ1.e3651_s2608_s2183
_r7326_r6282_p2516.02-03-450_output.root/
user.mdubovsk.361301.Sherpa.DAOD_TOPQ1.e3651_s2586_s2174
_r7326_r6282_p2516.02-03-450_output.root/
user.mdubovsk.361302.Sherpa.DAOD_TOPQ1.e3651_s2586_s2174
_r7326_r6282_p2516.02-03-450_output.root/
user.mdubovsk.361303.Sherpa.DAOD_TOPQ1.e3651_s2586_s2174
_r7267_r6282_p2516.02-03-450_output.root/
user.mdubovsk.361304.Sherpa.DAOD_TOPQ1.e3651_s2586_s2174
_r7267_r6282_p2516.02-03-450_output.root/
user.mdubovsk.361305.Sherpa.DAOD_TOPQ1.e3651_s2586_s2174
_r7267_r6282_p2516.02-03-450_output.root/
user.mdubovsk.361306.Sherpa.DAOD_TOPQ1.e3651_s2586_s2174
_r7267_r6282_p2516.02-03-450_output.root/
user.mdubovsk.361307.Sherpa.DAOD_TOPQ1.e3651_s2586_s2174
_r7267_r6282_p2516.02-03-450_output.root/
user.mdubovsk.361308.Sherpa.DAOD_TOPQ1.e3651_s2586_s2174
_r7267_r6282_p2516.02-03-450_output.root/
user.mdubovsk.361309.Sherpa.DAOD_TOPQ1.e4133_s2608_s2183
_r7326_r6282_p2516.02-03-450_output.root/
user.mdubovsk.361310.Sherpa.DAOD_TOPQ1.e4133_s2608_s2183
_r7326_r6282_p2516.02-03-450_output.root/

user.mdubovsk.361311.Sherpa.DAOD_TOPQ1.e4133_s2608_s2183
_r7326_r6282_p2516.02-03-450_output.root/
user.mdubovsk.361312.Sherpa.DAOD_TOPQ1.e4133_s2608_s2183
_r7326_r6282_p2516.02-03-450_output.root/
user.mdubovsk.361313.Sherpa.DAOD_TOPQ1.e4133_s2608_s2183
_r7326_r6282_p2516.02-03-450_output.root/
user.mdubovsk.361314.Sherpa.DAOD_TOPQ1.e4133_s2608_s2183
_r7326_r6282_p2516.02-03-450_output.root/
user.mdubovsk.361315.Sherpa.DAOD_TOPQ1.e4133_s2608_s2183
_r7326_r6282_p2516.02-03-450_output.root/
user.mdubovsk.361316.Sherpa.DAOD_TOPQ1.e4133_s2608_s2183
_r7326_r6282_p2516.02-03-450_output.root/
user.mdubovsk.361317.Sherpa.DAOD_TOPQ1.e4133_s2608_s2183
_r7326_r6282_p2516.02-03-450_output.root/
user.mdubovsk.361318.Sherpa.DAOD_TOPQ1.e4133_s2608_s2183
_r7326_r6282_p2516.02-03-45_output.root/
user.mdubovsk.361319.Sherpa.DAOD_TOPQ1.e4133_s2608_s2183
_r7326_r6282_p2516.02-03-450_output.root/
user.mdubovsk.361320.Sherpa.DAOD_TOPQ1.e4133_s2608_s2183
_r7326_r6282_p2516.02-03-450_output.root/
user.mdubovsk.361321.Sherpa.DAOD_TOPQ1.e4133_s2608_s2183
_r7326_r6282_p2516.02-03-45_output.root/
user.mdubovsk.361322.Sherpa.DAOD_TOPQ1.e4133_s2608_s2183
_r7326_r6282_p2516.02-03-450_output.root/
user.mdubovsk.361323.Sherpa.DAOD_TOPQ1.e4133_s2608_s2183
_r7326_r6282_p2516.02-03-45_output.root/
user.mdubovsk.361324.Sherpa.DAOD_TOPQ1.e3651_s2608_s2183
_r7267_r6282_p2516.02-03-450_output.root/
user.mdubovsk.361325.Sherpa.DAOD_TOPQ1.e3651_s2586_s2174
_r7267_r6282_p2516.02-03-450_output.root/
user.mdubovsk.361326.Sherpa.DAOD_TOPQ1.e3651_s2608_s2183
_r7267_r6282_p2516.02-03-450_output.root/
user.mdubovsk.361327.Sherpa.DAOD_TOPQ1.e3651_s2586_s2174
_r7267_r6282_p2516.02-03-450_output.root/
user.mdubovsk.361328.Sherpa.DAOD_TOPQ1.e3651_s2586_s2174
_r7267_r6282_p2516.02-03-450_output.root/
user.mdubovsk.361329.Sherpa.DAOD_TOPQ1.e3651_s2586_s2174
_r7267_r6282_p2516.02-03-450_output.root/
user.mdubovsk.361330.Sherpa.DAOD_TOPQ1.e3651_s2586_s2174
_r7267_r6282_p2516.02-03-450_output.root/
user.mdubovsk.361331.Sherpa.DAOD_TOPQ1.e3651_s2586_s2174
_r7267_r6282_p2516.02-03-450_output.root/
user.mdubovsk.361332.Sherpa.DAOD_TOPQ1.e3651_s2586_s2174
_r7267_r6282_p2516.02-03-450_output.root/

user.mdubovsk.361333.Sherpa.DAOD_TOPQ1.e4133_s2608_s2183
_r7326_r6282_p2516.02-03-450_output.root/
user.mdubovsk.361334.Sherpa.DAOD_TOPQ1.e4133_s2608_s2183
_r7326_r6282_p2516.02-03-450_output.root/
user.mdubovsk.361335.Sherpa.DAOD_TOPQ1.e4133_s2608_s2183
_r7326_r6282_p2516.02-03-45_output.root/
user.mdubovsk.361336.Sherpa.DAOD_TOPQ1.e4133_s2608_s2183
_r7326_r6282_p2516.02-03-450_output.root/
user.mdubovsk.361337.Sherpa.DAOD_TOPQ1.e4133_s2608_s2183
_r7326_r6282_p2516.02-03-450_output.root/
user.mdubovsk.361338.Sherpa.DAOD_TOPQ1.e4133_s2608_s2183
_r7326_r6282_p2516.02-03-450_output.root/
user.mdubovsk.361339.Sherpa.DAOD_TOPQ1.e4133_s2608_s2183
_r7326_r6282_p2516.02-03-450_output.root/
user.mdubovsk.361340.Sherpa.DAOD_TOPQ1.e4133_s2608_s2183
_r7326_r6282_p2516.02-03-450_output.root/
user.mdubovsk.361341.Sherpa.DAOD_TOPQ1.e4133_s2608_s2183
_r7326_r6282_p2516.02-03-45_output.root/
user.mdubovsk.361342.Sherpa.DAOD_TOPQ1.e4133_s2608_s2183
_r7326_r6282_p2516.02-03-450_output.root/
user.mdubovsk.361343.Sherpa.DAOD_TOPQ1.e4133_s2608_s2183
_r7326_r6282_p2516.02-03-450_output.root/
user.mdubovsk.361344.Sherpa.DAOD_TOPQ1.e4133_s2608_s2183
_r7326_r6282_p2516.02-03-450_output.root/
user.mdubovsk.361345.Sherpa.DAOD_TOPQ1.e4133_s2608_s2183
_r7326_r6282_p2516.02-03-45_output.root/
user.mdubovsk.361346.Sherpa.DAOD_TOPQ1.e4133_s2608_s2183
_r7326_r6282_p2516.02-03-45_output.root/
user.mdubovsk.361347.Sherpa.DAOD_TOPQ1.e4133_s2608_s2183
_r7326_r6282_p2516.02-03-450_output.root/
user.mdubovsk.361348.Sherpa.DAOD_TOPQ1.e3733_s2608_s2183
_r7267_r6282_p2516.02-03-450_output.root/
user.mdubovsk.361349.Sherpa.DAOD_TOPQ1.e3733_s2608_s2183
_r7267_r6282_p2516.02-03-450_output.root/
user.mdubovsk.361350.Sherpa.DAOD_TOPQ1.e3733_s2608_s2183
_r7267_r6282_p2516.02-03-450_output.root/
user.mdubovsk.361351.Sherpa.DAOD_TOPQ1.e3733_s2608_s2183
_r7267_r6282_p2516.02-03-450_output.root/
user.mdubovsk.361352.Sherpa.DAOD_TOPQ1.e3733_s2608_s2183
_r7267_r6282_p2516.02-03-450_output.root/
user.mdubovsk.361353.Sherpa.DAOD_TOPQ1.e3733_s2608_s2183
_r7267_r6282_p2516.02-03-450_output.root/
user.mdubovsk.361354.Sherpa.DAOD_TOPQ1.e3733_s2608_s2183
_r7267_r6282_p2516.02-03-450_output.root/

user.mdubovsk.361355.Sherpa.DAOD_TOPQ1.e3733_s2608_s2183
_r7267_r6282_p2516.02-03-450_output.root/
user.mdubovsk.361356.Sherpa.DAOD_TOPQ1.e3733_s2608_s2183
_r7267_r6282_p2516.02-03-450_output.root/
user.mdubovsk.361357.Sherpa.DAOD_TOPQ1.e4133_s2608_s2183
_r7326_r6282_p2516.02-03-450_output.root/
user.mdubovsk.361358.Sherpa.DAOD_TOPQ1.e4133_s2608_s2183
_r7326_r6282_p2516.02-03-450_output.root/
user.mdubovsk.361359.Sherpa.DAOD_TOPQ1.e4133_s2608_s2183
_r7326_r6282_p2516.02-03-450_output.root/
user.mdubovsk.361360.Sherpa.DAOD_TOPQ1.e4133_s2608_s2183
_r7326_r6282_p2516.02-03-450_output.root/
user.mdubovsk.361361.Sherpa.DAOD_TOPQ1.e4133_s2608_s2183
_r7326_r6282_p2516.02-03-45_output.root/
user.mdubovsk.361362.Sherpa.DAOD_TOPQ1.e4133_s2608_s2183
_r7326_r6282_p2516.02-03-45_output.root/
user.mdubovsk.361363.Sherpa.DAOD_TOPQ1.e4133_s2608_s2183
_r7326_r6282_p2516.02-03-45_output.root/
user.mdubovsk.361364.Sherpa.DAOD_TOPQ1.e4133_s2608_s2183
_r7326_r6282_p2516.02-03-450_output.root/
user.mdubovsk.361365.Sherpa.DAOD_TOPQ1.e4133_s2608_s2183
_r7326_r6282_p2516.02-03-450_output.root/
user.mdubovsk.361366.Sherpa.DAOD_TOPQ1.e4133_s2608_s2183
_r7326_r6282_p2516.02-03-45_output.root/
user.mdubovsk.361367.Sherpa.DAOD_TOPQ1.e4133_s2608_s2183
_r7326_r6282_p2516.02-03-45_output.root/
user.mdubovsk.361368.Sherpa.DAOD_TOPQ1.e4133_s2608_s2183
_r7326_r6282_p2516.02-03-45_output.root/
user.mdubovsk.361369.Sherpa.DAOD_TOPQ1.e4133_s2608_s2183
_r7326_r6282_p2516.02-03-45_output.root/
user.mdubovsk.361370.Sherpa.DAOD_TOPQ1.e4133_s2608_s2183
_r7326_r6282_p2516.02-03-450_output.root/
user.mdubovsk.361371.Sherpa.DAOD_TOPQ1.e4133_s2608_s2183
_r7326_r6282_p2516.02-03-450_output.root/

Bibliography

[1] M. Thomson, *Modern Particle Physics*, Cambridge University Press, Cambridge (2013)

[2] D. Griffiths, *Introduction to Elementary Particles*, WILEY-VCH, Weinheim (2008)

[3] P. W. Higgs, *Broken Symmetries, Massless Particles and Gauge Fields*, Phys. Lett. **12**, 132 (1964)

[4] F. Englert, R. Brout, *Broken Symmetry and the Mass of Gauge Vector Mesons*, Phys. Rev. Lett. **13**, 321 (1964)

[5] G. S. Guralnik, C. R. Hagen, T. W. B. Kibble, *Global Conservation Laws and Massless Particles*, Phys. Rev. Lett. **13**, 585 (1964)

[6] ATLAS Collaboration, *Evidence for the spin-0 nature of the Higgs boson using ATLAS data*, Phys. Lett. B **726**, 120 (2013)

[7] ATLAS Collaboration, *Observation of a new particle in the search for the Standard Model Higgs boson with the ATLAS detector at the LHC*, Phys. Lett. B **716**, 1 (2012)

[8] K. A. Olive, et al. (Particle Data Group), *Review of Particle Physics*, Chin. Phys. C **38**, 090001 (2014)

[9] E. Noether, *Invariante Variationsprobleme*, Nachrichten von der Gesellschaft der Wissenschaften zu Göttingen, Mathematisch-Physikalische Klasse **1918**, 235 (1918)

[10] S. Weinberg, *A Model of Leptons*, Phys. Rev. Lett. **19**, 1264 (1967)

[11] A. Salam, *Weak and Electromagnetic Interactions*, ed. Nobel Symposium No. 8 (Almqvist & Wiksell) (1968)

[12] S. L. Glashow, J. Iliopoulos, L. Maiani, *Weak Interactions with Lepton-Hadron Symmetry*, Phys. Rev. D **2**, 1285 (1970)

[13] H. Georgi, S. L. Glashow, *Unified Weak and Electromagnetic Interactions without Neutral Currents*, Phys. Rev. Lett. **28**, 1494 (1972)

[14] ATLAS, CDF, CMS, DØ Collaborations, *First combination of Tevatron and LHC measurements of the top-quark mass* **(ATLAS-CONF-2014-008, CDF-NOTE-11071, CMS-PAS-TOP-13-014, D0-NOTE-6416, FERMILAB-TM-2582-E)** (2014)

[15] M. Czakon, P. Fiedler, A. Mitov, *Total Top-Quark Pair-Production Cross Section at Hadron Colliders Through* $O(\pm\frac{4}{S})$, Phys. Rev. Lett. **110**, 252004 (2013)

[16] V. M. Abazov, et al. (DØ Collaboration), $t\bar{t}$ *production cross-section in* $p\bar{p}$ *collisions at* $\sqrt{s} = 1.8$ TeV, Phys. Rev. D **67**, 012004 (2003)

[17] T. Affolder, et al. (CDF Collaboration), *Measurement of the* $t\bar{t}$ *production cross section in* $p\bar{p}$ *collisions at* $\sqrt{s} = 1.8$ TeV, Phys. Rev. D **64**, 032002 (2001), [Erratum: Phys. Rev.D 67, 119901 (2003)]

[18] Abazov, V. M. and others (DØ Collaboration), *Measurement of the inclusive* $t\bar{t}$ *production cross section in* $p\bar{p}$ *collisions at* $\sqrt{s} = 1.96$ TeV, D0-CONF-Note 6453 (2015)

[19] T. Aaltonen, et al. (CDF Collaboration), *Measurement of the top-quark pair production cross-section in events with two leptons and bottom-quark jets using the full CDF data set*, Phys. Rev. D **88**, 091103 (2013)

[20] T. A. Aaltonen, et al. (CDF, DØ Collaborations), *Combination of measurements of the top-quark pair production cross section from the Tevatron Collider*, Phys. Rev. D **89(7)**, 072001 (2014)

[21] ATLAS Collaboration, *Measurement of the top pair production cross section in* 8 TeV *proton–proton collisions using kinematic information in the lepton+jets final state with ATLAS*, Phys. Rev. D **91**, 112013 (2015)

[22] ATLAS Collaboration, *Measurement of the* $t\bar{t}$ *production cross section in the all-hadronic channel in* 4.7 fb^{-1} *of* pp *collisions at* $\sqrt{s} = 7$ TeV *with the ATLAS detector*, ATLAS-CONF-2012-031 (2012)

[23] ATLAS Collaboration, *Statistical combination of top quark pair production cross-section measurements using dilepton, single-lepton, and all-hadronic final states at* $\sqrt{s} = 7$ TeV *with the ATLAS detector*, ATLAS-CONF-2012-024 (2012)

[24] CMS Collaboration, *Measurement of the* $t\bar{t}$ *production cross section in the all-jet final state in* pp *collisions at* $\sqrt{s} = 7$ TeV, JHEP **1305**, 065 (2013)

[25] CMS Collaboration, *Measurement of the* $t\bar{t}$ *production cross section in* pp *collisions at* $\sqrt{s} = 7$ TeV *with lepton + jets final states*, Phys. Lett. B **720**, 83 (2013)

[26] LHCb Collaboration, *First observation of top quark production in the forward region*, Phys. Rev. Lett. **115(11)**, 112001 (2015)

[27] J. Alwall, et al., *The automated computation of tree-level and next-to-leading order differential cross sections, and their matching to parton shower simulations*, JHEP **2014(07)**, 1 (2014)

[28] J. M. Campbell, R. K. Ellis, $t\bar{t}W^{+-}$ *production and decay at NLO*, JHEP **07**, 52 (2012)

[29] ATLAS Collaboration, *Search for* $t\bar{t}Z$ *production in the three lepton final state with* 4.7 fb^{-1} *of* $\sqrt{s} = 7$ TeV pp *collision data collected by the ATLAS detector*, ATLAS-CONF-2012-126 (2012)

[30] CMS Collaboration, *Measurement of associated production of vector bosons and top quark-antiquark pairs at* $\sqrt{(s)} = 7$ TeV, Phys. Rev. Lett. **110**, 172002 (2013)

[31] ATLAS Collaboration, *Measurement of the* $t\bar{t}W$ *and* $t\bar{t}Z$ *production cross sections in pp collisions at* $\sqrt{s} = 8$ TeV *with the ATLAS detector*, JHEP **11**, 172 (2015)

[32] CMS Collaboration, *Observation of top quark pairs produced in association with a vector boson in pp collisions at* $\sqrt{s} = 8$ TeV, JHEP **01**, 096 (2016)

[33] ATLAS Collaboration, *Measurement of the* $t\bar{t}Z$ *and* $t\bar{t}W$ *production cross sections in multilepton final states using* 3.2 fb^{-1} *of* pp *collisions at* 13 TeV *at the LHC*, Technical Report ATLAS-CONF-2016-003 (2016)

[34] CMS Collaboration, *Measurement of the cross section of top quark pair production in association with a Z boson in pp collisions at* 13 TeV, Technical Report CMS-PAS-TOP-16-009 (2016)

[35] O. S. Brüning, et al., *LHC Design Report*, CERN, Geneva (2004)

[36] R. Brun, et al., *Simulation program for particle physics experiments, GEANT: user guide and reference manual*, CERN DD 78-2, 1978 (unpublished)

[37] S. Agostinelli, et al., *GEANT4: A Simulation Toolkit*, Nucl. Instrum. Methods A **506**, 250 (2003)

[38] T. Gleisberg, et al., *SHERPA 1.α, a proof-of-concept version*, JHEP **0402**, 056 (2004)

[39] A. Schälicke, et al., *Event Generator for Particle Production in High-Energy Collisions*, Prog. Part. Nucl. Phys. **53**, 329 (2004)

[40] T. Gleisberg, et al., *Predictions for multi-particle final states with SHERPA*, Talk at Physics at LHC, Vienna, Austria, 2004,

[41] S. Alioli, et al., *A general framework for implementing NLO calculations in shower Monte Carlo programs: the POWHEG BOX*, JHEP **06**, 43 (2010)

[42] S. Alioli, et al., *Vector boson plus one jet production in POWHEG*, JHEP **01**, 95 (2011)

[43] S. Alioli, et al., *NLO single-top production matched with shower in POWHEG: s- and t-channel contributions*, JHEP **09**, 111 (2009), [Erratum: JHEP 02, 011 (2010)]

[44] J. M. Campbell, et al., *Top-pair production and decay at NLO matched with parton showers*, JHEP **04**, 114 (2015)

[45] T. Sjöstrand, S. Mrenna, P. Z. Skands, *PYTHIA 6.4 Physics and Manual*, JHEP **05**, 26 (2006)

[46] P. Z. Skands, *Tuning Monte Carlo Generators: The Perugia Tunes*, Phys. Rev. D **82**, 074018 (2010)

[47] J. Alwall, et al., *The automated computation of tree-level and next-to-leading order differential cross sections, and their matching to parton shower simulations*, JHEP **07**, 79 (2014)

[48] T. Sjöstrand, et al., *An Introduction to PYTHIA 8.2*, Comput. Phys. Commun. **191**, 159 (2015)

[49] R. D. Ball, et al., *Parton distributions with LHC data*, Nucl. Phys. B **867**, 244 (2013)

[50] M. Bahr, et al., *Herwig++ Physics and Manual*, Eur. Phys. J. C **58**, 639 (2008)

[51] D. Lange, *The EvtGen particle decay simulation package*, Nucl. Instrum. Methods A **462**, 152 (2001)

[52] T. Gleisberg, et al., *Event generation with SHERPA 1.1*, JHEP **902**, 7 (2009)

[53] T. Gleisberg, S. Höche, *Comix, a new matrix element generator*, JHEP **812**, 39 (2008)

[54] F. Cascioli, P. Maierhofer, S. Pozzorini, *Scattering Amplitudes with Open Loops*, Phys. Rev. Lett. **108**, 111601 (2012)

[55] S. Schumann, F. Krauss, *A Parton shower algorithm based on Catani-Seymour dipole factorisation*, JHEP **803**, 38 (2008)

[56] S. Höche, et al., *QCD matrix elements + parton showers: The NLO case*, JHEP **04**, 27 (2013)

[57] ATLAS Collaboration, *Expected electron performance in the ATLAS experiment*, ATL-PHYS-PUB-2011-006 (2011)

[58] ATLAS Collaboration, *Muon reconstruction performance of the ATLAS detector in proton-proton collision data at* $\sqrt{s} = 13$ TeV, Eur. Phys. J. C **76(5)**, 292 (2016)

[59] M. Cacciari, G. P. Salam, G. Soyez, *The anti-k_t jet clustering algorithm*, JHEP **04**, 63 (2008)

[60] W. Lampl, et al., *Calorimeter Clustering Algorithms: Description and Performance*, Technical Report ATL-LARG-PUB-2008-002, ATL-COM-LARG-2008-003 (2008)

[61] ATLAS Collaboration, *Tagging and suppression of pileup jets with the ATLAS detector*, ATLAS-CONF-2014-018 (2014)

[62] ATLAS Collaboration, *Expected performance of the ATLAS b-tagging algorithms in Run-2*, ATL-PHYS-PUB-2015-022 (2015)

[63] A. Wharton, W. Yao, R. Jansky, *ATLAS Inner Detector Track Quality Cuts for Run 2*, Technical Report ATL-COM-PHYS-2014-1084 (2014)

[64] ATLAS Collaboration, *Selection of jets produced in* 13 TeV *proton–proton collisions with the ATLAS detector*, ATLAS-CONF-2015-029 (2015)

[65] T. Hryn'ova, K. Nagano, *Trigger Menu Strategy for Run 2*, Technical Report ATL-COM-DAQ-2014-054 (2014)

[66] T. Berger-Hryn'ova, et al., *Physics Uses and Hardware Constraints of the L1 Topological Trigger*, Technical Report ATL-COM-DAQ-2014-005 (2014)

[67] T. Vazquez Schroeder, *Measurement of the associated production of a vector boson (W, Z) and top quark pair in the opposite sign dilepton channel with pp collisions at* $\sqrt{s} = 8$ TeV *with the ATLAS detector*, Ph.D. thesis, Göttingen U., II. Phys. Inst. (2014)

[68] M. Feindt, U. Kerzel, *The NeuroBayes neural network package*, Nucl. Instrum. Methods A **559**, 190 (2006)

[69] R. Byrd, et al., *A Limited Memory Algorithm for Bound Constrained Optimization*, SIAM J. Sci. Comput. **16(5)**, 1190 (1995)

Danksagung

This Master's course at the University of Goettingen took three years including one year at Tokyo Institute of Technology in Japan.

Thank you very much Arnulf Quadt for sparking my interest in particle physics and the cosmos of CERN, the LHC and ATLAS. Your support opened the doors to persue a broad education. An intense education in particle physics as a summer student at CERN, as a participant of the Hadron Collider Summer School 2014 (HASCO), as a Master's student at the II. Institute of Physics in Goettingen and as an international visiting student at Tokyo Institute of Technology. As well as an often underestimated, but very important education alongside research, by offering to contribute to *Physics in Advent* and participate in the core organisation teams of HASCO 2016 and the project *Physics for Refugees* at the time it was launched at the end of 2015.

Thank you as well for the open discussions and exchange about my future plans after graduating from the Master's programme in physics.

Thank you very much Boris Lemmer, Lisa Shabalina and María Moreno Llácer for your constant support in the Goettingen $t\bar{t}V$ group. Boris, you made sure that my project was on track and you always 'had an open ear' for questions and helped out whenever it was needed. Lisa, I profited a lot from the large experience that was mirrored in your comments and questions. Thank you as well for reading the whole draft of the thesis and adding your remarks. María, you have the ability to ask the final question, that was not discussed yet, but pins down the problem and enriches the academic exchange. Thank you to the three of you for guiding my Master's project.

Thank you very much Osamu Jinnouchi and Masahiro Kuze from the ATLAS group of TiTech for you hospitality during my stay in Tokyo. You allowed me to work on research in physics while diving into a completely new and exciting culture. Thank you for your patience with my Japanese and for supporting my participation in the ICEPP Symposium on Particle Physics 2015 in Nagano.

The enjoyable time in Goettingen started with a very friendly and supportive atmosphere within the group at the II. Institute of Physics. Thank you very much Professor Stan-sei for carrying happiness and a good mood into the corridors of the institute while still being willing to have detailed questions being answered during the seminars.

So many nationalities and so many different characters in the institute resulted in a lot of cake in various offices which very often also contributed to solving 'one or the other' problem, not only physics-wise. Thank you to the members of the II. Institute of Physics for your support and best of luck and success for your research and projects.

Finally, the gratitude I owe to my family and close friends cannot be expressed with words. You know that and this is why I will not even try. But rather return the affection and love you give to me.

Erklärung nach §17(9) der Prüfungsordnung für den Bachelor-Studiengang Physik und den Master-Studiengang Physik an der Universität Göttingen:

Hiermit erkläre ich, dass ich diese Abschlussarbeit selbständig verfasst habe, keine anderen als die angegebenen Quellen und Hilfsmittel benutzt habe und alle Stellen, die wörtlich oder sinngemäß aus veröffentlichten Schriften entnommen wurden, als solche kenntlich gemacht habe.
Darüberhinaus erkläre ich, dass diese Abschlussarbeit nicht, auch nicht auszugsweise, im Rahmen einer nichtbestandenen Prüfung an dieser oder einer anderen Hochschule eingereicht wurde.

Göttingen, den 6. Dezember 2016

(Tobias Christian Orthen)